Prabhakar Palni

Candidate

Physics and Astronomy

Department

This dissertation is approved, and it is acceptable in quality and form for publication:

Approved by the Dissertation Committee:

Dr. Sally Seidel, Chairperson

Dr. Igor Gorelov

Dr. Flera Rizatdinova

Dr. Rouzbeh Allahverdi

Dr. Leo Bitteker

Evidence for the Heavy Baryon Resonance State Λ_b^{*0} Observed with the CDF II Detector, and Studies of New Particle Tracking Technologies Using the LANSCE Proton Beam

by

Prabhakar Palni

B.Sc., Goa University, 2004
M.Sc., University of Mumbai, 2006

DISSERTATION

Submitted in Partial Fulfillment of the
Requirements for the Degree of

Doctor of Philosophy
Physics

The University of New Mexico

Albuquerque, New Mexico

May, 2014

Dedication

I dedicate this work to my beloved sister.

Acknowledgments

I would like to begin by thanking my advisor Prof. Sally Seidel, for her constant support and guidance throughout my research. Importantly, I am very thankful to her for motivating me and showing confidence in me right from the beginning through the up and down phases of my research work.

I would like to thank my co-advisor, Prof. Igor Gorelov, for his guidance and instruction in the analysis of the Λ_b^{*0} resonance state in the CDF and ROOT software environments. His mentoring and help in computer-related technical problems was very crucial when I first started my journey in the experimental particle physics field.

I would like to thank Martin Hoeferkamp for his help in the study of real time monitoring of charged particle beam profile and fluence. He has tremendously helped me during the development of the diode array technique carried out at the LANSCE facility of Los Alamos National Laboratory as well as in our laboratory. I would like to thank the Weapons Neutron Research facility at LANSCE and its associated staff for operating the facility during the experiments.

I would like to thank Satyajit Behari for collaborating on the Inclusive BMC project. I thank the members of the CDF Collaboration and the staff at Fermilab.

I want to thank Prof. Rouzbeh Allahverdi for mentoring and also for serving on my dissertation committee. I would like to thank you for your Cosmology, Electrodynamics, and Quantum Mechanics classes. I thoroughly enjoyed your courses and class discussions.

Many thanks to Prof. Flera Rizatdinova and Prof. Leo Bitteker for serving on my dissertation committee. Your feedback, comments, and advice on my dissertation have helped me improve my standards.

Many thanks to all the faculty members who have instructed me at the UNM Department of Physics during these years. I am very grateful to my teachers from my school, college, and University for their guidance in education and towards my career. Specially, I would like to thank Ms. Ranebai, Fenwick John, Dasharath Shetgaonkar, Lawrence Bosco, Rajendra Kanekar, Benedict Soares, Prof. A. Narsale, Dr. M.R. Press, Prof. A.A Rangwala, Prof. V.H. Kulkarni, and Charudatt Kadolkar.

I would like to thank my parents, my friends, and my best friends Venkatesh Veeraraghavan, Francisco Fernandes, Krishnkumar Chauhan, Vikrant Sawant, Mithun Shirodkar, Surya Kamulkar, and Jigyasa Rana for their unconditional support, love, and constant encouragement for the past six years.

Evidence for the Heavy Baryon Resonance State Λ_b^{*0} Observed with the CDF II Detector, and Studies of New Particle Tracking Technologies Using the LANSCE Proton Beam

by

Prabhakar Palni

B.Sc., Goa University, 2004
M.Sc., University of Mumbai, 2006

Ph.D., Physics, University of New Mexico, 2014

Abstract

To discover and probe the properties of new particles, we need to collide highly energetic particles. The Tevatron at Fermilab has collided protons and anti-protons at very high energies. These collisions produce short lived and stable particles, some known and some previously unknown. The CDF detector is used to study the products of such collisions and discover new elementary particles. To study the interaction between high energy charged particles and the detector materials often requires development of new instruments. Thus this dissertation involves a measurement at a contemporary experiment and development of technologies for related future experiments that will build on the contemporary one.

Using data from proton-antiproton collisions at $\sqrt{s} = 1.96\,\text{TeV}$ recorded by the CDF II detector at the Fermilab Tevatron, evidence for the excited resonance state

Λ_b^{*0} is presented in its $\Lambda_b^0\pi^-\pi^+$ decay, followed by the $\Lambda_b^0 \to \Lambda_c^+\pi^-$ and $\Lambda_c^+ \to pK^-\pi^+$ decays. The analysis is based on a data sample corresponding to an integrated luminosity of $9.6\,\mathrm{fb}^{-1}$ collected by an online event selection process based on charged-particle tracks displaced from the proton-antiproton interaction point. The significance of the observed signal is 3.5σ. The mass of the observed state is found to be 5919.22 ± 0.76 MeV/c^2 in agreement with similar findings in proton-proton collision experiments.

To predict the radiation damage to the components of new particle tracking detectors, prototype devices are irradiated at test beam facilities that reproduce the radiation conditions expected. The profile of the test beam and the fluence applied per unit time must be known. We have developed a technique to monitor in real time the beam profile and fluence using an array of *pin* semiconductor diodes whose forward voltage is linear with fluence over the fluence regime relevant to, for example, silicon tracking detectors in the LHC upgrade era. We have demonstrated this technique in the 800 MeV proton beam at the LANSCE facility of Los Alamos National Laboratory.

Contents

List of Figures

List of Tables

Chapter 1

Introduction

The quest to understand the nature of the fundamental particles and interactions between them motivates searches for elementary particles in the universe. This work is primarily dedicated to finding a fundamental particle called the Λ_b^{*0}, which is predicted by the Standard Model. The Λ_b^{*0} is a baryon which contains a heavy quark, b, and two light quarks, u and d. The discovery and detailed study of hadrons that contain a b quark is very effective in testing our understanding of the fundamental interactions and the validity of the Standard Model of particle physics.

The Standard Model is one of the most successful models of physics. It has provided most of the answers to our predominant questions, including the nature of the fundamental forces and their carriers and content of the visible matter in the universe. However, the Standard Model is incomplete because it does not incorporate gravity and does not provide answers to important questions, such as, What are dark energy and dark matter? and What is the origin of matter-antimatter asymmetry in the universe?

The report [1, 2] of the Higgs boson by the Large Hadron Collider (LHC) on 4 July 2012 confirmed the Higgs field which is crucial in the framework of the Standard

Model. The basic concepts of the Standard Model needed to understand this work are discussed in Chapter 2.

Heavy quark baryons are useful in probing Quantum Chromodynamics (QCD) in its confinement scale. The Heavy Quark Effective Theory (HQET) [3, 4, 5] which assumes an infinite mass for the heavy quark in heavy baryons is just a general quantum field theory based on the principles of relativity and Quantum Mechanics but without the restriction of renormalizability. The theoretical framework of HQET and its application to the Λ_b^{*0} is described in the second section of Chapter 2.

To discover and probe the properties of new particles, we need to collide highly energetic particles. The Tevatron [6] at Fermilab accelerated protons and anti-protons close to the speed of light, and then made them collide head-on inside the Collider Detector at Fermilab (CDF) [7]. The CDF detector was used to study the products of such collisions by reconstructing the events that occurred around the collision point. The Tevatron produced approximately 2.5 million collisions per second at each interaction region. However, the event recording capability of the experiment did not permit storage of all of the data. A small fraction of the events was recorded for further processing. Such selection is performed by a system called a trigger, that can interpret the online data from a collision rapidly. The Tevatron collider, the CDF II detector, and the trigger system are described in Chapters 3 and 4. Particular emphasis is put on the Central Outer Tracker (a drift chamber), the silicon vertex detector, and the Two Track Trigger, all of which are of particular importance in this analysis.

The 9.6 fb^{-1} of data collected by the CDF II detector contains a large number of heavy baryons. A baryon is made up of three quarks bound by the strong force. The search for the heavy baryon resonance state Λ_b^{*0} starts with the reconstruction of the ground state Λ_b^0, and follows with the reconstruction of the Λ_b^{*0} by using two oppositely charged soft pions and the Λ_b^0. Chapter 5 details the main analysis of

this search and presents the evidence for a bottom baryon resonance state Λ_b^{*0}. The systematic error studies carried out for this analysis are presented in Chapter 6. The main sources of systematic uncertainties turn out to be due to the uncertainty on the momentum scale and due to the detector resolution model.

To study the interaction between high energy charged particles and the detector materials often requires development of new instruments. Detectors planned for use at the Large Hadron Collider [8] will operate in a radiation field produced by beam collisions. Hence, to predict the radiation damage to the components of the detectors, the profile of the charged particle beam and the fluence received must be known precisely and instantaneously. The second analysis, presented in Chapter 7 and Chapter 8, is "Studies of New Particle Tracking Technologies Using the LANSCE Proton Beam".

The CDF heavy flavor physics program includes a broad range of analyses involving final states with bottom and charm hadrons. Over most of Run II, the heavy flavor physics analyzers produced their own Monte Carlo (MC) samples using custom setups which were not centrally organized nor documented adequately for their reuse by other analyses. Most of these samples were based on a specific signal or background decay and were outdated by each new release of the CDF II software framework. It is our goal to produce a large generic B/charm Monte Carlo (BMC) sample to serve all the future analyses requiring background composition studies. This work is detailed in Chapter 9.

Chapter 10 wraps up the dissertation by drawing conclusions and summarizing the results of the main analysis on evidence [9, 10, 11] for a bottom baryon resonance state Λ_b^{*0}, studies of new particle tracking technologies using the LANSCE proton beam, and a production of a large inclusive BMC sample. Appendix A presents a brief description of the data definition file used in the inclusive BMC study.

Chapter 2

Theoretical Overview and Motivation

2.1 Standard Model of Particle Physics

The Standard Model [12, 13] of elementary particles or particle physics is the theory that describes the fundamental interactions between the elementary particles and the force carriers. All these elementary particles are subject to four fundamental interactions, the strong, the weak, the electromagnetic, and the gravitational interaction. However, the gravitational interaction is so weak that it is not included in the framework of the Standard Model. The fundamental forces are mediated by vector or spin-1 bosons, and the elementary building blocks of visible matter are made of fermions, shown in Figure 2.1.

The Standard Model is based on a renormalizable quantum field theory that is invariant under the transformations in $SU(3)_C \otimes SU(2)_L \otimes U(1)_Y$. The indices refer to the conserved quantity in each transformation: weak hypercharge (Y), color (C), and for $SU(2)$, although the weak isospin (I) is the conserved quantity, the L denotes

the fact that it involves only left-handed fields. The three gauge symmetries give rise to three fundamental interactions. According to the Standard Model the Higgs boson, which is a scalar, gives mass to all the elementary particles by spontaneous breaking of electro-weak gauge symmetry. The Higgs potential is invariant under the electro-weak symmetry. However, the minimum of the potential is situated at a non-zero field value (vacuum expectation value), which spontaneously breaks the electro-weak symmetry.

2.2 Elementary Particles of Matter and Fundamental Forces in Nature

Fermions are the elementary building blocks of matter, and they are further classified into six quarks and six leptons. They are spin $\frac{1}{2}$ particles obeying Fermi-Dirac statistics. The characteristics of fermions are shown in Table 2.1.

The quarks can be arranged into three generations of increasing mass, where each generation consists of a quark with electric charge $+\frac{2}{3}$ and one with charge $-\frac{1}{3}$. The up and down quarks are the lowest mass generation and they are the basic constituents of protons and neutrons. The second generation contains the charm and strange quarks and the third generation consists of the heavy mass top and bottom quarks. The existence of the heaviest of these quarks, the top quark, was discovered at the Tevatron in 1995 [14]. The quarks come in three colors, Red (R), Green (G), and Blue (B), and are bound by gluons to form colorless hadrons. The hadrons are grouped into baryons (made of three quarks) and mesons (made of a quark and anti-quark).

Vector or spin-1 bosons are the mediator of interactions. They obey Bose-Einstein statistics. The fundamental particles and interactions of nature are listed in Table

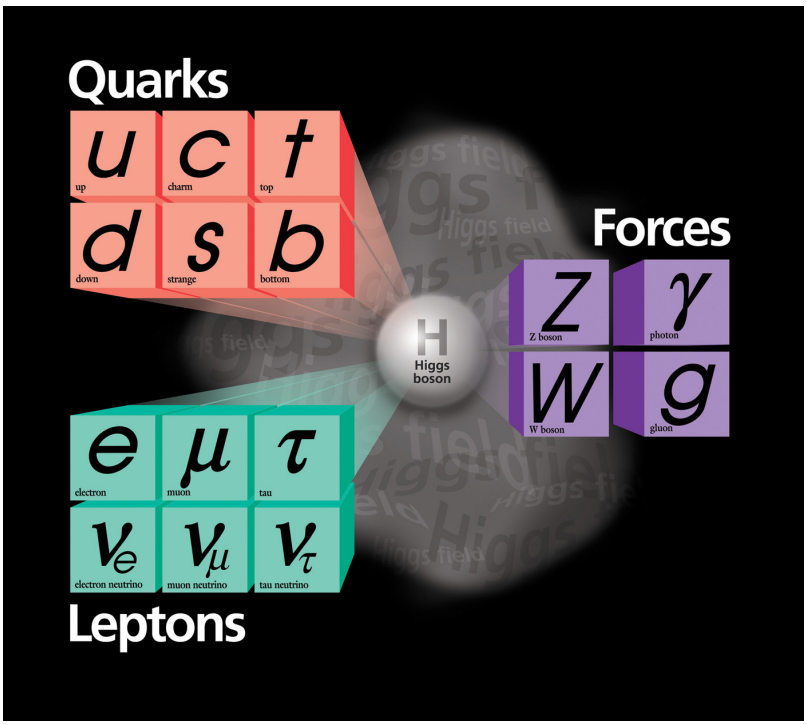

Figure 2.1: Elementary particles and force carriers.

2.2. All of the fundamental particles have an antimatter. The strong nuclear force is mediated by the gluon which binds the quarks in hadrons. The strength of the strong force increases with the distance between quarks and results in quark confinement. Quark confinement and perturbative QCD will be discussed in more detail in the next section. There are 8 gluons, which also interact via strong interactions. Leptons, however, do not carry any color charge, and have no strong interactions.

The electromagnetic interaction is carried by the massless photon which couples to all charged particles. It is the electromagnetic force that binds the electrons to nuclei in an atom. The range of the force is infinite although its strength falls off as the square of the distance. In quantum field theory, the local gauge transformation that leaves the action invariant forms a unitary gauge group $U(1)$ which give rise to Quantum Electrodynamics (QED). In order to preserve the local gauge invariance,

Name	Symbol	Charge Q	Mass (MeV/c^2)
Quarks			
up	u	$+\frac{2}{3}$	2.3
down	d	$-\frac{1}{3}$	4.8
charm	c	$+\frac{2}{3}$	$(1.275 \pm 0.025) \times 10^3$
strange	s	$-\frac{1}{3}$	95 ± 5
top	t	$+\frac{2}{3}$	$(173.07 \pm 0.72) \times 10^3$
bottom	b	$-\frac{1}{3}$	$(4.18 \pm 0.03) \times 10^3$
Leptons			
electron	e^-	-1	0.511
electron neutrino	ν_e	0	< 2 eV/c^2
muon	μ	-1	105.7
muon neutrino	ν_μ	0	< 0.19
tau	τ	-1	17776.90 ± 0.20
tau neutrino	ν_τ	0	< 18

Table 2.1: Elementary particles of matter and their quantum numbers.

the photon is required to be massless.

The weak force is mediated by one neutral (Z^0) vector boson and two charged (W^- and W^+) vector bosons. The weak interaction is responsible for all the interactions which change quark flavors, such as β-decay. The strength of the weak coupling between the particles is determined by the weak isospin. The mass and the weak isospin eigenstates of quarks are related to each other by a unitary matrix called the CKM matrix (after Cabibbo, Kobayashi and Maskawa) [15, 16]. Left-handed fermions carry weak isospin, $I = \frac{1}{2}$ with third component $I_z = \pm\frac{1}{2}$, while right-handed fermions have $I = 0$. The W^+, W^-, and Z^0 gauge bosons also interact via weak interactions. The Glashow-Salam-Weinberg model unifies the electromagnetic and weak interaction within the same theoretical framework via the $SU(2) \otimes U(1)$ symmetry.

Force	Gauge boson	Charge	Spin	Relative strength	Range (cm)	Mass [22] (GeV)
Strong	gluon (g)	0	1	1	$\sim 10^{-13}$	0
EM	photon (γ)	0	1	10^{-2}	infinite	0
Weak	W^+	+1	1	10^{-6}	$\sim 10^{-16}$	80.385 ± 0.015
	W^-	-1	1			80.385 ± 0.015
	Z	0	1			91.187 ± 0.002
Gravity	graviton (G)	0	2	10^{-40}	infinite	0

Table 2.2: The fundamental forces in nature and their properties.

2.3 Mesons and Baryons

In the quark model, mesons are hadrons composed of one quark and one antiquark. The spin quantum number of mesons can be $S = 0$ for anti-parallel orientation or $S = 1$ for parallel alignment. Since mesons can only have integer spin, they are bosons. If the orbital angular momentum quantum number L is zero (no orbital excitations), the mesons with spin $S = 1$ are called vector mesons with quantum numbers $J^P = 1^-$. The mesons with no orbital excitations, $L = 0$, and no spin ($S = 0$) are called pseudoscalars, with quantum numbers $J^P = 0^-$. J is the total angular momentum resulting from the combination of spin and orbital angular momentum. Its range is $|l - s| < J < |l + s|$. P is the parity. The parity of the meson is given by $P = (-1)^{l+1}$ as $P = 1$ is assigned to quarks and $P = -1$ to antiquarks.

For three flavors of light quarks, u, d, and s, there are nine ($3 \otimes 3 = 8 + 1$) possible combination of light mesons classified by means of $SU(3)$ flavor symmetry. The nine mesons divide into an $SU(3)$ octet and an $SU(3)$ singlet. Similarly by including the charm quark, the symmetry can be expanded to $SU(4)$. However, $SU(4)$ symmetry is stronger because of the higher mass of the charm quark. The D meson is the lightest charm meson. There are 16 possible meson states ($4 \otimes 4 = 15 + 1$) made from u, d, s, and c quarks, and these are shown in Figure 2.2. These pseudoscalar and

vector mesons are in their ground states; they have no orbital angular momentum excitation nor radial.

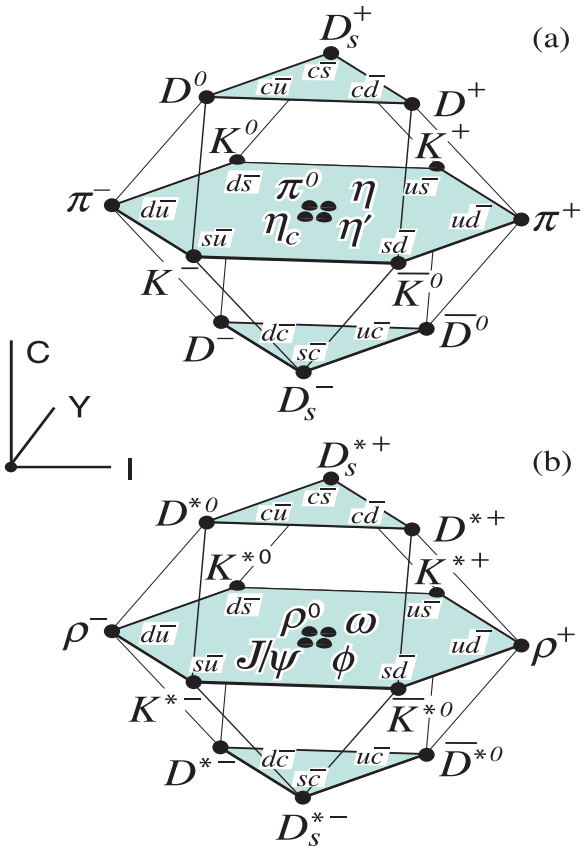

Figure 2.2: The multiplets of mesons made from u, d, s, and c quarks, plotted in (I_3, Y, C) space. Pseudoscalar (top) and vector meson multiplets (bottom) include the four lightest quarks [22].

Baryons are made of valence quarks. They are fermions with spin quantum numbers $S = \frac{1}{2}$ or $S = \frac{3}{2}$. They must obey the Pauli exclusion principle and keep their total wave function ($|qqq\rangle_A = |$ color $\rangle_A \otimes |$space, spin, flavor$\rangle_S$) anti-symmetric under the interchange of any two quarks. The subscript S stands for symmetric and A stands for antisymmetric. Since all baryon bound states are colorless, $|color\rangle$ is always anti-symmetric, which requires the rest of the wave function to be symmetric.

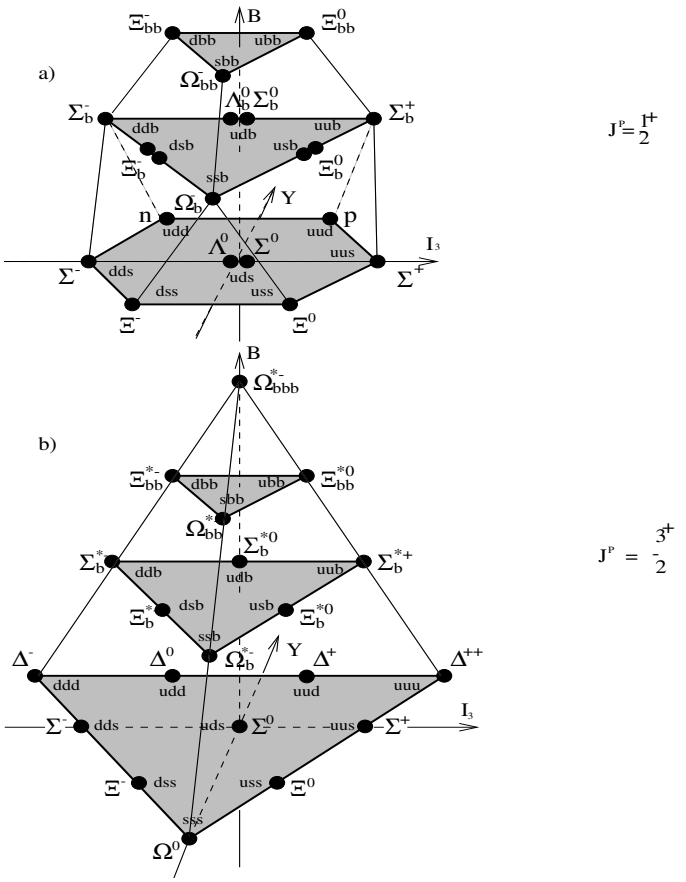

Figure 2.3: The multiplets of ground state baryons made from u, d, s, and b quarks with total spin quantum numbers $J^P = \frac{1}{2}^+$ and $J^P = \frac{3}{2}^+$ [22].

For orbital excitation $l = 0$, $|space\rangle$ is symmetric. Spin is only symmetric for $S = \frac{1}{2}$, but it has a mixed symmetry for $S = \frac{3}{2}$. For the three lightest quarks (u, d, and s) there are 27 possible qqq combinations of baryons using $SU(3)$ symmetry ($3 \otimes 3 \otimes 3 = 10 + 8 + 8 + 1$). The ground state baryon multiplets carying u, d, s, and b quarks and the total spin quantum numbers $J^P = \frac{1}{2}^+$ and $J^P = \frac{3}{2}^+$ are shown in Figure 2.3. The spin $\frac{3}{2}$ is associated with the decuplet, and the spin $\frac{1}{2}$ with the two octets. The anti-symmetric single state is forbidden for $l = 0$. Furthermore, $SU(3)$ symmetry can be expanded to a stronger broken $SU(4)$ symmetry by including the charm quark.

2.4 Lagrangian Formulation of the Quantum Field Theory

Quantum field theory is the mathematical framework that incorporates the principles of quantum mechanics and special relativity to explain the physics of elementary particles and their interactions. In quantum mechanics, any system is described by a wave function ψ, whereas in quantum field theories, each particle is described by an excitation of a local field $\phi(x)$. Their interactions are expressed in the Lagrangian density $\mathcal{L}$. In the framework of classical mechanics, the properties and equation of motion of the interacting particles are described by the Lagrangian density, using the field and its space-time derivatives,

$$\mathcal{L}(x) = \mathcal{L}(\phi, \partial_\mu \phi).$$

The Principle of Least Action describes the evolution of a system from an initial to a final state, along a path for which the action S is stationary:

$$\delta S = \delta \int \mathcal{L}(\phi, \partial_\mu \phi) d^4x = 0.$$

This equation leads to the Euler-Lagrange equation that describes the motion of the field,

$$\partial_\mu \Big(\frac{\partial \mathcal{L}}{\partial(\partial_\mu \phi)} \Big) - \frac{\partial \mathcal{L}}{\partial \phi} = 0.$$

In quantum field theory, the gauge symmetries play an important role. A symmetry is any continuous transformation of the field that does not change δS and leaves the Lagrangian invariant. These symmetry transformations (for example rotation about an axis) form the gauge symmetry groups of the system.

A transformation ($\phi \rightarrow \phi + \epsilon \Delta\phi$), where ϵ is an infinitesimal parameter, can be a symmetry of the system if the Lagrangian density remains invariant under this

transformation up to a four-divergence

$$\mathcal{L} \to \mathcal{L} + \epsilon \partial_\mu J^\mu$$

Noether's Theorem says, every symmetry of nature yields a conserved quantity and similarly, every conserved quantity reveals an underlying symmetry. For example the current density is given by

$$j_\mu(x) = \frac{\partial \mathcal{L}}{\partial(\partial_\mu \phi)} \Delta\phi - J^\mu.$$

Hence current is conserved,

$$\partial_\mu j^\mu = 0.$$

2.5 The Mathematical Framework of the Electromagnetic Interaction

Quantum electrodynamics (QED) is an abelian gauge theory describing the interaction between particles possessing electric charge. The Lagrangian for a free Dirac fermion field ψ of mass m is given by

$$\mathcal{L} = \bar{\psi}(i\gamma^\mu \partial_\mu - m)\psi, \tag{2.1}$$

where $\bar{\psi} = \psi^\dagger \gamma^0$ and the γ^μ are the Dirac matrices. Equation 2.1 satisfies the global $U(1)$ symmetry transformation given by

$$\psi(x) \to U\psi(x) = e^{iQ\alpha}\psi(x) \tag{2.2}$$

with the electric charge Q and the space independent parameter α. The family of such phase transformations forms a unitary abelian group known as the $U(1)$ group.

In the case of the Dirac field, the conserved current j^μ is given by

$$j^\mu = -Q\bar{\psi}\gamma^\mu\psi. \tag{2.3}$$

This describes the conservation of charge, as the time component of the current 4-vector j^μ, integrated over the space, is a constant.

An elegant way to introduce interaction in the free Lagrangian is to shift from the global (space independent, α), $U(1)$ transformation to a local (space dependent, $\alpha(x)$), $U(1)$ transformation,

$$\psi(x) \to U\psi(x) = e^{iQ\alpha(x)}\psi(x). \tag{2.4}$$

Clearly, the Lagrangian density is not locally gauge invariant under this transformation as

$$\partial_\mu\psi \to e^{iQ\alpha(x)}\partial_\mu\psi + ie^{iQ\alpha(x)}\psi\partial_\mu\alpha. \tag{2.5}$$

In order to satisfy local gauge invariance, a covariant derivative D_μ is introduced:

$$\partial_\mu \to D_\mu = \partial_\mu + iQA_\mu, \tag{2.6}$$

where A_μ is a new field, called the "gauge field"

$$D_\mu\psi(x) \to e^{iQ\alpha(x)}D_\mu\psi(x) \tag{2.7}$$

A_μ transforming as,

$$A_\mu \to A_\mu - \frac{1}{Q}\partial_\mu\alpha(x) \tag{2.8}$$

Equation 2.6 introduces into the Lagrangian a new term

$$\mathcal{L} = \bar{\psi}(i\gamma^\mu\partial_\mu - m)\psi + Q\bar{\psi}\gamma^\mu A_\mu\psi \tag{2.9}$$

which describes the interaction of the gauge field or vector field A_μ with the electromagnetic current $j^\mu = -Q\bar{\psi}\gamma^\mu\psi$.

The Lagrangian density needs a kinematic part for the vector field. The massive Lagrangian density is given by

$$\mathcal{L} = -\frac{1}{4}F^{\mu\nu}F_{\nu\mu} + \frac{1}{4}m^2 A_\mu A^\mu \tag{2.10}$$

where $F^{\mu\nu}$ is the electromagnetic field strength tensor, defined as $F^{\mu\nu} = \partial_\mu A_\nu - \partial_\nu A_\mu$. Only the first term in the Lagrangian density is locally gauge invariant. The second (mass) term breaks gauge invariance. To satisfy the gauge invariance principle, the gauge field is required to be massless and the full Lagrangian density is given as

$$\mathcal{L}_{QED} = -\frac{1}{4}F^{\mu\nu}F_{\nu\mu} + \bar{\psi}(i\gamma^\mu D_\mu \psi - m)\psi. \tag{2.11}$$

To satisfy local gauge invariance, a vector field A_μ has been introduced into the Lagrangian of the Dirac field spin-1/2 particles. It is the photon field, obeying Maxwell's Lagrangian Equation:

$$\mathcal{L}_{Maxwell} = -\frac{1}{4}F^{\mu\nu}F_{\nu\mu} + Q\bar{\psi}\gamma^\mu A_\mu \psi \tag{2.12}$$

This is consistent with what we observe in nature, i.e. that the rest mass of the photon is zero.

2.6 The Mathematical Framework of the Strong Interaction

The strong interaction is described by a non-Abelian gauge theory known as Quantum Chromo Dynamics (QCD). QCD is based on the gauge group SU(3). The free Lagrangian density for a quark field q is

$$\mathcal{L} = \sum_{j=1}^{6} \bar{q_j}(i\gamma^\mu D_\mu - m)q_j,$$

where $q_j = (q_r, q_b, q_g)^T_j$, with $j = 1, ..., 6$ being the color triplet corresponding to the six quark flavors. Requiring the Lagrangian to be invariant under SU(3) transformations corresponds to

$$q(x) \to Uq(x) \equiv e^{-ig\alpha_a(x)T_a}q(x),$$

where U is an arbitrary 3×3 unitary matrix, the α_a are arbitrary parameters, and g is the strong coupling constant which determines the strength of the interaction between colored quanta. Parameter $\alpha_s = \frac{g^2}{4\pi}$, and $T_a = \frac{\lambda_a}{2}$ with $a = 1, ..., 8$ being the generators of the SU(3) group. The λ_a are the set of linearly independent traceless 3×3 matrices called Gell-Mann matrices. The generators T_a satisfy the commutation relation $[T_a, T_b] = if_{abc}T_c$, where the real numbers f_{abc} are the structure constants of the SU(3) color group.

In order to satisfy SU(3) local gauge invariance, eight gauge fields G^a_μ, the gluon fields, are introduced. These are written as

$$G^a_\mu \to G^a_\mu - \frac{1}{g}\partial_\mu\alpha_a - f_{abc}\alpha_b G^c_\mu.$$

The Lagrangian density transform as

$$\mathcal{L} = \bar{q}(i\gamma^\mu D_\mu - m)q - g(\bar{q}\gamma^\mu T_a q)G^a_\mu,$$

where the covariant derivative used is

$$D_\mu = \partial_\mu + igT_a G^a_\mu$$

and $T_a G^a_\mu$ is in analogy to gauge field A_μ and g to e from QED. We can define a term $J^{a,\mu} = (g\bar{q}\gamma^\mu T_a q)$ in the Lagrangian which describes the interaction of the currents with the gauge fields G^a_μ. Adding the gauge invariant kinematic terms for each of the G^a_μ gauge fields, the final gauge invariant QCD Lagrangian density is given as

$$\mathcal{L}_{QCD} = -\frac{1}{4}G^a_{\mu\nu}G^{\mu\nu}_a + \bar{q}(i\gamma^\mu D_\mu - m)q$$

where $G^a_{\mu\nu}$ is the gluon field tensor

$$G^a_{\mu\nu} = \partial_\mu G^a_\nu - \partial_\nu G^a_\mu - g f^{abc} G^b_\mu G^c_\nu.$$

The Lagrangian contains terms corresponding to self-interaction between the gauge fields, forming three and four gluon vertices. The coupling strength of QCD decreases as the energy scale increases which leads to a number of interesting features and behaviours of quarks and their interactions, such as quark confinement and asymptotic freedom.

2.7 Heavy Quark Effective Theory

Why do we need Non-Perturbative Theory? In high Q^2 interactions in particle physics, the quarks and gluons behave as free particles. Thus is called asymptotic freedom. The strong coupling α_s becomes so small that it is possible to use a perturbative expansion in powers of α_s to describe Quantum Chromodynamics (QCD) interactions at high energies. This approach is known as perturbative QCD. For low Q^2 interactions, we cannot use perturbative theory, as α_s approaches unity or greater. The series can no longer be assumed to converge. In order to work at non-perturbative QCD scales (energy scale $<$ 200 MeV), we need non-perturbative theories.

To describe the binding of quarks in a hadron, which is a low energy interaction, we typically exploit some symmetry of QCD rather than attempting a dynamical calculation. Non-perturbative theories such as lattice QCD, $1/\mathrm{N}_c$ expansions, and effective theories take advantage of symmetry and simplify the problem.

Heavy Quark Effective Theory assumes an infinite mass for the heavy quarks and is just a general quantum field theory based on the principles of relativity and

quantum mechanics but without the restriction of renormalizability. HQET can be tested using experimental measurements of masses and widths of heavy baryons.

When the Compton wavelength ($1/\mathrm{m}_Q$) of a heavy quark bound inside a hadron is much smaller than the typical hadronic distance of about 1 fm, the heavy quark mass is unimportant for the low energy properties of the system. HQET is the limit of QCD in which the heavy quark mass, m_Q, goes to infinity with its four-velocity v_μ held fixed. The strong interactions of such a heavy quark with light quarks and gluons can be described as HQET is invariant under changes of the flavor and spin of the heavy quark. In the case of mesons ($\mathrm{Q}\bar{q}$) with flavor quantum numbers, where Q denotes a heavy quark and $\bar{q}$ a light antiquark, the size of the meson is set by the non-perturbative scale of the strong interactions, $\mathrm{r} \sim 1/\Lambda_{QCD} (\sim 1/400$ MeV). By the Uncertainty Principle, the momentum carried by the light degrees of freedom is $p_l \sim \Lambda_{QCD}$. If an amount of momentum δp_l is transferred to the heavy quark, the change in its four-velocity is $\delta v \sim \delta p_l / m_Q \to 0$, in the infinite mass limit. As $m_Q \to \infty$, the strong interactions of the heavy quark become independent of its mass and spin. There exist two quarks in nature to which the ideas of HQET can be applied, the charm quark ($\mathrm{m}_c \approx 1.5$ GeV) and the bottom quark ($\mathrm{m}_b \approx 4.8$ GeV).

2.7.1 QCD Lagrangian for Quark-gluon Interactions

Quark-gluon dynamics are governed by the QCD Lagrangian

$$\begin{aligned} \mathcal{L} &= -\frac{1}{4} G^{\alpha}_{\mu\nu} G^{\alpha}_{\mu\nu} + \sum_q \bar{q} i \not{\mathcal{D}} q + \sum_q \bar{Q} (i \not{\mathcal{D}} - m_Q) Q \\ &= \mathcal{L}_{light} + \sum_q \bar{Q} (i \not{\mathcal{D}} - m_Q) Q \end{aligned}$$

where $G^{\alpha}_{\mu\nu}$ is the gluon field strength tensor, $\not{\mathcal{D}} = \gamma^\mu \partial_\mu$ denotes a covariant derivative, and q and Q are the light and heavy quark fields respectively. To qualify as a heavy

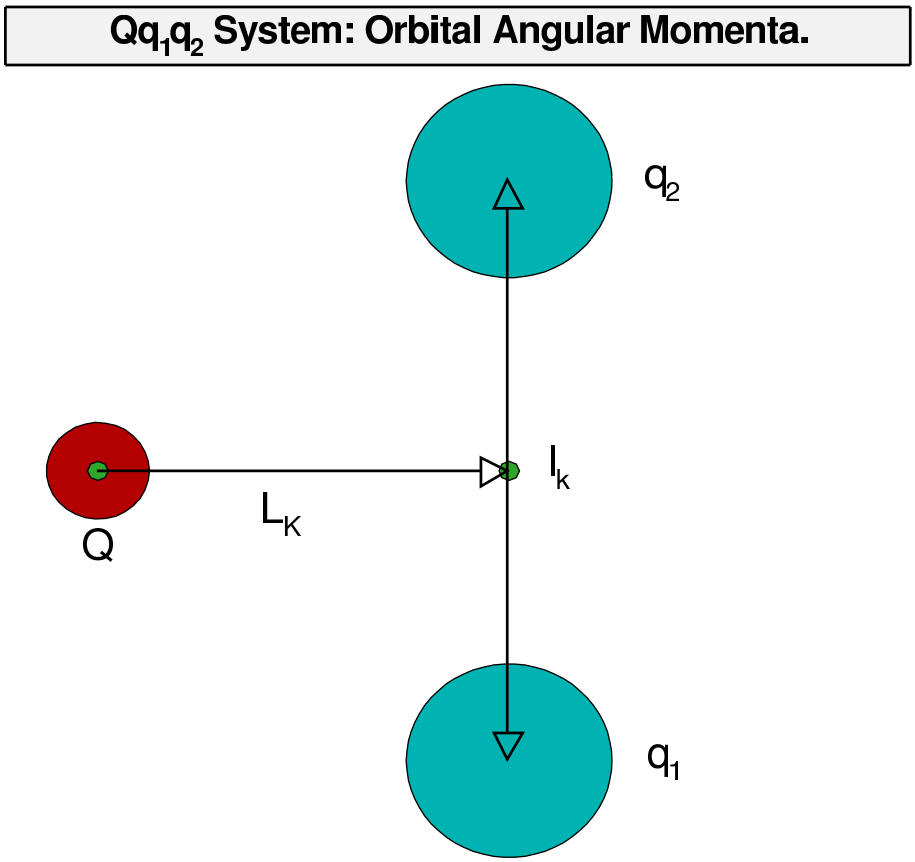

Figure 2.4: Orbital angular momenta of light quarks around the heavy quark Q

quark Q, the mass term m_Q must be much larger than Λ_{QCD}. The hadrons to be considered are composed from one heavy quark Q, a light antiquark $\bar{q}$ or diquark qq, and a gluon cloud which also contains light quark-antiquark pairs. This gluon cloud keeps all these objects together in a colorless bound state.

The Dirac equation for a heavy quark field is given by

$$(i\not{D} - m_Q)Q = 0.$$

The QCD Lagrangian containing only the heavy quark field is given by

$$\mathcal{L}_{heavy} = \bar{Q}(i\not{D} - m_Q)Q.$$

We need to take the limit $m_Q \to \infty$ with fixed four-velocity v^μ. To do this we perform a simple field transformation on the heavy quark field as follows:

$$Q = e^{-im_Q v^\mu x_\mu} Q_\nu$$

$$\not{v} Q_\nu = Q_\nu$$

$$v^\mu = \frac{p_\mu}{m_Q}$$

2.7.2 HQET Lagrangian

Substituting the above two equations into the QCD Lagrangian for the heavy quark field, we get

$$\begin{aligned}
\mathcal{L}_{HQET} &= \bar{Q}_\nu(m_Q\not{v} + i\not{D} - m_Q)Q_\nu \\
&= \bar{Q}_\nu i\not{D} Q_\nu \\
&= \bar{Q}_\nu \left(\frac{\not{v}+1}{2}\right) i\not{D}\left(\frac{\not{v}+1}{2}\right)Q_\nu \\
&= \bar{Q}_\nu \Big[ivD + i\not{v}\Big(\frac{-\not{v}+1}{2}\Big)\Big(\frac{\not{v}+1}{2}\Big)\Big]Q_\nu \\
\mathcal{L}_{HQET} &= \bar{Q}_\nu \big[iv.D\big]Q_\nu
\end{aligned}$$

This is the Heavy Quark Effective Theory Lagrangian for the heavy quark field. There is no explicit m_Q term in the Lagrangian.

2.7.3 Flavor Symmetry Between the b and c Heavy Quarks

The HQET Lagrangian we obtained is zeroth order in $1/m_Q$. Now we are in a position to discuss the two symmetries related to the infinite mass of the heavy quark. Flavor

symmetry relates heavy hadrons containing different heavy quarks. Let us denote the two heavy quarks by b and c. Then the total Lagrangian is given as

$$\mathcal{L}_{HQET} = \bar{Q}_\nu^{(b)}\big[iv.\mathcal{D}\big]Q_\nu^{(b)} + \bar{Q}_\nu^{(c)}\big[iv.\mathcal{D}\big]Q_\nu^{(c)}.$$

These two quarks b and c have same velocity. This Lagrangian is invariant under the transformation,

$$\begin{pmatrix} Q_\nu^{(c)} \\ Q_\nu^{(b)} \end{pmatrix} \rightarrow U \begin{pmatrix} Q_\nu^{(c)} \\ Q_\nu^{(b)} \end{pmatrix},$$

where U is an arbitrary SU(2) matrix. This depicts the flavor symmetry between the b and c quarks.

Any symmetry has in general two consequences, degeneracies and an associated conservation law. The degeneracy implied by the flavor symmetry can be expressed as

$$m_{bqq} - m_b = m_{cqq} - m_c.$$

This degeneracy implies that the mass of the light degrees of freedom is independent of the type of the heavy quark. For the b and c quarks, m_b - m_c = 3.4 GeV, which fairly well agrees with the experimental value.

2.7.4 Spin Symmetry of the Heavy Quarks

Another symmetry appearing in the infinite mass limit is the spin symmetry, which arises because the light degrees of freedom are insensitive to the spin orientation of the heavy quark. The Heavy Quark Symmetry first proposed in [17] and then developed in [18, 19, 20, 21]. This can be seen by performing an arbitrary spin rotation on the HQET Lagrangian which remains invariant; here the heavy quark is assumed to be at rest:

$$Q_\nu = e^{\frac{i}{2}\Sigma\cdot n\theta} Q_\nu,$$

where Σ, n, and θ are the spin operator, the rotation axis, and the rotation angle, respectively. This symmetry implies a degeneracy between the two states of spin J = j $\pm$ 1/2 obtained by coupling the heavy quark spin S = 1/2 with the angular momentum of the light degrees of freedom j. Examples of such states are the B and B^* mesons and the Σ_b and Σ_b^* baryons which are discussed in the next sections.

2.7.5 Spin Symmetry and Flavor Symmetry Breaking

There are $(1/\mathrm{m}_Q)$ corrections to the HQET Lagrangian. In the field equations, there is an approximation given by $\not{v}\, Q_\nu = Q_\nu$, so in order to go beyond leading order in $(1/\mathrm{m}_Q)$, we have to make the most general decomposition:

$$Q = e^{-im_Q v^\mu x_\mu}(Q_\nu + \chi_\nu)$$

$$\not{v} Q_\nu = Q_\nu \;\; ; \quad \not{v}\chi_\nu = -\chi_\nu$$

Now the decomposition is completely general. The field χ_ν corresponds partly to the anti-quark degrees of freedom, and Q corresponds to the heavy quark field. Substituting the above decomposed equation into the QCD Lagrangian density, we get,

$$\begin{aligned}
\mathcal{L}_{heavy} &= \bar{Q}(i\not{\mathcal{D}} - m_Q)Q \\
&= (\bar{Q}_\nu + \bar{\chi}_\nu)(m_Q(\not{v} - 1) + i\not{\mathcal{D}})(Q_\nu + \chi_\nu) \\
&= \bar{Q}_\nu(iv.\mathcal{D})Q_\nu - \bar{\chi}_\nu(iv.\mathcal{D} + 2m_Q)\chi_\nu + \bar{Q}_\nu i\not{\mathcal{D}}_\perp + \bar{\chi}_\nu i\not{\mathcal{D}}_\perp Q_\nu \\
&= \bar{Q}_\nu(iv.\mathcal{D})Q_\nu - \bar{Q}_\nu\frac{\mathcal{D}_\perp^2}{2m_Q}Q_\nu - g\bar{Q}_\nu\frac{\sigma_{\mu\nu}G^\alpha_{\mu\nu}}{4m_Q}Q_\nu + O\Big(\frac{1}{m_Q^2}\Big).
\end{aligned}$$

we expand in powers of $(1/\mathrm{m}_Q)$,

$$\mathcal{L}_{heavy} = \mathcal{L}_0 + \mathcal{L}_1 + ...$$

where the leading order term is the HQET Lagrangian density,

$$\mathcal{L}_0 = \mathcal{L}_{HQET} = \bar{Q}_\nu (iv.\mathcal{D}) Q_\nu$$

and the term $\mathcal{L}_1$ is the next to leading order:

$$\mathcal{L}_1 = -\bar{Q}_\nu \frac{\not{\mathcal{D}}_\perp^2}{2m_Q} Q_\nu - g\bar{Q}_\nu \frac{\sigma_{\mu\nu} G^\alpha_{\mu\nu}}{4m_Q} Q_\nu.$$

The first term in $\mathcal{L}_1$ is the heavy quark kinetic energy. It breaks the flavor symmetry but not the spin symmetry. The second term is the magnetic moment interaction ($\mu_Q \cdot B_c$). It breaks both the spin and flavor symmetries.

2.7.6 Application of HQET to the Λ_b^{*0}

The Λ_b^{*0} baryon (bqq) has a heavy bottom quark and two light quarks. The chromomagnetic moment of the heavy quark with spin $S_Q = 1/2$ is given as

$$\mu_Q = \frac{q}{2m_Q}.$$

As $\mu_Q \to \infty$, the chromomagnetic moment approaches zero, and the spin interaction between the light quarks and the heavy quark is suppressed. This is one of the classic results which allows us to exploit the spin degrees of freedom. The spin S_{qq} of a diquark plus a gluon field and the spin S_Q of a heavy quark are decoupled in HQET. The total angular momentum of the baryon can be written as:

$$J = L + S_Q + S_{qq}.$$

In this case, $S_{[b]} = 1/2$ and $S_{[ud]} = 0$. For S-wave, i.e for no orbital excitations, L= 0. Using these values, we get,

$$J = 1/2^+ \to \Lambda_b^0,$$

which is a singlet ground state. The singlet baryon, with quark content $b[ud]$ according to HQET, has the spin of the heavy quark, $S_{[b]} = 1/2$. Its flavor antisymmetric $[ud]$ diquark has spin $S_{[ud]} = 0$. Under these conditions the b quark and the $[ud]$ diquark make the lowest-lying singlet ground state.

For P-wave orbital excitations, L = 1, total angular momentum gives two states:

$$J = 1/2^- \rightarrow \Lambda_b^{1/2*}$$

or

$$J = 3/2^- \rightarrow \Lambda_b^{3/2*}.$$

In Figure 2.5, orbitally excited states are shown. The Λ_b^0 corresponds to the ground state with zero degeneracy. The other states are the lowest-lying S-wave states that can decay to the singlet via strong processes involving soft pion emissions, provided sufficient phase space is available. The Σ_b and Σ_b^* particles are classified as bottom baryon resonant states. The partners of the Σ_b^* states in the strange quark sector are Σ^* baryon resonances, though in that case the $J = 1/2^+$ state is light enough to decay only weakly or radiatively, and only the $J = 3/2^+$ state $\Sigma(1385)$ decays strongly via the $\Lambda_b^0\pi$ mode.

The Q-value equation for the energy difference associated with the Λ_b^* decaying into Λ_b^0 and two soft pions is given as

$$Q = M(\Lambda_b^* \rightarrow \Lambda_b^0\pi^+\pi^-) - M(\Lambda_b^0) - 2m(\pi^\pm_{PDG})$$

where the pion masses are taken from the PDG [22] and the Λ_b^0 mass is calculated by reconstruction of the proton, kaon, and pion tracks. In Figure 2.6, number of candidates per 3 MeV versus Q-value is plotted for the Σ_b^- and Σ_b^+ respectively. The mass resolution of the signal Λ_b^0 and most of the systematic uncertainties cancel in the mass difference spectrum. The full model for the Q-value spectra of all isospin partner states Σ_b^{*+} and Σ_b^{*-} describes two peaks on top of a smooth background with

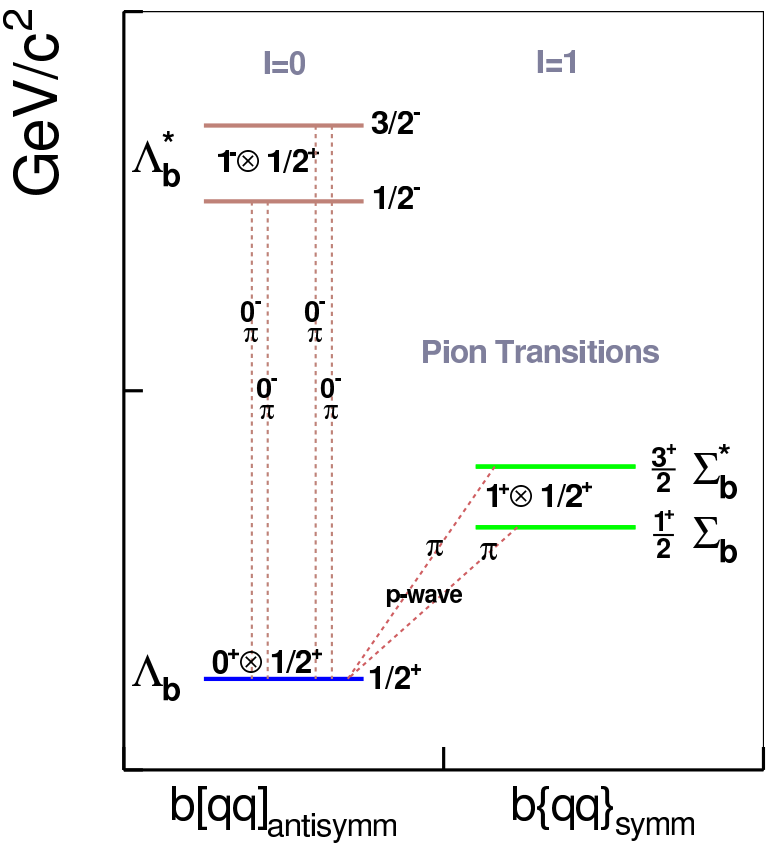

Figure 2.5: Resonant states of the Λ_b^*

a threshold. The two peaks in the bottom figure correspond to resonances $\Sigma_b^{*-1/2}$ and $\Sigma_b^{*-3/2}$ respectively. Using the measured Q-values, isospin mass splittings for the isotriplets of the $J = 1/2^+$ and $J = 3/2^+$ states are calculated, and they agree with the theoretical models. HQET is a very powerful tool to analyze physics at low energies, without solving the details of dynamics at higher energy scales. The framework of HQET is simple and exploits the symmetries of the system, flavor symmetry and spin symmetry. The application of heavy quark symmetry and the

operator product expansion allow for model independent predictions for exclusive and inclusive B decays. The non-perturbative formalism of QCD sum rules has been applied within HQET to calculate the mass spectra of the heavy baryons Λ_b and Σ_b as well as mesons. Remarkable achievements in the theory of heavy quark hadrons result from the approximation that a single heavy quark Q with mass $m_Q \gg \Lambda_{QCD}$ in the heavy hadron can be considered as a static color source in the hadron's rest frame.

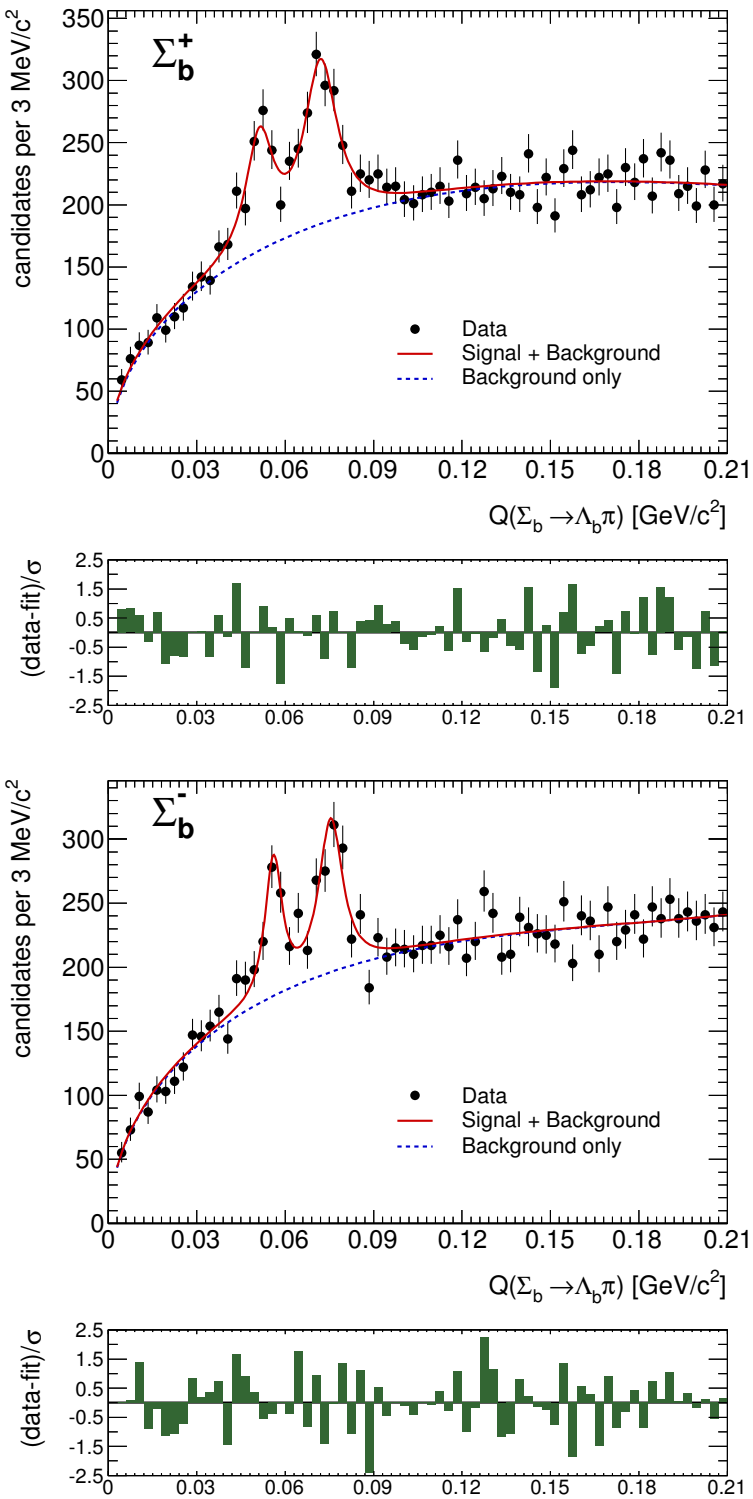

Figure 2.6: The top plot shows the $\Lambda_b^0\pi^+$ subsample, which contains $\Sigma_b^{(*)+}$, while the bottom plot shows the $\Lambda_b^0\pi^-$ subsample, which contains $\Sigma_b^{(*)-}$.

Chapter 3

The Tevatron Accelerator and the CDF Experiment

The data used in these analyses were collected by the Collider Detector at Fermilab (CDF) during Run II of the Tevatron (CDF II). The Tevatron accelerated protons and anti-protons to an energy of 980 GeV each by a chain of accelerators, before colliding them in the center of the CDF and D0 [23] detectors. Prior to the Large Hadron Collider (LHC) turning on in Geneva, it was the world's highest energy hadron collider. The results presented in this work make use of approximately 9.6 fb^{-1} of data collected by the CDF II detector. This chapter gives an overview of the Tevatron accelerator and the CDF detector, focusing on those components of the detector which are mainly used in this analysis.

3.1 The Tevatron Accelerator

The Tevatron was designed to accelerate protons and anti-protons to $\sim$1 TeV of energy. It was built in the early 1980s at Fermilab, and a major upgrade of the

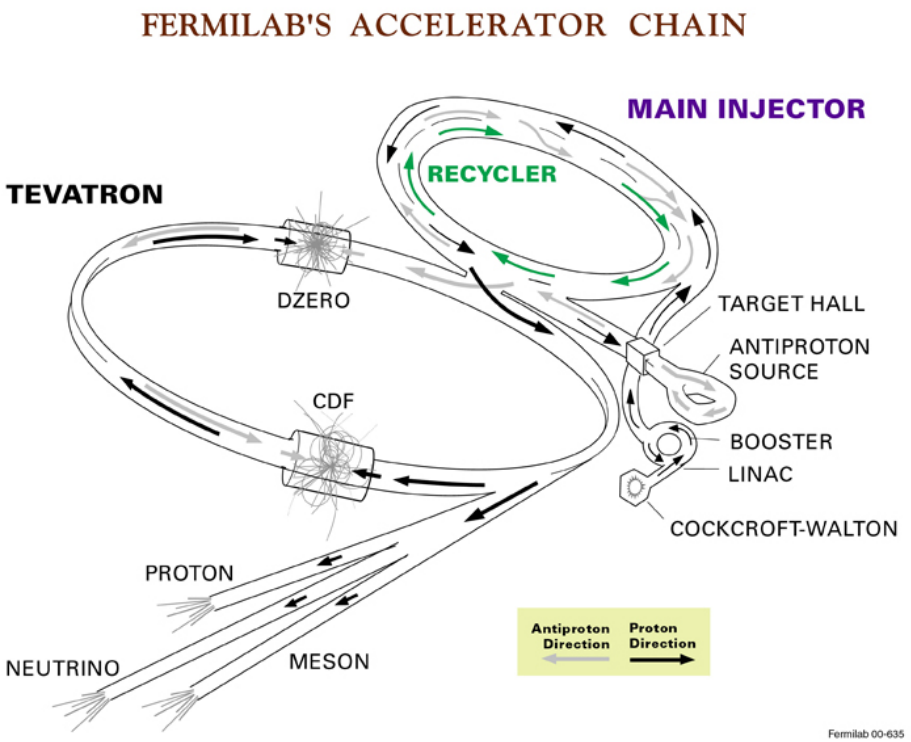

Figure 3.1: The Tevatron accelerator and Main Injector system.

Tevatron took place between September 1997 and March 2001. After that time, the Tevatron operated with a center of mass energy of 1.96 TeV. The Tevatron is a synchrotron of radius 1 km. The schematic diagram of the different stages of acceleration of proton and anti-proton beams is shown in Figure 3.1. In addition to serving the two collider experiments, the accelerator complex also delivers proton beams to test beam facilities and fixed-target and neutrino experiments located at Fermilab.

3.1.1 Proton Production and Acceleration

The protons are accelerated to 980 GeV in multiple stages. The Cockcroft-Walton pre-accelerator is the first accelerator in the complex. Hydrogen gas (H_2) is ionized

by electrical discharges to form H^- ions consisting of two electrons and one proton. The Cockcroft-Walton accelerates the ions to 750 keV using a diode capacitor voltage multiplier. The H^- ions are separated from the other debris of particles using a magnetic field, and they are accumulated every 66 ms, which segments the beam into bunches. Electrostatic acceleration creates a potential difference between a source of charged particles and a target point, and the upper energy limit is set by electrostatic breakdown in air; this is approximately 10 MeV. The H^- ion bunches are subsequently fed into a 150 m long linear accelerator (linac) which uses radio-frequency (RF) accelerating cavities. The RF cavities overcome the problem of electrostatic breakdown by repeatedly passing charged particles through an acceleration gap, each time imparting additional energy. The linac consists of twelve RF cavities operating at 805 MHz, and accelerates the H^- ions to 400 MeV. The beam is focused in the plane transverse to the direction of their motion using quadrapole magnets.

Before entering the Booster, a 75 m radius synchrotron, the ions are passed through a thin carbon fiber foil to strip the two electrons, leaving only the protons. The Booster accelerates the resulting proton beam from 400 MeV to 8 GeV in just 67 ms, hence its name. These 8 GeV protons are passed to the Main Injector, a multi-purpose synchrotron of 1 km diameter, seven times larger than the Booster, with 18 RF cavities. It can accelerate the protons to two different energies, If the protons are to be used to produce anti-protons, they are accelerated to 120 GeV, if they are to be injected into the Tevatron, they are accelerated 150 GeV.

3.1.2 Antiproton Production and Acceleration

The 120 GeV protons from the Main Injector are collided with a fixed nickel alloy target to produce anti-protons and a spectrum of secondary particles. Approximately 20 anti-protons are produced for every 10^6 protons incident on the nickel target.

The secondary particles are focused into a parallel beam using a cylindrical lithium lens and then using a pulsed dipole magnet, an 8 GeV anti-proton bunched beam is extracted. This bunched beam contains anti-protons with a large momentum spread. It is transferred to the Debuncher, a triangular synchrotron, to make a continuous beam. Stochastic cooling is applied to reduce the transverse energy of the anti-protons, which reduces the spread in the momentum. Anti-protons are stored in the Accumulator, which is also a 8 GeV synchrotron housed in the same tunnel as the Debuncher. The 8 GeV anti-protons are then moved to the Recycler (which is housed in the same tunnel as the Main Injector) for further stochastic and electron cooling. The Recycler can store 5×10^{12} anti-protons which are subsequently sent to the Main Injector where they circulate in the direction opposite to the protons and are accelerated to 150 GeV.

3.1.3 Tevatron Performance and Statistics

The proton and the anti-proton beams from the Main Injector are passed into the Tevatron ring of 1 km radius. There are 36 bunches each of protons and anti-protons. Each of the bunches contains 3×10^{11} protons, and they are separated by 396 ns. The Tevatron is a synchrotron which employs superconducting magnets and eight accelerating cavities to accelerate the proton and anti-proton bunches in opposite directions from 150 GeV to 980 GeV.

The higher the energy achieved in the particle accelerators, the higher are the chances of probing new physics associated with the experiment. The amount of data generated during the collisions also increases the chances of observing new phenomena and decreases the statistical uncertainty of the measured physical quantity. The performance of the particle collider is measured by the instantaneous luminosity which is defined as

$$L = \frac{f n N_p N_{\bar{p}}}{2\pi(\sigma_p^2 + \sigma_{\bar{p}}^2)} F(\frac{\sigma_l}{\beta^*}).$$

Here f is the RF bunch revolution frequency, n is the number of bunches, $N_p(N_{\bar{p}})$ are the number of protons (anti-protons) per bunch, and $\sigma_p, \sigma_{\bar{p}}$ are the root-mean-squared widths of the beams at the interaction points. The form factor F corrects for deviations from the ideal bunch shape and depends on the bunch length σ_l and the beta function β^* at the interaction point. The β function is a measure of the beam width, and is proportional to the beam's x and y spread in phase space.

The rate at which protons and anti-protons interact inside the detector collision regions can be expressed as,

$$R = \sigma L$$

where σ is the interaction cross section of a process. The interaction rate can be maximized by maximizing the instantaneous luminosity. The integrated luminosity, defined as $\mathcal{L} = \int L dt$, is a measure of the total amount of data collected, and is usually given in units of fb^{-1}, inverse femto-barns, where a barn is equal to 10^{-24} cm. The integrated luminosity delivered by the Tevatron over the period of Run II and the integrated luminosity acquired by the CDF detector are shown in Figure 3.2.

The improvements to the accelerator in Run II included the replacement of the Main Ring with the Main Injector and commissioning of a new anti-proton storage ring with the Recycler. These improvements increased the instantaneous luminosity up to $L \approx 4 \times 10^{32}$ $\text{cm}^{-2}\text{s}^{-1}$. The Tevatron delivered more than 12 fb^{-1} of integrated luminosity.

3.2 The CDF Detector in Run II

The upgraded Collider Detector at Fermilab (CDF II) in Run II was designed to study a broad range of physics phenomena, from top, QCD, electroweak, and heavy flavor physics to searches for the Higgs, SUSY, and new exotic particles. It is equipped

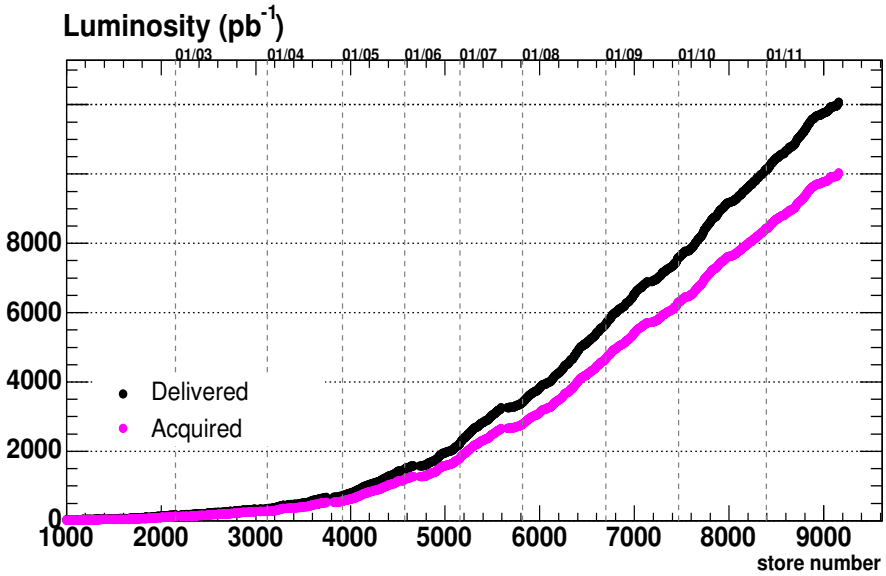

Figure 3.2: The integrated luminosity delivered and acquired by CDF over the period of Run II.

with the Silicon Tracking system, drift chamber tracking, a time-of-fight detector, a solenoid, calorimeters, and muon detectors, as well as triggers and data acquisition (DAQ) systems. The CDF detector has both azimuthal and forward-backward symmetry with respect to the interaction point. The detector has many components to measure the energy, momentum, and trajectory of charged particles produced in $p\bar{p}$ collisions. An extensive detailed description of the CDF Run II detector can be found in its technical design report at [24]. A schematic view of the CDF II detector system is shown in Figure 3.3.

The Run II upgrade to the CDF detector was designed to handle the luminosity enhancement and the increased center-of-mass energy of the Tevatron collider. Its inner subsystems consist of the Silicon Vertex Detectors, the Central Outer Tracker, and the superconducting solenoid. The tracking system is designed to measure the momentum and the trajectory of charged particles. The innermost layers are surrounded by the Calorimetry System, which consists of the central and forward elec-

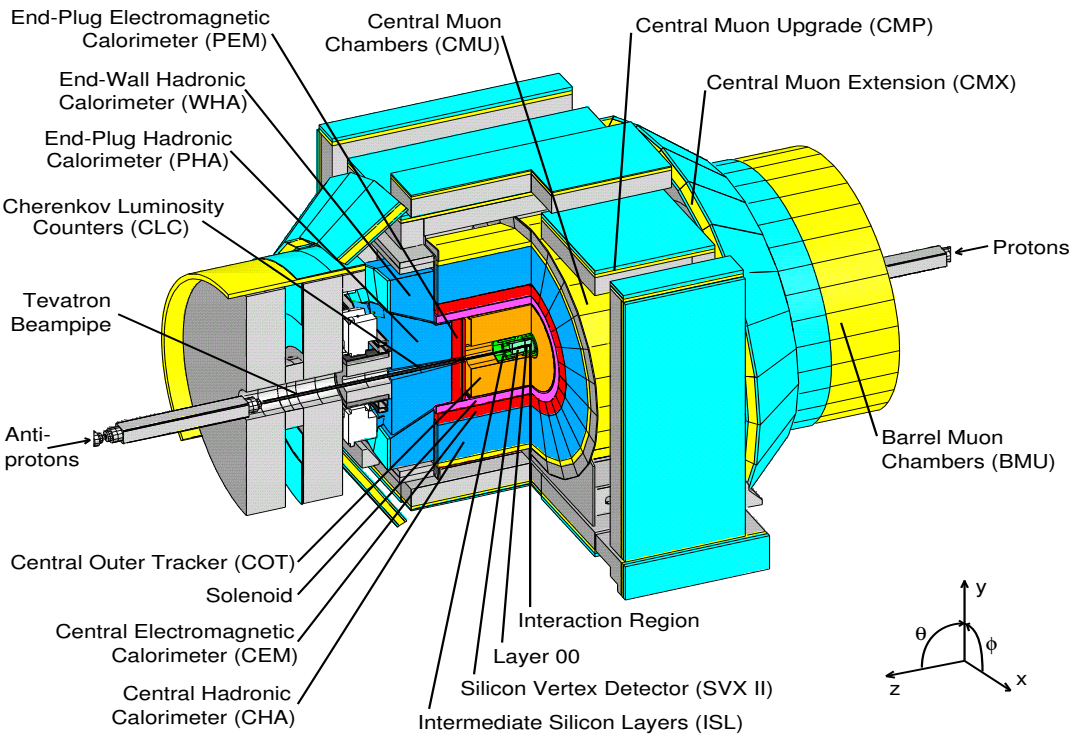

Figure 3.3: An overview of the Collider Detector at Fermilab in its Run II configuration.

tromagnetic and hadronic calorimeters and finally the outermost Muon Chambers. This section provides an overview of the various CDF sub-detectors, with emphasis on the silicon tracking system and central drift chamber. Before the discussion of detector details, it is useful to define the coordinate system and the parameters that describe the detector geometry and the $p\bar{p}$ collisions. An elevation view is shown in Figure 3.4.

3.2.1 Standard Definitions and Coordinate Systems

The origin in the three CDF coordinate systems is defined at the center of the drift chamber. In the Cartesian coordinate system, the z-axis is parallel to the $p\bar{p}$ beam

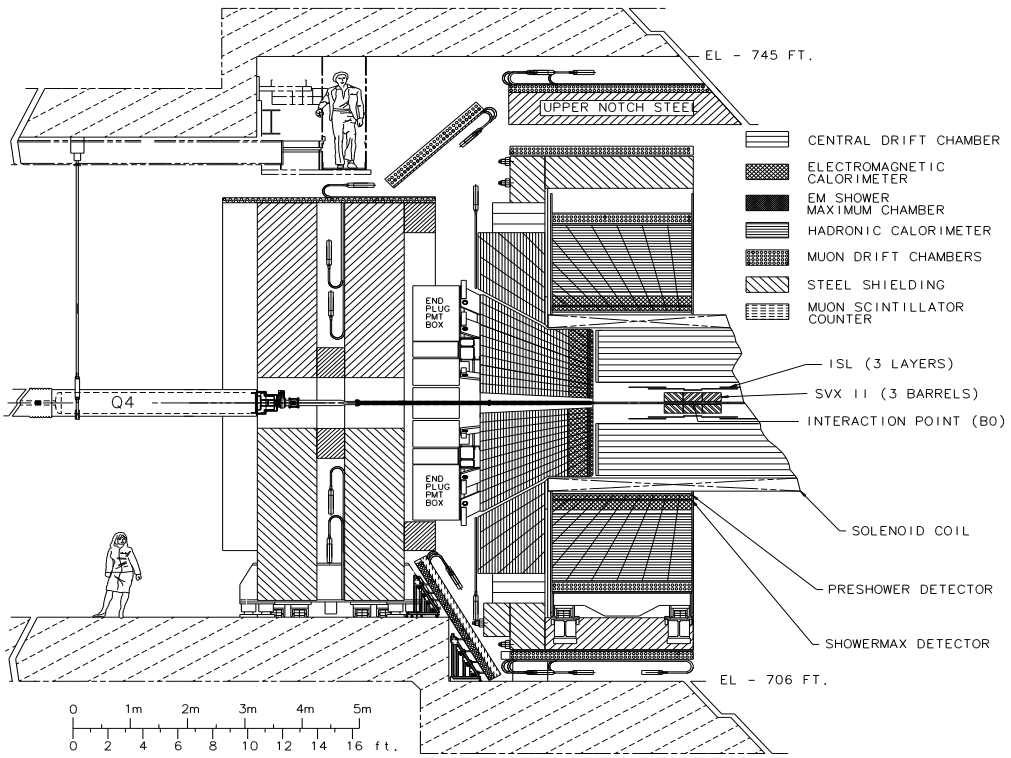

Figure 3.4: An elevation view of the CDF Run II detector.

line with the increasing positive axis in the direction of the proton beam. The y-axis is defined as vertically upwards and the x-axis is radially outwards from the Tevatron ring. These are shown in Figure 3.5.

The transverse plane is the $x-y$ plane, and the longitudinal direction is parallel to the z-axis. The other two coordinate systems, cylindrical (r, ϕ, z) and polar (ρ, ϕ, θ) are also useful due to the detector's approximate axial symmetry and because the unpolarized $p\bar{p}$ beams make interactions invariant under azimuthal rotation around the beam line. The polar angle θ in the cylindrical coordinate system is measured from the proton beam axis and the azimuthal angle ϕ, from the x-axis around the beam. Available fraction of the momentum of the colliding hadrons (protons) is carried by the quarks and gluons. Hence in each collision, the center of the mass

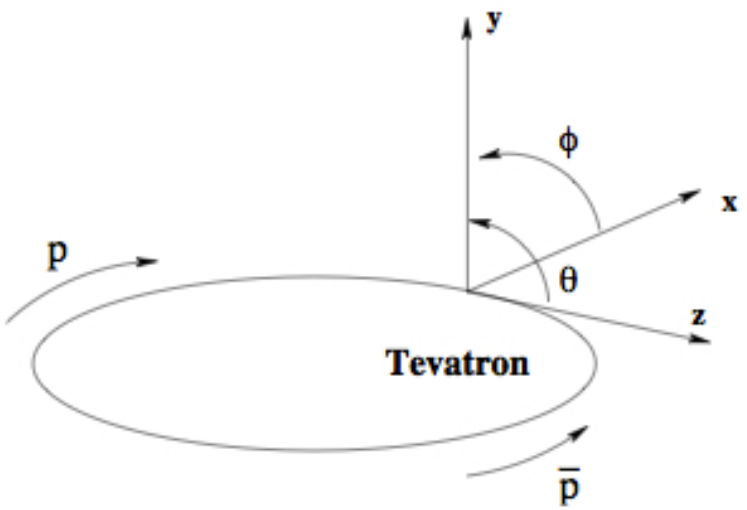

Figure 3.5: CDF coordinate system.

system is boosted along the z direction by an unknown amount, and the actual constituent partons will not be traveling at the same velocity. Thus, the number of particles per unit angle ($dN/d\theta$) will not be the same for particles with different velocity. The Lorentz invariant kinematic variable is rapidity, defined as

$$y \equiv \frac{1}{2} \ln \left[\frac{E + |\vec{p}| \cos\theta}{E - |\vec{p}| \cos\theta} \right],$$

where E and $\vec{p}$ are the particle's energy and momentum, respectively. The rapidity measurement depends on energy and momentum, which again requires precise particle identification to obtain each particle's mass. This is not always possible. In the relativistic limit, $pc \gg mc^2$, we approximate the rapidity by the pseudorapidity η, which is defined as

$$\eta \equiv -\ln \tan(\theta/2).$$

The pseudorapidity is a function of transverse momentum (p_T) and longitudinal

momentum (p_z) because the polar angle θ depends on these momenta through the relation, $\tan\theta = \frac{p_T}{p_z}$. The region of the detector where $|\eta|$ is very high (trajectories near the beam axis) is called the "forward region", and the region of the detector where $|\eta| \sim 0$ is called the "central region".

3.2.2 The Tracking System Parameters

A charged particle follows a helical trajectory through the region of constant magnetic field of 1.4 T inside the CDF tracking system. The helical path of a charged particle can be described by 5 parameters as follows:

- **Helix half-curvature C**: the track curvature in the $r-\phi$ plane is defined as

$$C = q/2R,$$

  where R is the radius of the helix and q is the charge of the particle. The transverse momentum of the charged particle can be related to its half-curvature by $p_T = \frac{cB}{2|C|}$, where c is the speed of light and B is the strength of the homogeneous magnetic field.

- **Helix pitch** λ: this is defined as $\lambda = \cot\theta$, where θ is the polar angle at the point of closest approach to the beam axis (z-axis).

- **Impact parameter** d_0: the signed impact parameter of the track, d_0, is the distance of closest approach to the primary vertex. It is defined as

$$d_0 = \frac{\hat{z} \cdot (\vec{r} \times \vec{p_T})}{|\vec{p_T}|},$$

  where $\hat{z}$ is the unit vector along the z-axis, p_T is the transverse momentum, and $\vec{r}$ is the vector pointing from the primary vertex to the reconstructed particle trajectory at the point of closest approach to the primary in the $r-\phi$ plane.

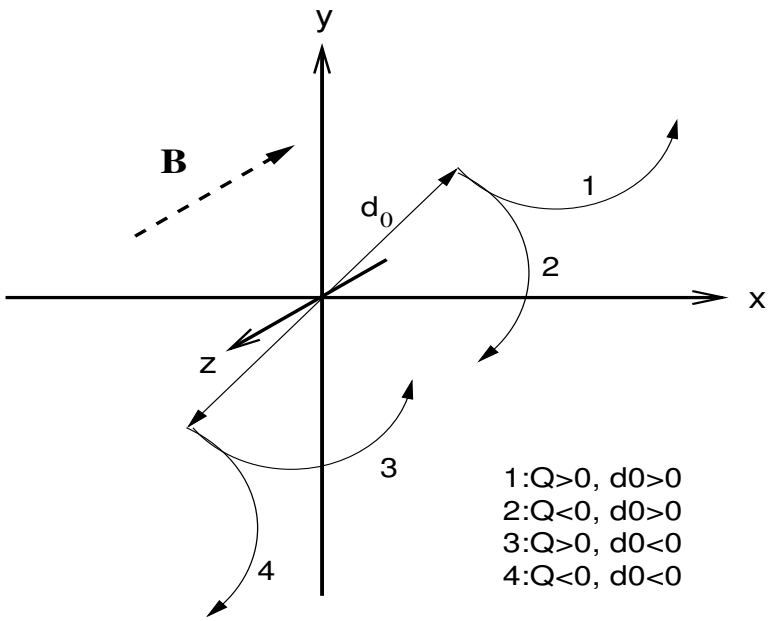

Figure 3.6: Signs of the impact parameter for positively and negatively charged particles in the magnetic field.

- Azimuthal angle ϕ_0: this is the coordinate of the particle trajectory at the point of closest approach to the beam.

- z_0: the position along the z-axis at the point of closest approach to the beam.

If a track has a positive or negative charge and the reference point is outside or inside the circle of the track respectively, then the impact parameter (D) has a positive sign, see Figure 3.6.

Other variables that are used in collider physics experiments are:

- **Opening angle** ΔR: for any two tracks, the opening angle ΔR between them is defined as

$$\Delta R = \sqrt{\Delta\eta^2 + \Delta\phi^2}$$

- **Transverse momentum p_T and transverse energy E_T**: the transverse momentum and energy are the components of the particle's momentum and energy projected into the transverse plane perpendicular to the z-axis and are defined as $p_T = p \cdot \sin\theta$ and $E_T = E \cdot \sin\theta$ respectively.

- **Transverse decay length L_{xy}**: the point of the $p\bar{p}$ collision is called the primary vertex. Any vertex that does not overlays the interaction region is called a secondary vertex. The transverse decay length L_{xy} is the distance a particle travels in the transverse plane from the primary vertex before decaying. It is defined as
$$L_{xy} = \vec{r} \cdot \hat{p_T}.$$

- **Proper decay length ct**: the proper time elapsed in the particle's reference frame between creation (primary vertex) and decay (secondary vertex) is defined as
$$ct = \frac{L_{xy} \cdot Mc}{p_T}$$
where M is the mass of the particle and c is the speed of light.

3.2.3 Silicon Tracking Systems

The CDF detector has two kinds of tracking systems. The inner tracking system is comprised of three silicon sub-detectors, the innermost *Layer 00* (L00), followed by the *Silicon Vertex Detector* (SVX II), and finally the *Intermediate Silicon Layers* (ISL). The *Central Outer Tracker* (COT) constitutes the outer tracking system, a wire-based drift chamber. The tracking system reconstructs charged particle trajectories that traverse the tracking volume enclosed by a superconducting, 1.4T, solenoidal magnet that is 2.8m in diameter and 3.5m long. The longitudinal view of the CDF II tracking system is shown in Figure 3.7, and the η coverage of the silicon detector system is shown in Figure 3.8.

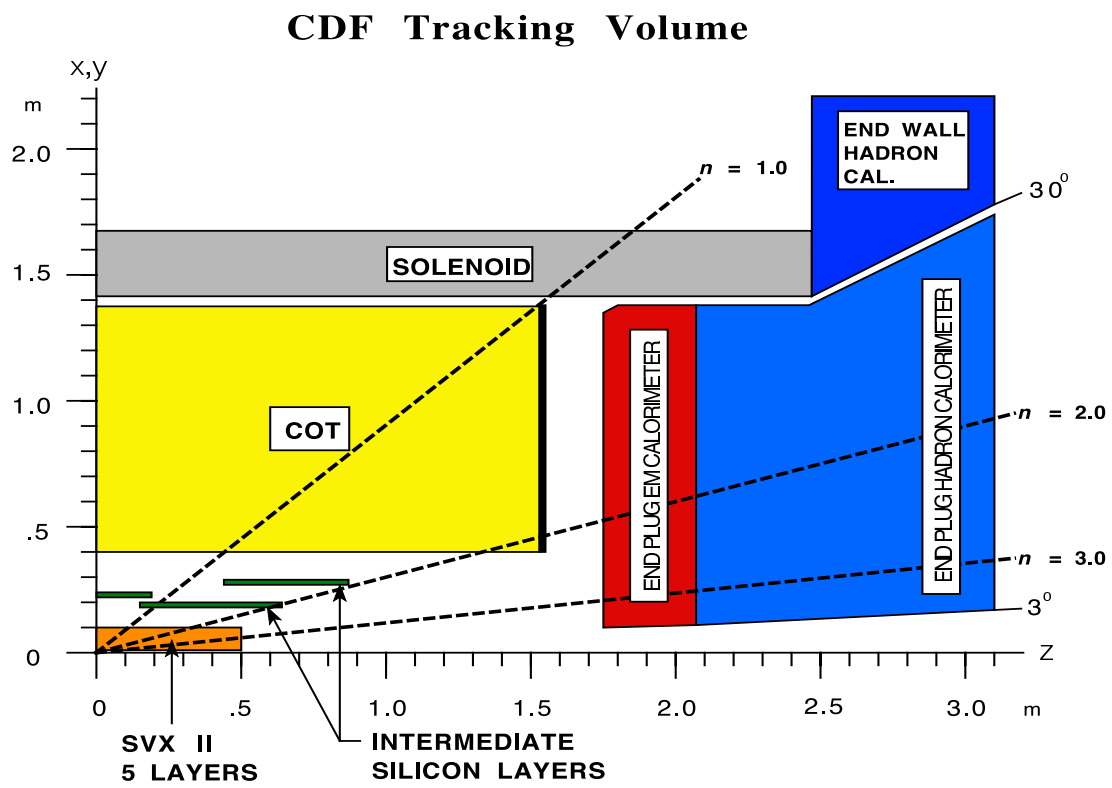

Figure 3.7: Longitudinal view of one quadrant of the inner portion of the CDF II tracking volume. Its main components are the Solenoid, the Central Outer Tracker (COT), the silicon micro-strip detectors ISL, and the SVXII.

The silicon based detectors can withstand the high radiation dose found near the beam pipe. The silicon is a semiconductor which provides fast electronic readout and can be finely segmented to give high precision position measurements of the charged particles. The silicon strip is a reverse biased p-n junction which creates an electron-hole pair when a charged particle passes through it. The bias voltage increases the gap between the conduction band and the valence band across the p-n junction and reduces the leakage current from thermal excitation. Electrons drift towards the n-side while holes drift to the p side of the semiconductor. One of the advantages of using a silicon detector over a drift chamber is that the electron-hole creation energy in the silicon is about 3 eV, while the ionization energies are about

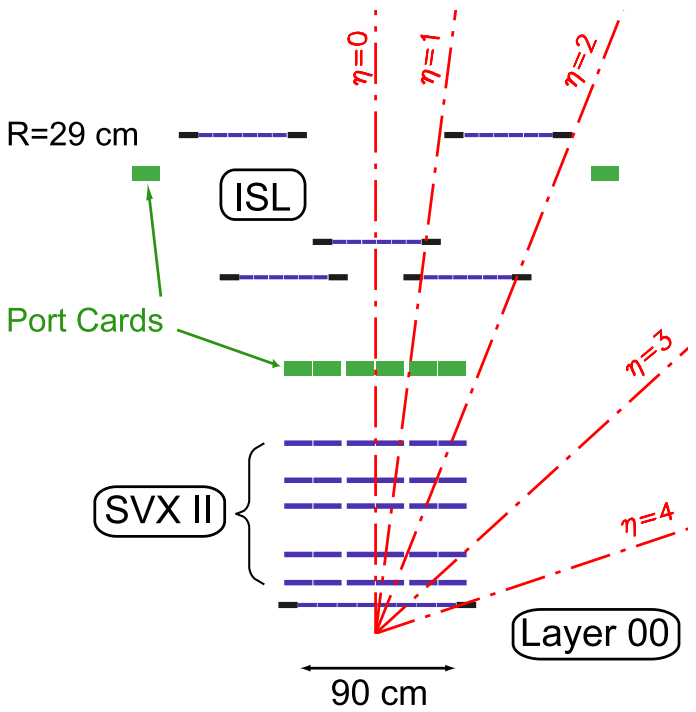

Figure 3.8: The coverage and a cross-sectional view of the silicon detectors at CDF II showing the three sub-detector systems in the $r-z$ plane.

1015 eV for the drift chamber gas. Thus, more electrons are produced per track length, which gives better energy and position resolution and signal to noise ratio. The charge deposition is read out on one or more strips to localize the signal, and this gives $r-\phi$ location.

3.2.4 Layer 00 (L00)

The L00 is a single-sided silicon detector layer directly on the beryllium beam pipe at alternating radii of 1.35 and 1.62 cm, as shown in a cross-sectional view in Figure 3.9. It has single-sided strips of AC coupled p-in-n silicon providing measurements in the $r-\phi$ coordinate. Since L00 is close to the interaction region, it significantly enhances CDF's impact parameter resolution. The hit spatial resolution is 6 μm.

The full detector spans 80 cm in the z direction, sufficient to cover the approximately Gaussian distribution of the primary vertex, which is centered at $z = 0$ and has width $\sigma_z \sim 30$ cm. The silicon sensors of L00 are radiation-hardened and capable of withstanding a high bias voltage ($\sim$500 V). This helps to fully deplete the sensor for readout even after radiation damage and hence increases the lifespan of data-taking. A cross-sectional view of the silicon subsystem is shown in Figure 3.9.

3.2.5 Silicon Vertex Detector II (SVX II)

The SVX II consists of five double-sided layers of 300 μm thick silicon strip sensors arranged in three 29 cm long cylindrical barrels with beryllium bulkheads at both ends for support and cooling of the detectors. The double-sided layers provide two dimensional information on the locations of hit clusters created by an ionizing particle passing through the detector. Each SVX II layer is made of 12 ladders, organized into 30° wedges in ϕ, between radii of 2.4 and 10.7 cm. Three of the layers have a stereo angle of 90°, and the second and fourth have stereo angles of $-1.2°$ and $+1.2°$ respectively. The layers are positioned at increasing radii as shown in the right side of Figure 3.9. Each layer is composed of four silicon sensors, which are aligned length-wise in a ladder structure with readout electronics mounted onto the ends of the ladders. The single hit resolution of the SVXII is about 9 μm. A water-glycol system cools the whole SVX II system to roughly a temperature of $10 - 15$°C.

3.2.6 Intermediate Silicon Layers

The Intermediate Silicon Layers (ISL) consists of three layers [25] as shown in Figure 3.8. The ISL layers are double-sided silicon layers with a stereo angle of 1.2°. Similar to SVX II, one side of each layer provides tracking information in the $r - \phi$ plane while the other side provides tracking information in the $r - z$ plane. The cen-

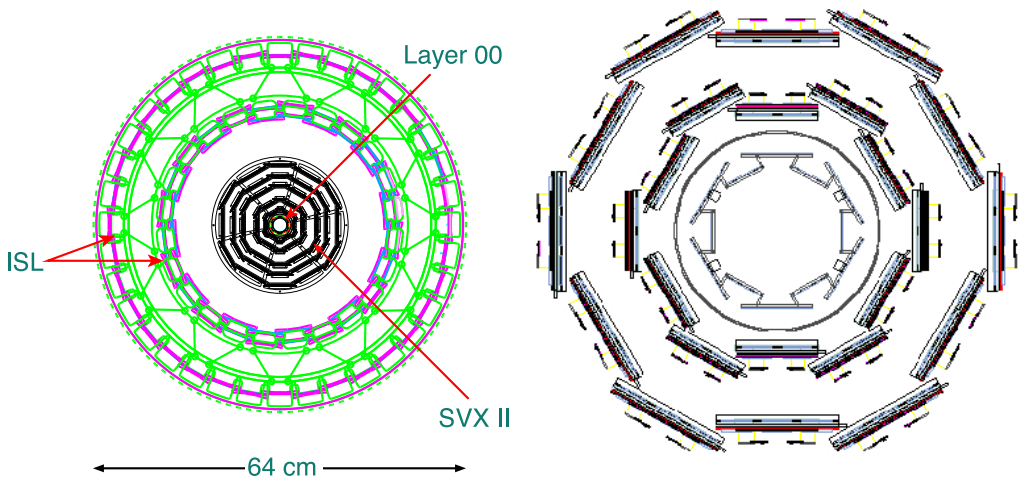

Figure 3.9: Left: An end view of the inner tracking system including the SVX II cooling bulkheads. The silicon detectors represented in black are SVX II layers, the pink are ISL layers and the red at the center are L00 layers. Right: End view of the L00 and the first two layers of the SVX II.

tral region's layer at $r = 22$ cm covers $|\eta| < 1$. This layer is useful for extrapolating tracks from the COT into the SVX II. The forward region's layers at $r = 20$ and $r = 29$ cm covers $1 < |\eta| < 2$. At high $|\eta|$, a track will not traverse all the layers of the COT, hence the hits from the ISL become more important.

3.2.7 Central Outer Tracker

The Central Outer Tracker (COT) is an open-cell cylindrical multi-wire drift chamber that extends from a radius of 43 cm to 132 cm from the beam pipe and has a length of 310 cm. It is the main tracking system at CDF II and provides accurate tracking information in the $r-\phi$ plane for the measurement of the transverse momentum, p_T, of a particle. The drift chamber contains 96 sense wires which are radially grouped into 8 concentric superlayers for particle reconstruction in the central region, $|\eta| < 1$, with transverse momenta as low as 400 MeV/c. Each superlayer is divided into

supercells in ϕ, each of which has 12 sense wires as shown in Figure 3.10. A supercell is defined as one sense plane (with active read-out) with two adjacent field planes, which are grounded as shown on the right side of Figure 3.10. The left side of Figure 3.10 shows the layout of supercells in the second superlayer of the COT. The supercells consist of sense and potential wires (for electric field shaping) and a field (cathode) plane on either side. The sense and potential plane wires are 40 μm in diameter and are made of gold plated tungsten. The field sheet is 6.35 μm thick Mylar with vapor-deposited gold on both sides. The drift chamber is filled with a nearly equal mixture of argon and ethane gas.

When a charged particle produced in $p\bar{p}$ collisions travels through a COT cell, the gas is ionized. The wires in the COT produce an electric gradient and this causes the electrons to drift towards the nearest sense wires. The resulting charge is collected at the sense wire and the signal is detected through the read-out electronics. Collisions between the electrons and atoms of the gas in the very high electric field region close to the sense wire cause an avalanche multiplication of charges. The trajectories of drifting electrons are deflected from the electric field lines by the presence of the solenoidal magnetic field. To compensate for this, the cells are tilted by a Lorentz angle of 35° with respect to the radial direction. The electrons have a sufficient drift velocity that the maximum drift time is 100 ns. This is smaller than the bunch crossing rate, so tracks from successive bunch crossing interactions are separated. The hit position resolution is approximately 140 μm. The COT information for a charged particle can also be used in event reconstruction by matching the hits in the silicon detector to the pattern of hits on the sense wires in the COT. The hits found in the COT, SVX II, ISL, and L00 detectors allow the determination of track trajectories using a variety of algorithms depending on the order in which the information from different tracking systems is processed.

The transverse momentum of a charged particle produced in $p\bar{p}$ collisions is de-

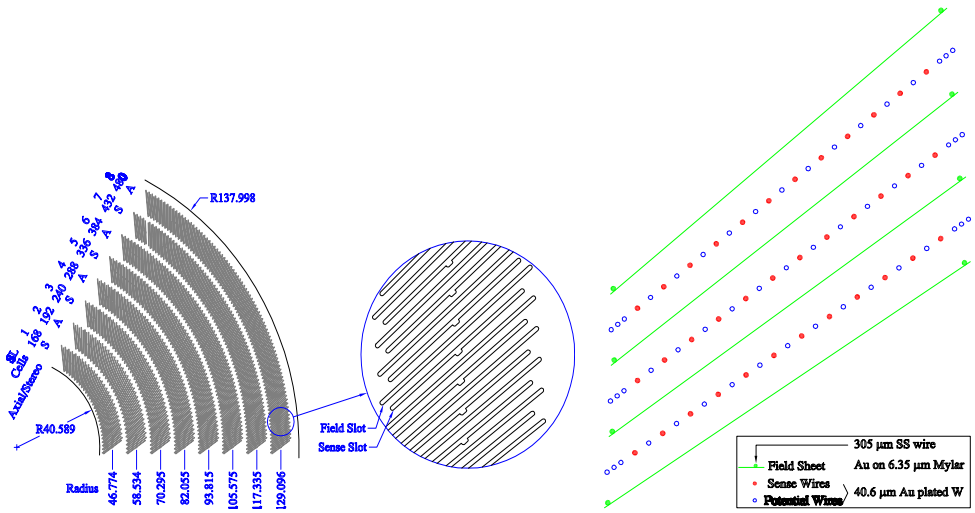

Figure 3.10: Left: End view of the field sheet and sense wire planes in a 1/6-th section of the 8 COT superlayers. The even super layers are axial and the odd super layers are stereo. Right: Layout of wires in three supercells in the second superlayer of the COT which runs along the beam direction.

termined from the curvature, C, of its trajectories as it bends in the magnetic field inside the tracking chamber. The relation between the transverse momentum of a particle and its curvature in a magnetic field, B_z, is given by:

$$p_T = \frac{AB_z}{|C|}$$

where $A = 1.5 \times 10^{-3}$ GeV cm/T.

The transverse momentum resolution of the COT is about $\frac{\sigma_{p_T}}{p_T^2} = 0.0015/(\text{GeV/c})$.

In addition to particle tracking, the COT provides particle identification information. The ionization energy loss per unit track length (dE/dx) of a charged particle is related to its drift velocity and hence, the COT information can be used for identifying charged particles by extracting the particle's mass by combining velocity and momentum measurements.

Chapter 4

Trigger System and Data Acquisition (DAQ)

The rate of collisions at the CDF interaction point is determined by the beam structure and is 1.7 MHz. Each event would contain 200 Kb of information if it were read out and written to tape. It is not possible to record such a volume of data. Currently approximately 120 events can be written to tape per second, and therefore the trigger must be able to provide a rejection factor of 14000. The CDF trigger system consists of three trigger levels, and it is shown in Figure 4.1.

4.1 Level 1 Trigger

The Level 1 is a synchronous trigger system. On every bunch crossing, this trigger reads out the event information from the detector, stores it in the pipeline and makes a decision on an earlier event. An event is saved at Level 1, if tracks with p_T above 1.5 GeV are reconstructed by the Trigger Track Processor (XFT) from axial hits in the COT. Track information is distributed by the XTRP for electron, muon and

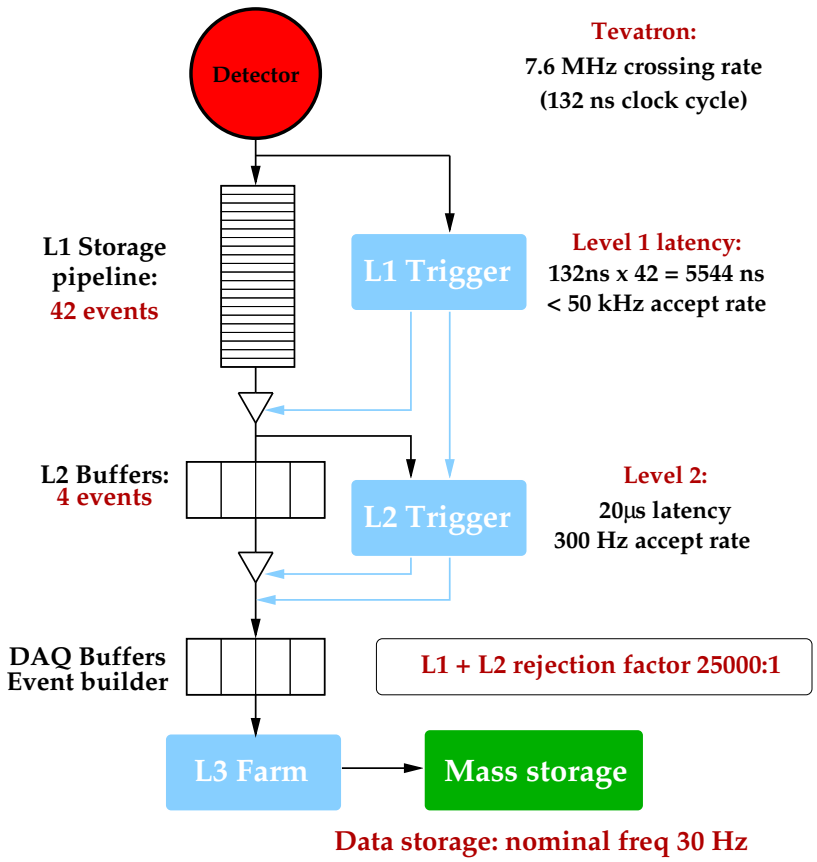

Figure 4.1: A flow diagram representing the CDF trigger and data acquisition system

track triggers. Level 1 reduces the input rate of 2.5 MHz to an output rate around 35 kHz.

4.2 Level 2 Trigger

The Level 2 trigger is an asynchronous system that processes events as they are received from Level 1. At Level 2, the Silicon Vertex Trigger (SVT) associates SVX II $r-\phi$ position measurements with XFT tracks, providing a precise measurement of the track impact parameter d_0. The Level 2 decision is based on Level 1 primitives

as well as on more accurately processed information from the calorimeter, additional information from the shower maximum strip chambers (CES), and information from the axial strips of the silicon vertex detector (SVX II). Decays of heavy flavor hadrons are identified by requiring two tracks with 0.12 mm $< d_0 <$ 1 mm and making an additional cut on the two-track combination. Four event buffers are available and the maximum output rate is reduced to 500 Hz.

4.3 Level 3 Trigger

The Level 3 trigger system is a large array of conventional PC's running the linux operating system. After an event is accepted at Level 2, it has to be read out completely. This operation involves collecting data from several hundred VME Readout Buffers (VRBs). The Event Builder assembles the event from pieces of data from the Level 2 system into complete events. The Level 3 is divided into 16 sub-farms, each consisting of a converter node (running the Event Builder) and 12 to 16 processor nodes. Once the event is built, it is sent to one node in the Level 3 sub-farm. The Level 3 trigger reconstructs the event following given algorithms. These algorithms take advantage of the full detector information and improved resolution not available to the lower trigger levels. This includes full 3-dimensional track reconstruction and tight matching of tracks to calorimeter and muon system information. The Level 3 output rate is approximately 100 Hz.

4.4 Two Track Trigger

The analysis in this dissertation involves examining events that satisfy the displaced Two Track Trigger (TTT) path criteria. The tracks corresponding to the decay products of B hadrons often have a large impact parameter with respect to the

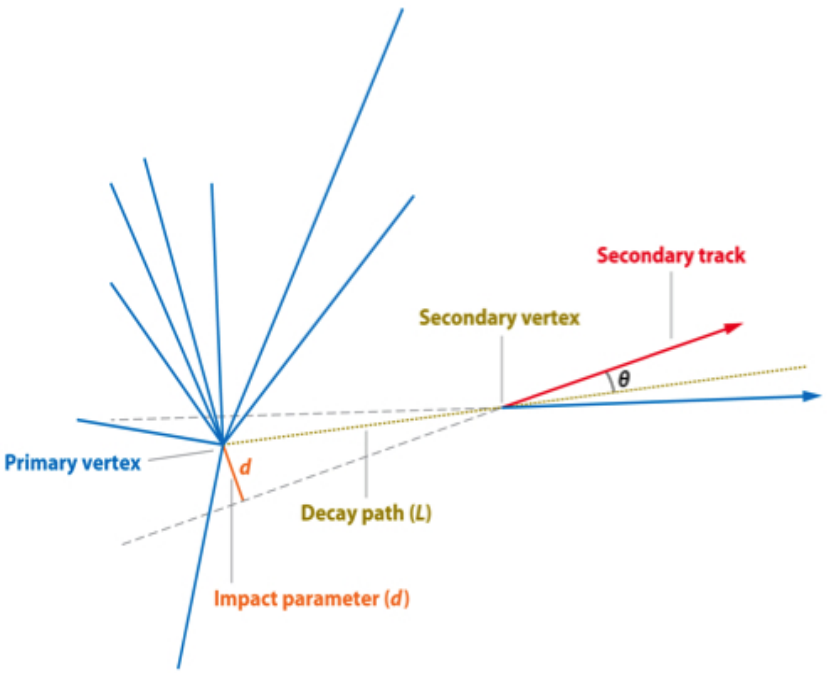

Figure 4.2: When a sufficiently long-lived particle decays after traveling some distance, the trajectories of the decay products do not point back to the collision point. The distance of closest approach of the extrapolated trajectory to the collision point is known as the impact parameter.

primary vertex. This is shown in Figure 4.2.

The two track trigger attempts to identify a set of two displaced tracks in the event based on the transverse momentum p_T, impact parameter d_0, opening angle between the two tracks in the transverse plane $\Delta\phi$, and transverse decay length L_{xy} of the two track vertex. The set of two trigger tracks can be a combination of a generic track in the event and a decay product of the B hadron, or both trigger tracks could be decay products of the B hadron. The Two Track Trigger is composed of many trigger paths that are categorized into three scenarios, which again depend on the instantaneous luminosity of the Tevatron accelerator.

Chapter 5

Λ_b^{*0} Measurement

5.1 Introduction

The Standard Model predicts the existence of the Λ_b^0 baryon, a singlet with quark content $b[ud]$ and ground state $J^P = \frac{1}{2}^+$; and two states, Σ_b and Σ_b^*, which are isospin triplets with quark content $b\{q_1 q_2\}$ and ground states with $J^P = \frac{1}{2}^+$ and $J^P = \frac{3}{2}^+$ respectively. The theory predicts the orbital excitations Λ_b^{*0}, and of them, the two lowest mass ones are the Λ_b^{*0} with $J^P = \frac{1}{2}^-$ and $J^P = \frac{3}{2}^-$. These states can decay to the lowest singlet Λ_b^0 via strong processes involving emission of two pions provided sufficient phase space is available for a given mode (see Fig. 5.1). The Λ_b^{*0} are resonance states. The partner states of the Λ_b^{*0} in the charm sector are [22] the $J^P = \frac{1}{2}^-$ state $\Lambda_c(2595)^+$ and the $J^P = \frac{3}{2}^-$ state $\Lambda_c(2625)^+$. The strange P-wave analogs of the Λ_b^{*0} are [26] $\Lambda(1405)$, $J^P = \frac{1}{2}^-$ and the $\Lambda(1520)$, $J^P = \frac{3}{2}^-$.

A recent review and extensive critique of approaches to baryon spectroscopy can be found in [27]. Another review of theoretical methods and comparison of their predictions with experimental data can be found in [28]. The global approach to the baryon spectrum have been described in [29].

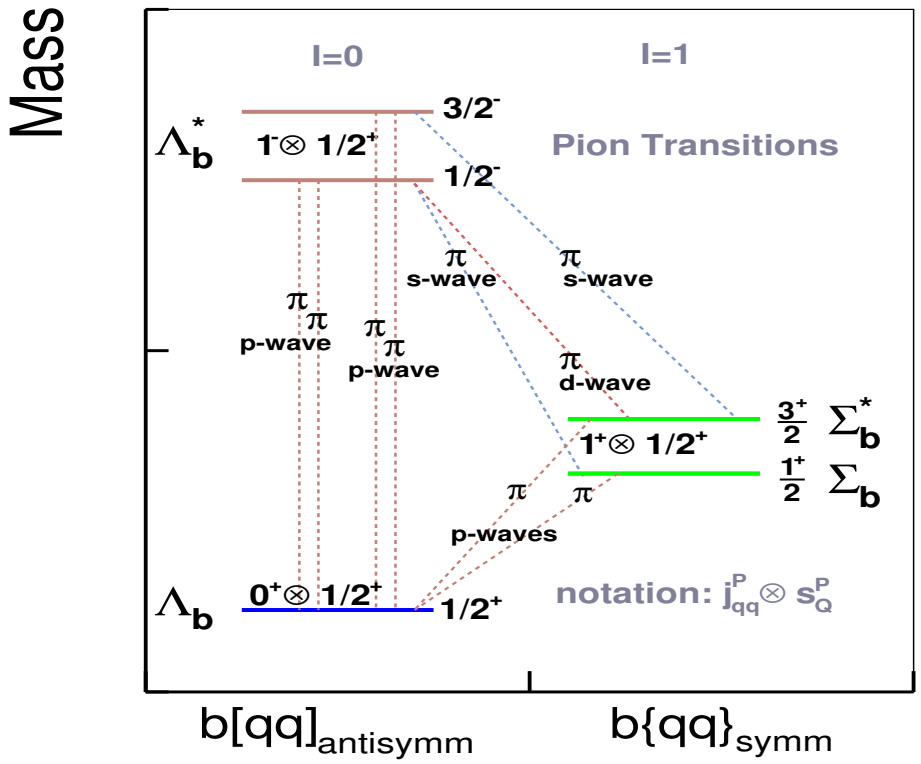

Figure 5.1: The pion transitions of low $S-$wave $\Sigma_b^{(*)}$ states and first orbital $P-$wave excitations Λ_b^{*0}. The $S-$wave transitions $\Lambda_b^{*0} \to \Sigma_b^{(*)}\pi$ may not be observable for low mass Λ_b^{*0} states.

Short comments on publications with particular emphasis on heavy baryon excited states are listed below. The corresponding theoretical predictions on masses are listed in Table 5.1.

- The paper [30] by Capstick and Isgur studies the three-quark system in a relativized quark potential model using a QCD approach.
- One of the first phenomenological analyses to establish the mass relations between various sectors of baryons is in [31]. This approach is being developed

further by Karliner *et al.* [32, 33, 34]. Here the heavy quark $\frac{1}{2}^-$ and $\frac{3}{2}^-$ excitations Λ_Q^* are interpreted as a P-wave isospin-0 spinless diquark coupled to the heavy quark. Under this assumption, the difference between the spin-averaged mass $M(\Lambda_Q^*)$ and the ground state mass $M(\Lambda_Q)$ is only the orbital excitation energy of the diquark.

- Roberts *et al.* [35] apply a non-relativistic quark model to the spectrum of baryons containing heavy quarks.

- Garcilazo *et al.* in [36] employ a constituent quark model in the non-relativistic case and solve exactly the three-quark problem using the Faddeev method in momentum space. They predict the orbital excitations $J = \frac{1}{2}, \frac{3}{2}$ for baryons.

- Ebert *et al.* [37, 38, 39] are developing a relativized quark model that treats a heavy baryon as a system of a heavy-quark coupled with a light diquark.

- Zhang *et al.* [40] [41] apply a QCD sum rule analytical non-perturbative approach to heavy baryon masses.

- Jenkins [42] successfully predicts bottom baryon masses in a model-independent approach based on a combined expansion in $1/N_c$ and $1/m_Q$ with $SU(3)$ flavor symmetry breaking. Unfortunately the predictions for bottom baryon excitations have not been made; see the further development of this case in the next bullet.

- Chow *et al.* [43] explore heavy baryons by taking into accounts both mass of the heavy quark and color number limit similarly to [42]. For the approximation of large heavy quark mass m_Q and large number of colors N_c, the effective field theory is developed in combined expansions of $1/N_c$ and $1/m_Q$. The model is applied to the charm Λ_c^+ and bottom Λ_b^0 baryons and their excitations. The model predicts the mass for the spin averaged orbitally excited Λ_b^0 state as

$M(\overline{\Lambda_b^{*0}}) \approx M(\Lambda_b^0) + 300\,\text{MeV} \approx 5920\,\text{MeV}$, where the mass value is the one averaged over the spin $J = \frac{1}{2}$ and $\frac{3}{2}$ states.

Reference	$M(\Lambda_b^0)$, MeV/c^2	$M(\Lambda_b^{*0}, \frac{1}{2}^-)$, MeV/$c^2$	Q, MeV/c^2	$M(\Lambda_b^{*0}, \frac{3}{2}^-)$, MeV/$c^2$	Q, MeV/c^2
Capstick [30]	5585	5912	47	5920	55
Karliner [32, 34]	5619.7,CDF	5929 ± 2	29	5940 ± 2	40
Roberts [35]	5612	5939	47	5941	49
Garcilazo [36]	5625	5890	-15	5890	-15
Faustov [37, 38]	5622	5930	28	5947	45
Zhang [40, 41]	5690 ± 130	5850	-120	5900	-70
Chow [43]	5619.7,CDF	5920	20	5920	20

Table 5.1: Theoretical predictions for Λ_b^{*0} Masses. The Q-value is defined as $Q = M(\Lambda_b^{*0}) - M(\Lambda_b^0) - 2 \cdot m(\pi^\pm)$ for the hadronic decay mode of interest, $\Lambda_b^{*0} \to \Lambda_b^0 \pi^+ \pi^-$. The predictions by Chow *et al.* are made for the spin averaged state.

After this work had been begun (as of 15 May 2012), the LHCb Collaboration has published [44] an observation of excited Λ_b^{*0} baryons. The LHCb results are summarized in Table 5.1 below.

The predictions in Table 5.1 made by Capstick [30] and Roberts [35] are very differ-

$M(\Lambda_b^{*0}(5912))$, MeV/c^2	Q, MeV/c^2	$M(\Lambda_b^{*0}(5920))$, MeV/c^2	Q, MeV/c^2
$5911.97 \pm 0.12 \pm 0.66$	13.46 ± 0.12	$5919.77 \pm 0.08 \pm 0.66$	21.26 ± 0.08

Table 5.2: LHCb results on the Λ_b^{*0} observation. The Q values of the observed resonance states are shown as well [44] .

ent from the LHCb observation and can be considered as outliers. The predictions made by Chow [43] are in decent agreement with the LHCb results.

5.2 Possible Scenarios

The predicted masses (Table 5.1) for the first state $\Lambda_b^{*0}(\frac{1}{2}^-)$ lie very close to the hadronic three-body mode threshold with $Q \sim (20...47)\,\mathrm{MeV}/c^2$. The predictions for its higher partner $\Lambda_b^{*0}(\frac{3}{2}^-)$ are only $(2...17)\,\mathrm{MeV}/c^2$ higher. Some authors [36, 41, 40] predict masses below the hadronic three-body decay threshold.

Unlike the partners from the charm quark sector decaying via two-body channels ($\Lambda_c^{*+} \to \Sigma_c^{(*)}\pi$), the modes in the bottom sector, $\Lambda_b^{*0} \to \Sigma_b^{(*)\pm}\pi^{\mp}$, are expected to be heavily suppressed if not closed by the very narrow phase space available. We are left with a search in the three-body domain $\Lambda_b^{*0} \to \Lambda_b^0\pi^+\pi^-$ of phase space where theoretical calculations for the width $\Gamma(\Lambda_b^{*0})$ are difficult to make and do not exist to our knowledge.

If Λ_b^{*0} lies above the three-body threshold, the states (or a single state) will be produced near the threshold and still in an energy suppressed condition. Chow *et al.* [43] predict that the Λ_b^{*0} states should exhibit radiative decay modes with quite a substantial branching ratio. A plausible scenario has the lowest state, $\Lambda_b^{*0}(\frac{1}{2}^-)$ below the hadronic mode threshold and decaying radiatively to $\Lambda_b^0\gamma$ with $\mathcal{B} = 100\%$, unrecorded by the CDF detector. In another pessimistic scenario, the state has some tiny $\Lambda_b^0\pi^+\pi^-$ $\mathcal{B}$ fraction which will have a very low acceptance and a low tracking efficiency for the pair of slow pions. The latter considerations can again make the state unobservable despite having its mass exceed the hadronic mode threshold.

According to some predictions, the state $\Lambda_b^{*0}(\frac{3}{2}^-)$ may lie only $\sim 10\,\mathrm{MeV}/c^2$ above its $\frac{1}{2}^-$ partner and it might also have a sizable radiative $\mathcal{B}(\Lambda_b^{*0}(\frac{3}{2}^-) \to \Lambda_b^0\gamma)$ fraction. The search should be focused on Q value in the range $(0,\, 45)\,\mathrm{MeV}/c^2$ of the spectrum.

5.3 Data Sample and Trigger

This work is based on data corresponding to the full integrated luminosity of $\int \mathcal{L}\, dt \approx 9.6\,\text{fb}^{-1}$ and comprising the B group Standard Ntuple (*BStNtuple*) datasets (of periods #0 through #38) collected with the CDF Two Track Trigger. The data handling system based on Sequential Access Model (SAM) datasets has been used, see Table 5.3. The experimental data have been filtered through the Good Run List, GRL, version 45, corresponding to the GRL file, goodrun_b_bs_nocal_nomu.v45.list . Correcting the total luminosity of $\sim 9.47\,\text{fb}^{-1}$ (last line in Table 5.3) by a factor of 1.019 (selects only the good runs), one finds the total luminosity to be $\int \mathcal{L}\, dt \approx 9.6\,\text{fb}^{-1}$.

SAM dataset name	Period #	Run Range	$\int \mathcal{L}\, dt$, nb^{-1}
`xbhdid`	0	138809 – 186598	344315.0
`xbhdih`	1 – 4	191289 – 203799	397962.0
`xbhdii`	5 – 10	203819 – 233111	895072.0
`xbhdij`	11 – 13	233133 – 246229	703291.0
`xbhdik`	14 – 17	253134 – 261005	498734.0
`xbhdfm`	18 – 28	261119 – 289197	3259733.0
`xbhdfp`	29 – 38	289273 – 312510	3375211.0
total stat.	0 – 38	138809 – 289197	9474318.0

Table 5.3: The datasets used in this analysis with the runs filtered according to `GRL, version 45`. Correcting the total luminosity of $\sim 9.47\,\text{fb}^{-1}$ by a factor of 1.019 one yields a total luminosity to be of $\int \mathcal{L}\, dt \approx 9.6\,\text{fb}^{-1}$.

The *BStNtuple* data listed in Table 5.3 are based on the data collected by CDF Two Track Triggers of several configurations: `B_CHARM_LOWPT`, `B_CHARM_SCENA` and `B_CHARM_HIGHPT`, see the detailed description in [45]. The scenario `B_CHARM_LOWPT` is inclusive with respect to the other two. The `B_CHARM_LOWPT` conditions are tested at the offline production step by the dedicated modules called from the offline production executable `CandsExe`. The details on trigger conditions are listed in Table 5.4.

Parameter	Trigger Condition
`B_CHARM_LOWPT` scenario	
2 tracks: trk_1, trk_2	reconstructed by XFT/SVT/L3
$\lvert d_0\rvert(trk_1)$, $\lvert d_0\rvert(trk_2)$	$> 120\,\mu$m
$\lvert d_0\rvert(trk_1)$, $\lvert d_0\rvert(trk_2)$	$< 1000\,\mu$m
opening angle $\lvert\phi_1 - \phi_2\rvert$	$\in (2^\circ, 90^\circ)$
$\chi^2_{SVT}(trk_1)$, $\chi^2_{SVT}(trk_2)$	< 25
$L_{xy}(trk_1, trk_2)$	$> 200\,\mu$m
$p_{\mathrm{T}}(trk_1)$, $p_{\mathrm{T}}(trk_2)$	$> 2.0\,\mathrm{GeV}/c$
$p_{\mathrm{T}}(trk_1) + p_{\mathrm{T}}(trk_2)$ (scalar sum)	$> 4.0\,\mathrm{GeV}/c$
`B_CHARM_SCENA` scenario	
2 tracks: trk_1, trk_2	reconstructed by XFT/SVT/L3
$Q(trk_1) \cdot Q(trk_2)$	$= -1$, opposite charges
$\lvert d_0\rvert(trk_1)$, $\lvert d_0\rvert(trk_2)$	$> 120\,\mu$m
$\lvert d_0\rvert(trk_1)$, $\lvert d_0\rvert(trk_2)$	$< 1000\,\mu$m
opening angle $\lvert\phi_1 - \phi_2\rvert$	$\in (2^\circ, 90^\circ)$
$\chi^2_{SVT}(trk_1)$, $\chi^2_{SVT}(trk_2)$	< 25
$L_{xy}(trk_1, trk_2)$	$> 200\,\mu$m
$p_{\mathrm{T}}(trk_1)$, $p_{\mathrm{T}}(trk_2)$	$> 2.0\,\mathrm{GeV}/c$
$p_{\mathrm{T}}(trk_1) + p_{\mathrm{T}}(trk_2)$ (scalar sum)	$> 5.5\,\mathrm{GeV}/c$
`B_CHARM_HIGHPT` scenario	
2 tracks: trk_1, trk_2	reconstructed by XFT/SVT/L3
$Q(trk_1) \cdot Q(trk_2)$	$= -1$, opposite charges
$\lvert d_0\rvert(trk_1)$, $\lvert d_0\rvert(trk_2)$	$> 120\,\mu$m
$\lvert d_0\rvert(trk_1)$, $\lvert d_0\rvert(trk_2)$	$< 1000\,\mu$m
opening angle $\lvert\phi_1 - \phi_2\rvert$	$\in (2^\circ, 90^\circ)$
$\chi^2_{SVT}(trk_1)$, $\chi^2_{SVT}(trk_2)$	< 25
$L_{xy}(trk_1, trk_2)$	$> 200\,\mu$m
$p_{\mathrm{T}}(trk_1)$, $p_{\mathrm{T}}(trk_2)$	$> 2.5\,\mathrm{GeV}/c$
$p_{\mathrm{T}}(trk_1) + p_{\mathrm{T}}(trk_2)$ (scalar sum)	$> 6.5\,\mathrm{GeV}/c$

Table 5.4: The CDF Two Track Trigger scenarios.

5.4 *BStNtuple* Data and Conditions

The present analysis is based on a general purpose ROOT ntuple *BStNtuple* generated by a package `BottomMods` of the tags or releases v80, v81, and v82 bundled

with a suite of several other packages of the same tag. The tag v80 has been used only for period 0. All other periods have been produced with continuously improving tags v81 and then v82 (for the last large datasets xbhdfm and xbhdfp). The production executable `CandsExe` and corresponding shared libraries used in the present analysis of the *BStNtuple* datasets have been built against general version `cdfsoft2, v. 6.1.4m` with tag `v82`. These *BStNtuple* data have been used by many CDF analyses including those related to B_s^0-mixing [46].

Analysis branches of the *BStNtuple* correspond to the following decay modes that are relevant to this analysis[2]:

- `LbS-Lb2Pi-LcPi-PKPi` collection of $\Lambda_b^{*0} \to \Lambda_b^0 \pi^+_{soft} \pi^-_{soft}$ candidates. All candidates in this collection are subjected to the vertex fit.

- `Lb-LcPi-PKPi` collection of $\Lambda_b^0 \to \Lambda_c^+ \pi_b^-$ candidates. All Λ_b^0 candidates are subjected to the vertex fit. The contributing $\Lambda_c^+ \to pK^-\pi^+$ candidates are vertex fitted with the mass constrained to the $M_{PDG}(\Lambda_c^+)$ value [22].

- `Lc-PKPi` collection of $\Lambda_c^+ \to pK^-\pi^+$ candidates. Only the candidates contributing to the parent collections listed above are saved. The three tracks contributing to the candidates are fitted to a common secondary vertex.

- The full unbiased collection of pions `Pions` is saved in every *BStNtuple* event. `Pions` are constructed from the `stdTracks` collection with additional energy corrections and refits. The pion's energy loss in the detector adds to smearing of energy which require additional refitting of tracks by scaling covariance matrix. The `stdTracks` collection is a CDF default `defTracks` track collection with minimal quality requirements, see below.

[2]Unless otherwise stated, all references to a specific charge combination imply the charge conjugate combination as well.

Track/Collection	Criteria
`stdTracks`	made from `defTracks` with valid helix fit and physical error matrix, no COT or/and SVX hit cuts applied
$\pi^{\pm}$/`Pions` full and unbiased	from `stdTracks` corrected for energy loss magnetic field scaled, COT covariance matrix scaled L00 hits added, track refits. No plain p_{T} cuts.
p/`Protons` contributing to candidates only	from `stdTracks` corrected for energy loss magnetic field scaled, COT covariance matrix scaled L00 hits added, track refits. No plain p_{T} cuts.
K/`Kaons` contributing to candidates only	from `stdTracks` corrected for energy loss magnetic field scaled, COT covariance matrix scaled L00 hits added, track refits. No plain p_{T} cuts.

Table 5.5: The track selection criteria.

- The collections of protons, `Protons`, and kaons, `Kaons`. Only the candidates contributing to the parent (decay mode) collections listed above are saved.

The track selection criteria are summarized in Table 5.5.

The selection criteria for composite candidates are complex. The details on selections are listed in Table 5.6.

- $\Lambda_c^+ \to pK^-\pi^+$ candidates collection is built by the `D_SSS` module.
- $\Lambda_b^0 \to \Lambda_c^+\pi_b^-$ candidate produces the second weak decay vertex. The collection is built by the `D_DS` module.
- $\Lambda_b^{*0} \to \Lambda_b^0\pi_{soft}^{\pm}\pi_{soft}^{\mp}$ is a strong decay process. Its vertex is a primary vertex of the event. The candidates are processed by the `D_DD` module where the vertex fit is activated but with the very loose $\chi^2_{r\phi} < 100$ requirement to keep the efficiency as high as possible. No mass constraints are applied here because the mass difference Q-spectra will be analyzed.

The inclusive `B_CHARM_LOWPT` trigger scenario [45] is imposed on every event; the event is rejected if `B_CHARM_LOWPT` is not confirmed. The details on trigger conditions are listed in Table 5.4. The module `TrigTracks-LowPt` reconstructs and replicates the trigger condition at the offline level with the offline default `defTracks` tracks. The events are filtered by the `TrigTracks-LowPt` module during *BStNtuple* production. The module creates the collection of pairs of tracks matched with the ones satisfying the `B_CHARM_LOWPT` trigger conditions and stored in the `SVTD` object. The subsequent modules reconstructing candidates enforce the match between some of candidate's tracks and the ones from the trigger track pair collection. As Table 5.6 shows, the $\Lambda_b^0 \to \Lambda_c^+ \pi_b^-$ candidates from the `Lb-LcPi-PKPi` collection must satisfy the trigger, i.e., at least 2 out of the 4 tracks must match the trigger track pair collection.

Candidate/Collection	Criteria
$\Lambda_c^+ \to pK^-\pi^+$/`Lc-PKPi`	made from basic `Pions`,`Kaons`,`Protons`
charge Q	$= \pm 1$
vertex fit with $\chi^2_{r\phi}$	< 20.0
$\Delta(z_0)$	$< 1.5\,\mathrm{cm}$
$p_\mathrm{T}(\pi), p_\mathrm{T}(K), p_\mathrm{T}(p)$	$> 0.350\,\mathrm{GeV}/c^2$
$M(pK^-\pi^+)$	$\in (2.200,\ 2.380)\,\mathrm{GeV}/c^2$
trigger confirmation	the `B_CHARM_LOWPT` imposed per event,
	≥ 1 trigger track $\in (\mathrm{p}, \mathrm{K}, \pi)$
$\Lambda_b^0 \to \Lambda_c^+\pi_b^\pm$/`Lb-LcPi-PKPi`	made from composite `Lc-PKPi` and basic `Pions`
charge Q	$= 0,\ \pm 2$
vertex fit with $\chi^2_{r\phi}$	< 40.0
and $M(\Lambda_c^+ \to pK^-\pi^+)$	$\in (2.260,\ 2.311)\,\mathrm{GeV}/c^2$ or
	$\approx (2.28646 \pm 4 \cdot \sigma)\,\mathrm{GeV}/c^2$
mass constraint: $M(pK^-\pi^+)$	"true", i.e. set $= 2.28646\,\mathrm{GeV}/c^2$ (PDG)
vertex information	linked to branches with Primary
	and secondary VX info per event
$p_\mathrm{T}(\pi), p_\mathrm{T}(K), p_\mathrm{T}(p)$	$> 0.350\,\mathrm{GeV}/c^2$
$p_\mathrm{T}(\pi_b^\pm)$	no cut set, threshold is propagated via trigger
$M(\Lambda_c^+\pi_b^\pm)$	$\in (4.500,\ 7.000)\,\mathrm{GeV}/c^2$
trigger confirmation	the `B_CHARM_LOWPT` imposed per event,
	≥ 2 trigger track $\in (\mathrm{p}, \mathrm{K}, \pi^+, \pi^-_\mathrm{b})$, i.e.
	Λ_b^0 candidate does trigger the `B_CHARM_LOWPT`
$\Lambda_b^{*0} \to \Lambda_b^0\pi^\pm_{soft}\pi^\mp_{soft}$/	made from
`LbS-Lb2Pi-LcPi-PKPi`	composite `Lb-LcPi-PKPi` and `2Pi`
charge Q	$= 0$
vertex fit with $\chi^2_{r\phi}$	< 100.0
and $M(\Lambda_b^0 \to \Lambda_c^+\pi_b^\pm)$	$\in (5.200,\ 6.500)\,\mathrm{GeV}/c^2$ or
	$\approx (5.619^{+46\cdot\sigma}_{-22\cdot\sigma})\,\mathrm{GeV}/c^2$
mass constraint	"false", i.e. not set
vertex information	linked to branches with Primary
	and secondary VX info per event
$p_\mathrm{T}(\pi), p_\mathrm{T}(K), p_\mathrm{T}(p)$	$> 0.350\,\mathrm{GeV}/c^2$
$p_\mathrm{T}(\pi_b^\pm)$	$> 0.350\,\mathrm{GeV}/c^2$
$p_\mathrm{T}(\pi^\pm_{soft})$	$> 0.200\,\mathrm{GeV}/c^2$, set in `2Pi`
$M(\Lambda_b^0\pi^\pm_{soft}\pi^\mp_{soft})$	$\in (5.400,\ 7.500)\,\mathrm{GeV}/c^2$

Table 5.6: The collections of candidates to be used in the analysis and their selection criteria set in *BStNtuple* branches.

5.5 Monte Carlo Simulation Data

The mass resolution on the Λ_b^{*0} resonances is predicted with a Monte Carlo simulation that generates $\underline{q}$uarks according to a next-to-leading order calculation [47] and produces events containing final state hadrons by simulating $\underline{q}$uark fragmentation [48]. A mass value of $5920\,\mathrm{MeV}/c^2$ for the Λ_b^{*0} is used in the Monte Carlo generator, and the natural width of the generated state is set to zero. Final state decay processes are simulated with the EVTGEN [49] program, and all simulated $\underline{h}$adrons are produced without polarization. The generated events are input to the detector and trigger simulation based on GEANT3 [50] and processed through the same reconstruction and analysis algorithms as are used on the data.

5.6 Mass Difference Spectrum for Λ_b^{*0} Candidates

The Λ_b^{*0} candidates are sought in the decay chain $\Lambda_b^{*0} \to \Lambda_b^0 \pi_s^+ \pi_s^-$ with $\Lambda_b^0 \to \Lambda_c^+ \pi_b^-$ and its daughter $\Lambda_c^+ \to pK^-\pi^+$.

To remove the contribution due to the mass resolution of each Λ_b^0 candidate and to avoid absolute mass scale systematic uncertainties, the Λ_b^{*0} candidates are reconstructed in the mass difference Q-value spectrum defined as

$$Q = M(\Lambda_b^0 \pi_s^+ \pi_s^-) - m(\Lambda_b^0) - 2 \cdot m(\pi^\pm).$$

The Λ_b^0 candidates are reconstructed in their (only possible) weak decay mode. Hence the width of the Λ_b^0 signal is determined by the detector mass resolution at the Q-value scale. The width of the possible Λ_b^{*0} resonance signal is determined by its natural value convoluted with the mass resolution of the soft pion pair $\pi_s^+\pi_s^-$ at the Q-value scale. Narrow signatures are searched at the low range (where the signals are predicted) of the Q-spectrum constructed for Λ_b^{*0} candidates.

5.7 Track Quality Requirements

At the analysis stage the track quality criteria for the Λ_b^0 tracks are tightened with respect to Table 5.5. The analysis track quality cuts are shown in Table 5.7. The

Track Parameter	Analysis Cut
Track Collections	`Protons`, `Kaons`, `Pions`
COT stereo hits	≥ 10
COT axial hits	≥ 10
SVX $r-\phi$ hits	≥ 3
$\lvert d_0 \rvert$	$< 0.1\,\text{cm}$
p_{T}	$> 400\,\text{MeV}/c$

Table 5.7: Λ_b^0 Candidates: Track Quality Cuts

tracks involved in Λ_c^+ and Λ_b^0 reconstruction have the momenta above $400\,\text{MeV}/c$ where the CDF tracking efficiency flattens. The quality cuts shown in Table 5.7 are the standard ones used by other CDF analyses.

The basic track quality criteria for the soft pion tracks are somewhat loose with respect to nominal tracks contributing to the Λ_b^0 candidate. In this situation we are limited by our goals, specifically in a search for a new resonance state Λ_b^{*0} in its hadron mode with two soft pions emitted.

First of all we take the soft tracks with momentum as low as $200\,\text{MeV}/c$. We consider also the option to include the soft tracks with hits found in the SVX II silicon tracker only ("Si standalone" tracks) when no hits in the COT tracker are found. The other option includes the soft tracks that have hits in both SVX II and the COT but excludes the "Si standalone" tracks. Hit distributions for both soft pions based on the CDF MC simulation data of $\Lambda_b^{*0} \to \Lambda_b^0 \pi_s^+ \pi_s^-$ generated with BGEN are shown in Figure 5.2. One can see that the requirement on the total number of stereo and axial hits in the COT is fully efficient above nine. The MC hit

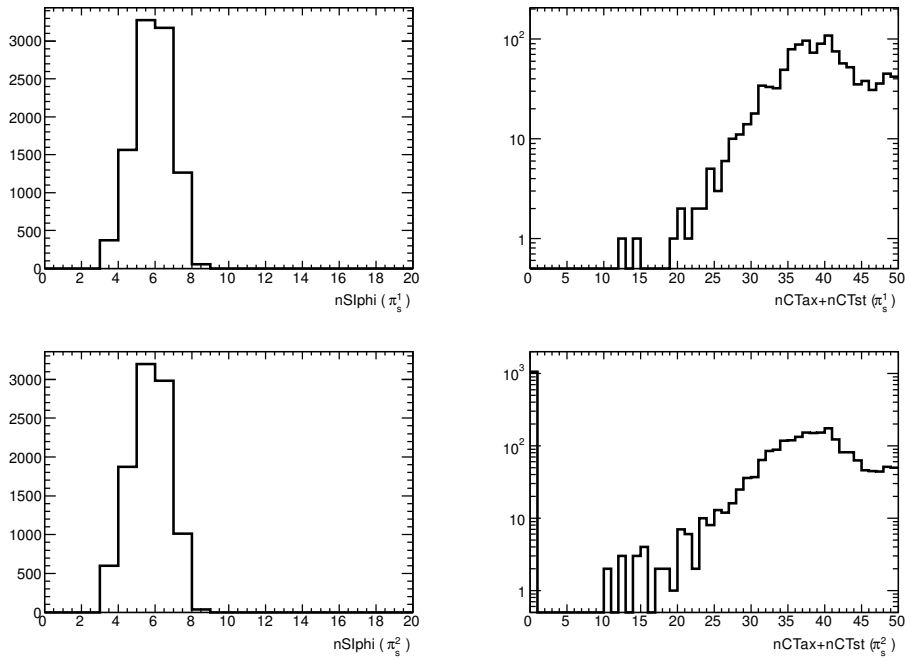

Figure 5.2: Hit distribution in SVX II and COT for soft pions 1 and 2: full CDF MC simulation of Λ_b^{*0} generated with BGEN. The number of $r-\phi$ hits, $N_{r-\phi}$(SVX II) produced by soft pions in SVX II is demonstrated in the left column. The sum of the COT stereo and axial hits, $(N_{\rm ax}+N_{\rm st})$(COT), is demonstrated in the right column.

distributions are compared with the data in Figure 5.3 and Figure 5.4. The COT hits distributions for soft pions taken from the calibration D^* experimental sample, Fig. 5.4, as well as for soft pions belonging to the Λ_b^{*0} candidates, Fig. 5.3, are in agreement with the MC predictions. The selection criteria applied to the soft pion track are listed in Table 5.8. Further discussion on the final choice to include the "Si standalone" tracks continues in the chapters below.

5.8 Λ_b^0 Analysis Cuts

The background in Q-value distribution is composed from

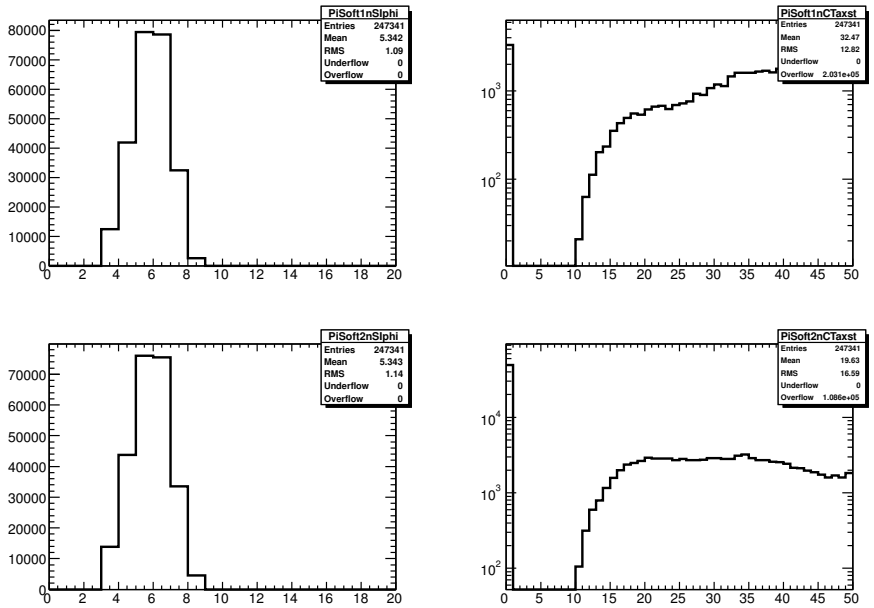

Figure 5.3: Hit distribution in SVX II and COT for soft pions 1 (upper row) and 2 (lower row) for Λ_b^{*0} candidates in the experimental data sample. The number of $r-\phi$ hits, $N_{r-\phi}$(SVX II) produced by soft pions in SVX II is demonstrated by the plots in the left column. The sum of the COT stereo and axial hits, $(N_{\rm ax}+N_{\rm st})$(COT), is demonstrated by the plots in the right column.

- the background under the Λ_b^0 signal candidates in the $M(\Lambda_c^+\pi^-)$ spectrum combined with pairs of pions $\pi^+\pi^-$ with their momenta extending to $p_{\rm T} \sim 200\,{\rm MeV}/c$.

- the Λ_b^0 signal candidates combined with a $\pi^+\pi^-$ originating from hadronization processes like b-quark fragmentation into various bottom baryon states.

The background shape of Q-spectrum is expected to have a steep rising shape. However there are few factors that may improve the chances for observation of a signal:

- For Λ_b^{*0} case the Λ_b^0 candidates are present in combination with two charged pion tracks, so the S/B ratio for Λ_b^0 peak might be higher than for the inclusive

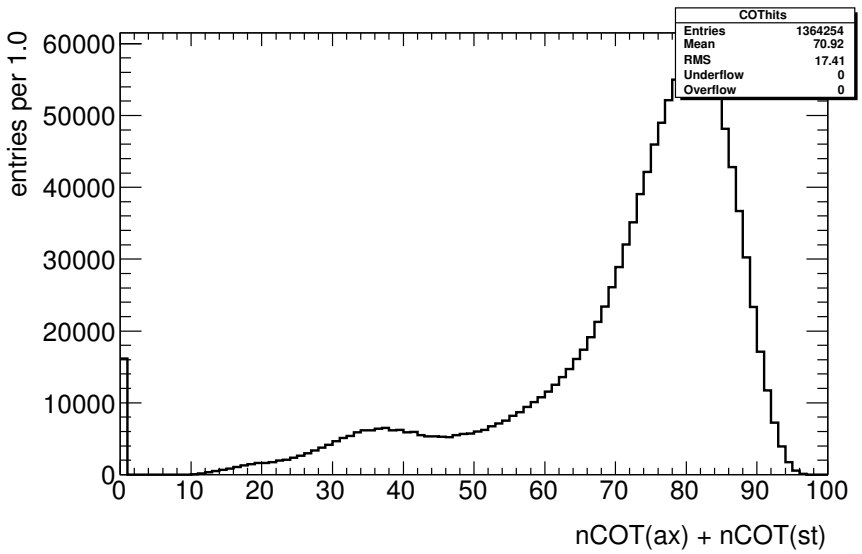

Figure 5.4: Hit distribution in COT for soft pions for D^* candidates in the experimental data sample. The sum of the COT stereo and axial hits, $(N_{\rm ax} + N_{\rm st})$(COT), are shown in the plot.

Λ_b^0 signal.

Track Parameter	Analysis Cut
Track Collections	`Pions`
Hit Selection:	
COT stereo hits, $N_{\rm st}$(COT)	< 1, no hits found
COT axial hits, $N_{\rm ax}$(COT)	< 1, no hits found
SVX $r-\phi$ hits, $N_{r-\phi}$(SVX II)	≥ 4
OR	
$(N_{\rm ax} + N_{\rm st})$(COT)	≥ 10
SVX $r-\phi$ hits	≥ 3
$\lvert d_0 \rvert$	$< 0.1\,{\rm cm}$
$p_{\rm T}$	$> 200\,{\rm MeV}/c$

Table 5.8: Λ_b^{*0} Candidates: $\pi^{\pm}_{soft}$ Track Quality Cuts

- The resolution of a possible signal in the Q spectrum is $\sim$1.0...2.0 MeV/c^2, to be compared with the resolution $\sigma(\Lambda_b^0) \sim 18\,\mathrm{MeV}/c^2$ of a $M(\Lambda_b^0 \to \Lambda_c^+\pi_b^-)$ signal.
- At the threshold area of the mass difference Q-spectrum, the background is expected to be low due to kinematical reasons.

The following are definitions of useful quantities used to identify and extract the Λ_b^0 signal [51].

- $ct(\Lambda_b^0)/\sigma_{ct}$, the Λ_b^0 proper lifetime expressed in terms of its error. The Λ_b^0 proper lifetime is defined as

  $$ct(\Lambda_b^0) = L_{xy} \cdot \frac{M(\Lambda_b^0)}{p_{\mathrm{T}}(\Lambda_b^0)}\,,$$

  where L_{xy} is defined in the transverse plane as

  $$L_{xy}(\Lambda_b^0) = \vec{D}_{xy} \cdot (\vec{p}_{xy}/p_{\mathrm{T}}).$$

- $|d_0(\Lambda_b^0)|$, the impact parameter of the Λ_b^0 candidate defined in the transverse plane as

  $$|d_0(\Lambda_b^0)| = \left|\vec{D}_{xy} \times (\vec{p}_{xy}/p_{\mathrm{T}})\right|.$$

- $ct(\Lambda_c^+ \leftarrow \Lambda_b^0)$, the charm baryon Λ_c^+ proper lifetime relative to its origin in the Λ_b^0 decay reconstructed vertex.
- $\vec{D}_{xy}$ is the position of the Λ_b^0 decay vertex with respect to the primary vertex in the transverse plane.
- $p_{\mathrm{T}}(\pi_b^-)$, the transverse momentum of a prompt pion from a $\Lambda_b^0 \to \Lambda_c^+\pi_b^-$ decay.

As this analysis is preceded by the published one on CDF $\Sigma_b^{*\pm}$ mass measurements, we know approximately the set of cuts in the vicinity of an optimal point, see [51].

#	Variable	Cut value
1	$p_{\mathrm{T}}(p)$	$> 2.0\,\mathrm{GeV}/c$
	trigger confirmation	`B_CHARM_LOWPT`
2	$p_{\mathrm{T}}(K^-)$	$> 0.4\,\mathrm{GeV}/c$
3	$p_{\mathrm{T}}(\pi^+)$	$> 0.4\,\mathrm{GeV}/c$
4	$\left\lvert m(\mathrm{pK}^-\pi^+) - \mathrm{m}(\Lambda_\mathrm{c}^+)_{\mathrm{PDG}}\right\rvert$	$< 18\,\mathrm{MeV}/c^2$, $\pm 3\sigma$
5	proton ID	no particle ID used
6	$p_{\mathrm{T}}(\pi_b^-)$	$> 0.4\,\mathrm{GeV}/c$
7	$\mathrm{Prob}(\chi^2_{3D})$ of Λ_b^0 vertex fit	$> 0.01\%$
8	$ct(\Lambda_b^0)$	$> 200\,\mu\mathrm{m}$
9	$ct(\Lambda_b^0)/\sigma_{ct}$	> 6.0
10	$\lvert d_0(\Lambda_b^0)\rvert$	$< 80\,\mu\mathrm{m}$
11	$ct(\Lambda_c^+ \leftarrow \Lambda_b^0)$	$> -100\,\mu\mathrm{m}$
12	$p_{\mathrm{T}}(\Lambda_b^0)$	$> 4.0\,\mathrm{GeV}/c$

Table 5.9: The initial values of the analysis cuts for the Λ_b^0 reconstruction.

Cut #1 on a p from $\Lambda_c^+ \to pK^-\pi^+$ confirms the condition imposed at the Two-Track Trigger level. We assume that the second leg of the trigger is picked up among other Λ_c^+ tracks or is taken as the Λ_b^0 decay pion π_b^-. Cut #4 specifies the invariant mass range of the Λ_c^+ candidates contributing to the Λ_b^0. We do not use particle identification information in this analysis. The Λ_b^0 vertex is subjected to a three-dimensional kinematic fit with the Λ_c^+ candidate mass constrained to its world-average value [22]. The probability of the constrained Λ_b^0 vertex fit must exceed 0.01% as specified by Cut #7. Cut #8 requires the proper lifetime of the Λ_b^0 to be above $200\,\mu$m and confirms the Two-Track Trigger. The cuts on the total momentum of the Λ_b^0 candidate (#12) and its decay pion π_b^- are powerful for background rejection.

As has been shown in studies on Σ_b [52, 53, 54] the dominant ($\sim 90\%$) background at the low range of the Q value for the Σ_b is created by the combination of real Λ_b^0 with hadrons produced in the b-quark hadronization process. We expect the same physics scenario in the Λ_b^{*0} case. Particle identification is not expected to play a critical role in the suppression of background composed from real Λ_b^0 and random tracks originating

from the Λ_b^0 fragmentation processes. Kinematical measures like the vertex fit of the Λ_c^+ candidate with the π_b^- track, requirements on the proton to be in the trigger, i.e. with $p_{\mathrm{T}} > 2.0\,\mathrm{GeV}/c$, and cuts on the $p_{\mathrm{T}}(\pi_b^-) > 1.0, 1.5\,\mathrm{GeV}/c$, together with the topological cuts, provide the Λ_b^0 signals with S/B ratios of 1.0...2.0. Particle identification has not been used in any of the Λ_b^0 published analyses [54, 55, 56, 57].

5.8.1 Optimization of the Total Transverse Momentum $p_T(\Lambda_b^0)$ Selection Requirement

The total momentum spectra for the Λ_b^0 and Λ_b^{*0} states as reconstructed from MC data are shown in Fig. 5.5. To optimize the cut on total momentum of the Λ_b^0 candidates we use the score function (or Figure Of Merit, FOM [58]) defined in Eq. (5.1) below.

$$\mathrm{FOM} = \frac{S(\mathrm{MC})}{(1.0 + \sqrt{B(\text{exp. data})})}\ , \tag{5.1}$$

where $S(\mathrm{MC})$ is the number of signal events of Λ_b^{*0} evaluated from MC at the specific point of the cut on $p_{\mathrm{T}}(\Lambda_b^0)$, while the background is evaluated from the side band range of the experimental Q value spectrum. The side band shown at Fig. 5.6 is set at $Q \in (0.041, 0.083)\,\mathrm{MeV}/c^2$. The left edge of the side band is far enough from the expected signal position around $Q \sim 21\,\mathrm{MeV}/c^2$ as it was identified by the LHCb observation [44]. The Λ_b^{*0} signal is expected at the very edge of the spectrum, very near the threshold. The level of the background in the Q-value spectrum is low in this area. Including the background into the score function of while optimizing the Λ_b^0 signal makes it more sensitive to the background under the Λ_b^{*0} signal which is also expected to be of low statistics.

For the optimization scans, the same total transverse momentum cut is applied to the Λ_b^{*0} candidate. The $p_{\mathrm{T}}(\pi_b^-)$ is required to be above $1.0\,\mathrm{GeV}/c$, and the impact parameter of the soft pions, $|d_0(\pi_s^{\pm})/\sigma_{d_0}| < 3.0$.

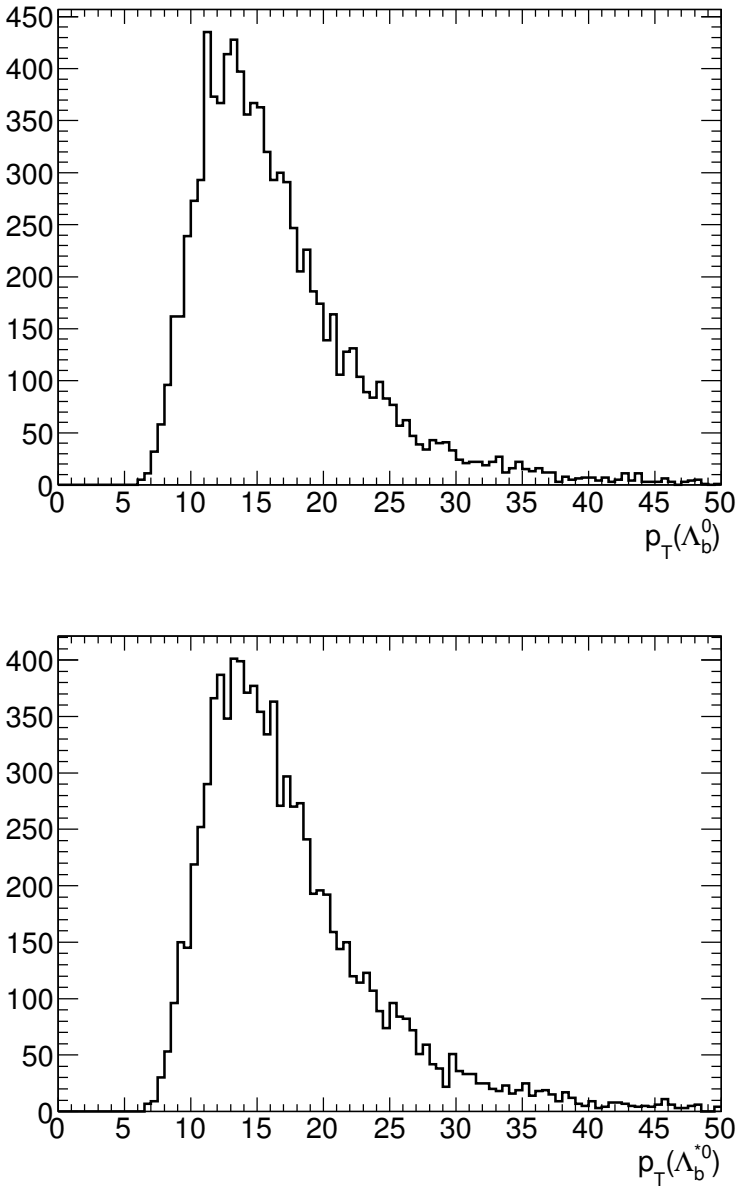

Figure 5.5: Total transverse momenta $p_{\mathrm{T}}(\Lambda_b^0)$ and $p_{\mathrm{T}}(\Lambda_b^{*0})$ from MC data.

The scan of total momentum is shown in Figure 5.7. To keep the efficiency of the signal high and given the fact that the score function flattens at 9.0 GeV/c, the

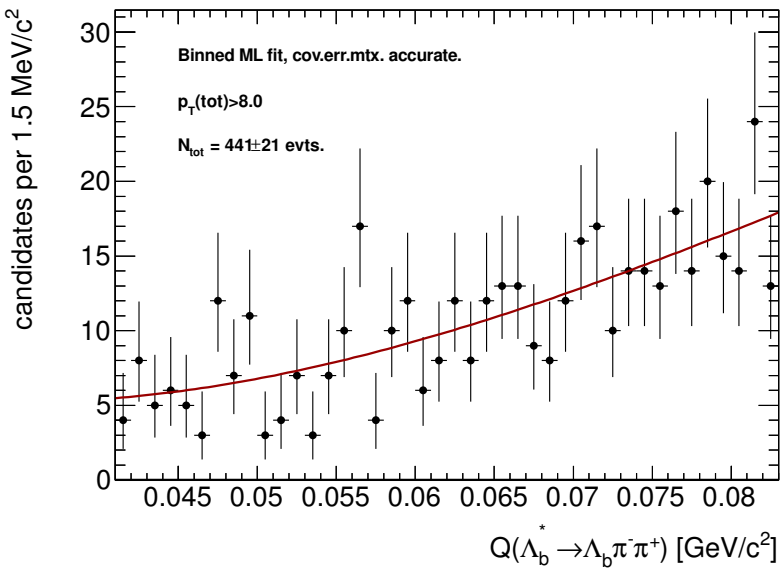

Figure 5.6: An example of a Q value side-band of extent $(0.041, 0.083)\,\mathrm{MeV}/c^2$, fitted with the second order Chebyshev polynomial to integrate the number of entries, $B(\mathrm{data})$. Here $p_\mathrm{T}(\Lambda_b^0) > 8.0\,\mathrm{GeV}/c$.

optimal cut is selected to be $p_\mathrm{T}(\Lambda_b^0) > 9.0\,\mathrm{GeV}/c$.

5.8.2 Optimization of the Decay Pion Transverse Momentum $p_T(\pi_b^-)$ Selection Requirement

Again we use the score function of Eq. (5.1). In this case the numerator is measured from the experimental Λ_b^0 signal: the $S(\Lambda_b^0)$ is found from the fit of the Λ_b^0 signal reconstructed in the invariant mass distribution $m(\Lambda_c^+\pi^-)$. The denominator is again determined using the experimental Q value side-band of $(0.041, 0.083)\,\mathrm{MeV}/c^2$. The cut on the total momentum is fixed to the value found in Section 5.8.1, specifically $p_\mathrm{T}(\Lambda_b^0) > 9.0\,\mathrm{GeV}/c$. The impact parameters of soft pions are required to have $|d_0(\pi_s^\pm)/\sigma_{d_0}| < 3.0$.

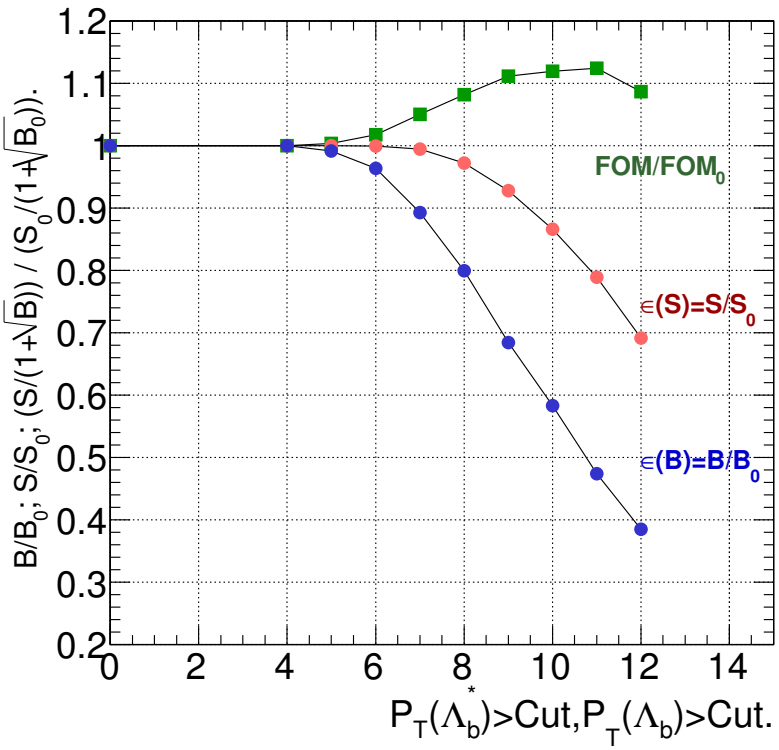

Figure 5.7: Scan of the total momentum to find the optimal cut in $p_{\mathrm{T}}(\Lambda_b^0)$ and $p_{\mathrm{T}}(\Lambda_b^{*0})$. The pion momentum cut is fixed to $p_{\mathrm{T}}(\pi_b^-) > 1.0\,\mathrm{GeV}/c$ and the impact parameter cut for every soft pion, $|d_0(\pi_s^{\pm})/\sigma_{d_0}| < 3.0$. The optimal point $p_{\mathrm{T}}(\Lambda_b^0) > 9.0\,\mathrm{GeV}/c$ is chosen.

The scan of the decay pion cut is shown in Figure 5.7. The score function starts flattening at the $1.0\,\mathrm{GeV}/c$ point, which is selected as the cut, $p_{\mathrm{T}}(\pi_b^-) > 1.0\,\mathrm{GeV}/c$.

5.8.3 Proper Lifetime of Λ_b^0

To suppress prompt backgrounds from the primary interaction, the decay vertex of the Λ_b^0 is required to be distinct from the primary vertex. To achieve this, cuts on $ct(\Lambda_b^0)$ and its significance $ct(\Lambda_b^0)/\sigma_{ct}$ are applied. The cut $ct(\Lambda_b^0) > 200\,\mu\mathrm{m}$ confirms

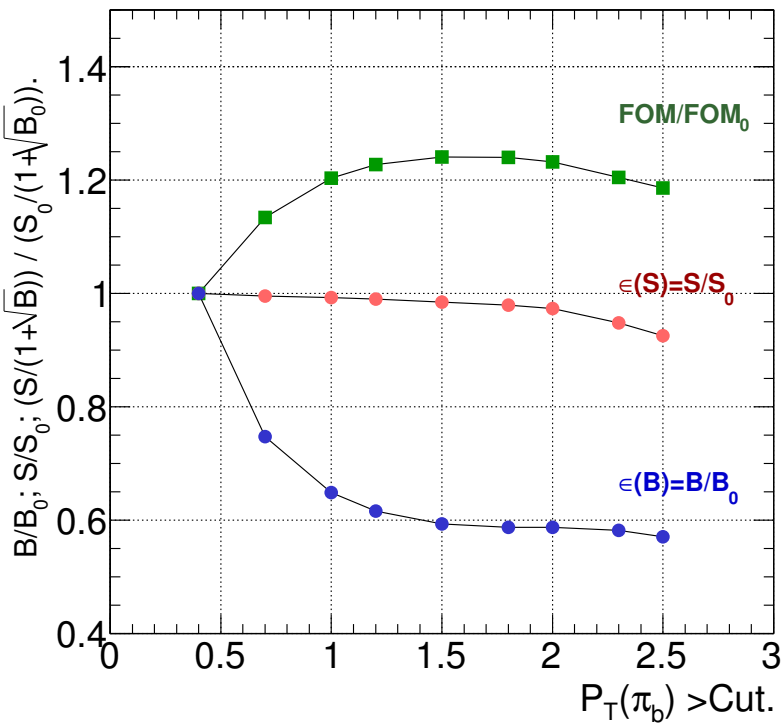

Figure 5.8: Scan of the Λ_b^0 decay pion transverse momentum to find the optimal $p_{\rm T}(\pi_b^-)$ cut. The total momentum cuts are fixed to the optimized values $p_{\rm T}(\Lambda_b^0) > 9.0\,{\rm GeV}/c$ and $p_{\rm T}(\Lambda_b^{*0}) > 9.0\,{\rm GeV}/c$. The impact parameter cut for every soft pion, $|d_0(\pi_s^{\pm})/\sigma_{d_0}| < 3.0$. The point $p_{\rm T}(\pi_b^-) > 1.0\,{\rm GeV}/c$ is chosen.

the cut $L_{xy} > 200\,\mu$m applied at the CDF triggers Level 2 and Level 3. The MC distributions of both $ct(\Lambda_b^0)$ and $ct(\Lambda_b^0)/\sigma_{ct}$ are shown in Figure 5.9. We select the cut on the proper lifetime significance based on the signal efficiency, specifically the cut $ct(\Lambda_b^0)/\sigma_{ct} > 6.0$ is $\gtrsim 99.5\%$ efficient for the Λ_b^{*0} signal.

We require the Λ_c^+ vertex to be close to the Λ_b^0 vertex by applying cuts on $ct(\Lambda_c^+ \leftarrow \Lambda_b^0)$ where the corresponding quantity $L_{xy}(\Lambda_c^+)$ is calculated with respect to the Λ_b^0 vertex. The requirement $ct(\Lambda_c^+ \leftarrow \Lambda_b^0) > -100\ \mu$m reduces contributions from Λ_c^+ baryons directly produced in $p\bar{p}$ interaction and from random combination of tracks

faking Λ_c^+ candidates which may have negative $ct(\Lambda_c^+)$ values. Similar cut values have been used in other CDF Λ_b^0 analyses. This requirement is also selected based on a signal efficiency which is $\gtrsim 99.5\%$. The corresponding MC data distribution is shown in Figure 5.9 (bottom plot).

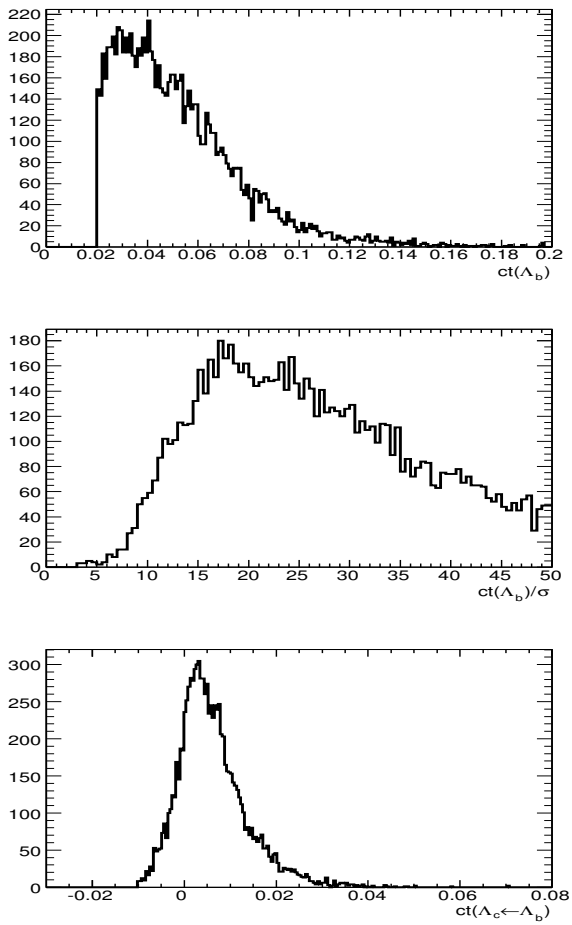

Figure 5.9: The distribution of the proper lifetime $ct(\Lambda_b^0)$ (upper plot) and its significance $ct(\Lambda_b^0)/\sigma_{ct}$ (middle plot) for the Λ_b^0 candidates resulting from the generated, simulated, and reconstructed hadron modes, $\Lambda_b^{*0} \to \Lambda_b^0 \pi_s^+ \pi_s^-$. The cut of $ct(\Lambda_b^0)/\sigma_{ct} > 6.0$ has an efficiency of $\gtrsim 99.5\%$. The bottom plot is a $ct(\Lambda_c^+ \leftarrow \Lambda_b^0)$ distribution. The cut $ct(\Lambda_c^+ \leftarrow \Lambda_b^0) > -100$ μm has also an efficiency of $\gtrsim 99.5\%$.

5.8.4 Impact Parameter $|d_0(\Lambda_b^0)|$

The cut on the impact parameter of the Λ_b^0 candidate is selected by requiring high efficiency of the Λ_b^0 candidates. The MC data distribution is shown in Figure 5.10. The cut $|d_0(\Lambda_b^0)| < 80$ μm used in the Σ_b analysis [51] is selected. The cut is practically fully efficient.

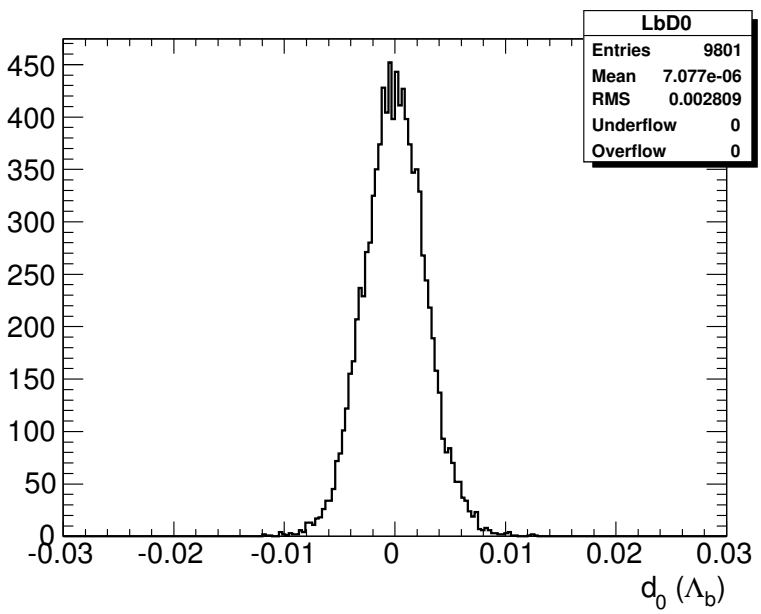

Figure 5.10: The distribution of the impact parameter $|d_0(\Lambda_b^0)|$ made with MC data. The cut $|d_0(\Lambda_b^0)| < 80$ μm is practically fully efficient.

5.8.5 Yields of the Λ_b^0 Signal

For our optimization scans discussed in the previous sections and Λ_b^0 yield estimates we use the fitter developed by R. Tesarek and co-workers [59] and by M. Martin, P. Maksimovich and co-workers [60, 55].

5.8.6 Fitter of the Λ_b^0 Signal

The Λ_b^0 signal is modeled by a Gaussian function.

The following backgrounds contribute to the mass spectrum of $M(\Lambda_b^0 \to \Lambda_c^+ \pi_b^-)$:

- Cabibbo suppressed decay $\Lambda_b^0 \to \Lambda_c^+ K^-$ with a peak at $\sim 50\,\mathrm{MeV}/c^2$ below the Λ_b^0 signal peak. The contribution is modeled by two Gaussians.
- Four-prong mis-identified B-mesons: all B-mesons with four tracks in the final state that are fully reconstructed. The $B \to 4\,\mathrm{prongs}$ modes produce a peak to the left of the Λ_b^0 signal peak and are modeled by a sum of a Gaussian and a Landau function.
- The remaining B-meson decays, modeled by the sum of an exponential function and a product of a bifurcated Gaussian with a step-down function.
- The remaining Λ_b^0 decays modeled by the sum of two Gaussians and the product of a bifurcated Gaussian and a step-down function.
- The combinatorial background which is described by an exponential function.

Several parameters of the combined background model are fixed, based on MC templates or ratios of branching fractions taken from known measurements.

5.8.7 Analysis Cuts and Yields of Λ_b^0 Events

The choice of cuts for the Λ_b^0 is summarized in Table 5.10. The cut values specified in this table override the ones listed in the Table 5.9.

The inclusive Λ_b^0 signals reconstructed according to the Table 5.10, fitted [59], and found with all datasets are shown in Figures 5.11 and 5.12. The bottom right plot

Variable	Cut value
$ct(\Lambda_b^0)/\sigma_{ct}$	> 6.0
$\lvert d_0(\Lambda_b^0)\rvert$	$< 80\,\mu$m
$ct(\Lambda_c^+ \leftarrow \Lambda_b^0)$	$> -100\,\mu$m
$p_{\mathrm{T}}(\Lambda_b^0)$	$> 9.0\,\mathrm{GeV}/c$
$p_{\mathrm{T}}(\pi_b^-)$	$> 1.0\,\mathrm{GeV}/c$
$\lvert m(\Lambda_c^+\pi^-) - m(\Lambda_b^0)\rvert$	$\in (5.561,\, 5.677)\,\mathrm{GeV}/c^2$, $\pm 3\sigma$

Table 5.10: The domain of cut values for Λ_b^0 signals chosen for further analysis. The mass range to be used for reconstruction of Λ_b^{*0} candidates is specified as well.

of Figure 5.12 shows a prominent Λ_b^0 signal in the $\Lambda_c^+\pi_b^-$ invariant mass distribution, reconstructed using the criteria listed in Table 5.10. A binned maximum-likelihood fit finds a signal of approximately $15,400$ candidates at the expected Λ_b^0 mass, with a signal to background ratio around 1.1/1.0.

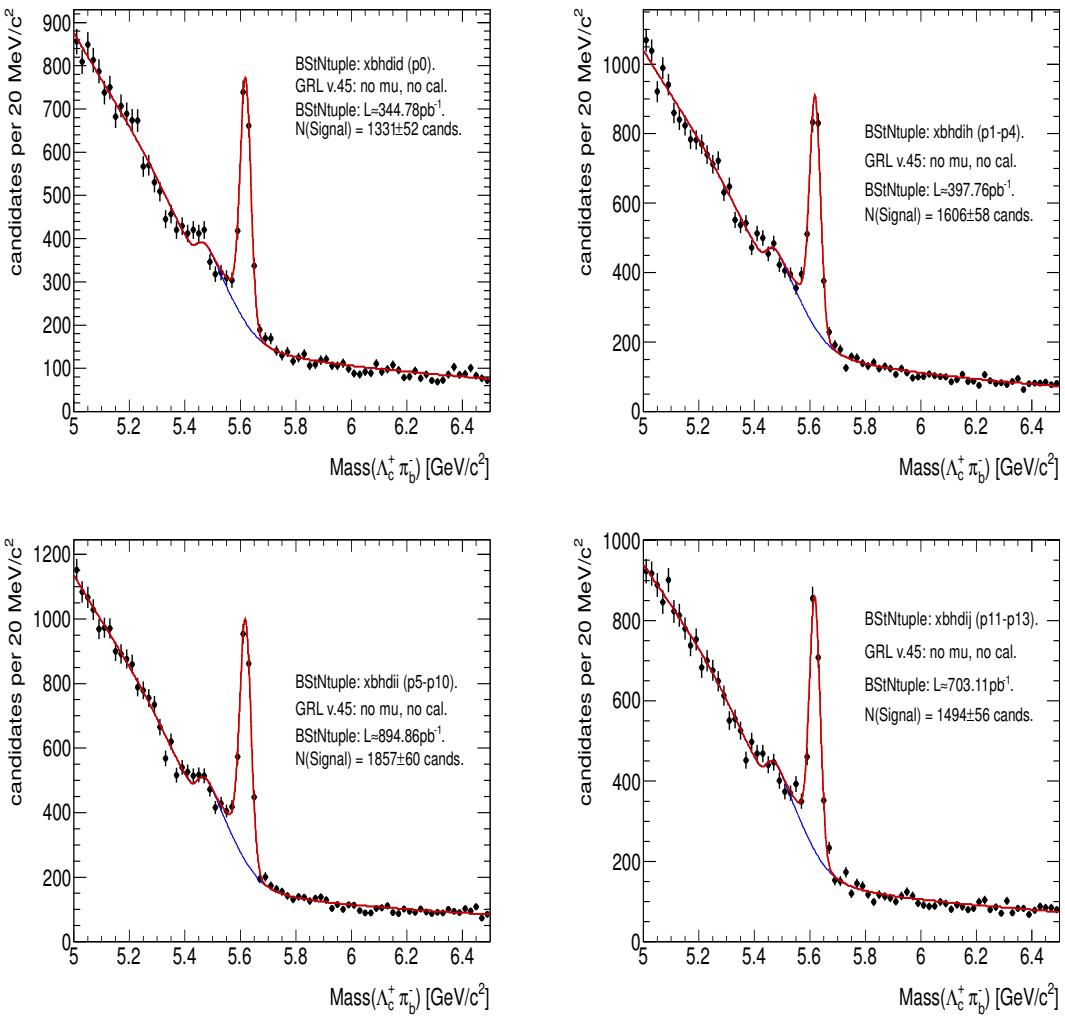

Figure 5.11: Inclusive Λ_b^0 signals with `xbhdid`, `xbhdih`, `xbhdii`, `xbhdij`, *BStNtuple* datasets. The number of candidates $N/20\,\mathrm{MeV}/c^2$ is plotted. The optimized cuts $ct(\Lambda_b^0) > 0.0200, ct(\Lambda_b^0)/\sigma_{ct} > 6.0, |d_0(\Lambda_b^0)| < 0.0080,\ p_\mathrm{T}(p) > 1.0\,\mathrm{GeV}/c,\ p_\mathrm{T}(\pi_b^-) > 1.0\,\mathrm{GeV}/c$, and $p_\mathrm{T}(\Lambda_b^0) > 9.0\,\mathrm{GeV}/c$ are applied here. The typical signal to background ratio is $S/B \approx (1.1...1.2)/1.0$.

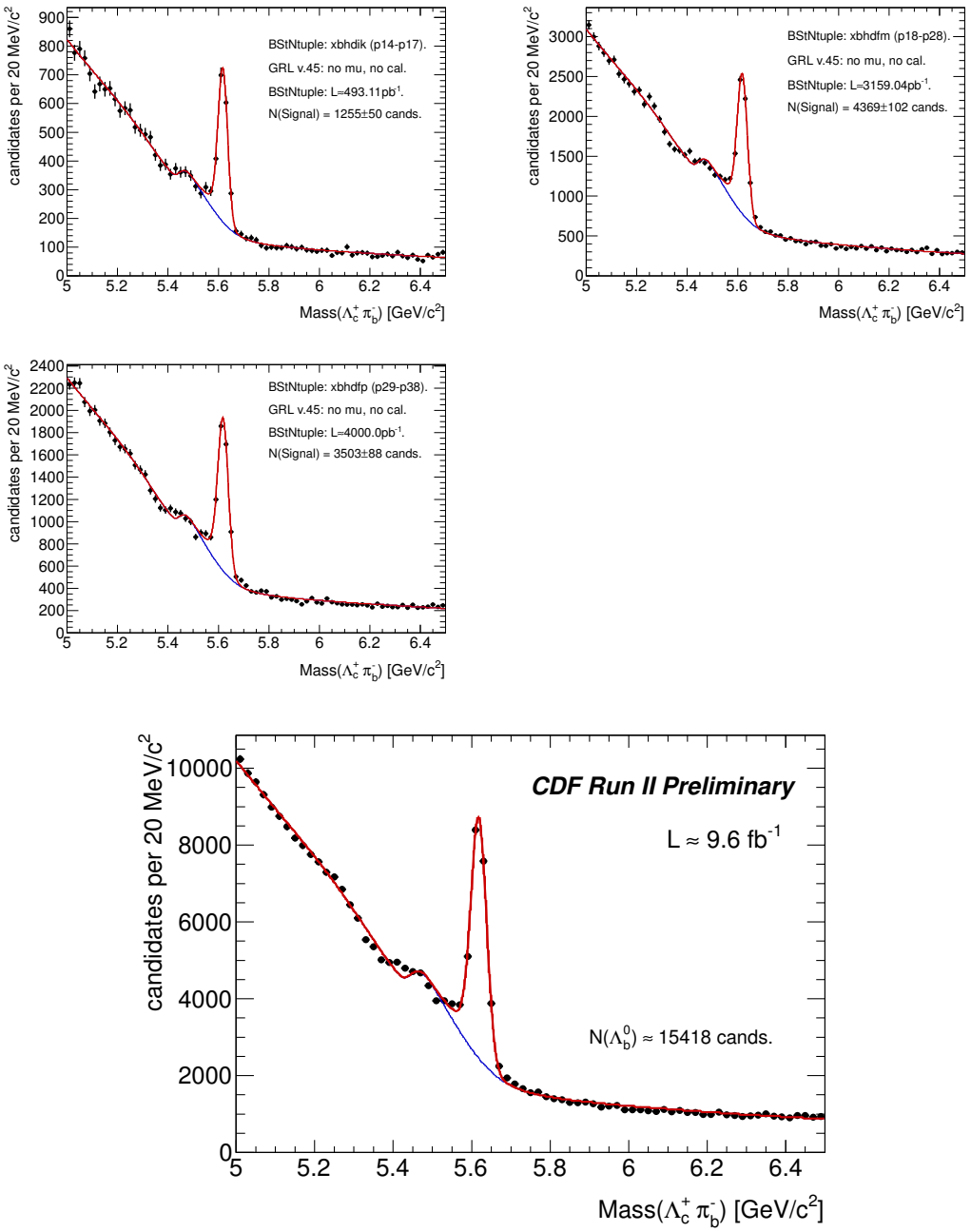

Figure 5.12: Inclusive Λ_b^0 signals with`xbhdik`, `xbhdfm` and `xbhdfp` *BStNtuple* datasets. The number of candidates $N/20\,\mathrm{MeV}/c^2$ is plotted. The optimized cuts $ct(\Lambda_b^0) > 0.0200, ct(\Lambda_b^0)/\sigma_{ct} > 6.0$, $|d_0(\Lambda_b^0)| < 0.0080$, $p_\mathrm{T}(p) > 1.0\,\mathrm{GeV}/c, p_\mathrm{T}(\pi_b^-) > 1.0\,\mathrm{GeV}/c$, and $p_\mathrm{T}(\Lambda_b^0) > 9.0\,\mathrm{GeV}/c$ are applied here. The typical signal to background ratio is $S/B \approx (1.0...1.2)/1.0$. The bottom right of the plot demonstrates the Λ_b^0 signal for $\int \mathcal{L}\,dt \approx 9.6\,\mathrm{fb}^{-1}$.

The corresponding yields are listed in Table 5.11. In the table, the Λ_b^0 signal yields are shown for every data-taking period. The yields of the fitted Λ_b^0 signals correspond to the cuts shown in Table 5.10.

BStNtuple dataset	Data taking period	$N_{\text{signal}}(\, p_{\text{T}}(\Lambda_b^0) > 9.0\,\text{GeV}/c,$ $p_{\text{T}}(p) > 2.0\,\text{GeV}/c,\, p_{\text{T}}(\pi_b^-) > 1.0\,\text{GeV}/c\,)$
`xbhdid`	0	1331 ± 52
`xbhdih`	1 – 4	1606 ± 58
`xbhdii`	5 – 10	1857 ± 60
`xbhdij`	11 – 13	1494 ± 56
`xbhdik`	14 – 17	1255 ± 50
`xbhdfm`	18 – 28	4369 ± 102
`xbhdfp`	29 – 38	3503 ± 88
total stat.	0 – 38	15418 ± 183

Table 5.11: The yields of optimized inclusive Λ_b^0 signals for all datasets. The analysis cuts are applied.

5.9 Λ_b^{*0}: Soft Pion Tracks

The search for Λ_b^{*0} resonance states challenges the tracking efficiency at low momenta. The pair of soft pions is where the tracking efficiency at low range becomes a critical factor.

5.9.1 Optimization of the Soft Pion Impact Parameter Significance

The scan of $|d_0(\pi_s^{\pm})/\sigma_{d_0}|$ is shown in Figure 5.13. The numerator of Eq. (5.1) is taken from MC while the denominator results from the fit of the right-side band of the experimental Q value spectrum, $Q \in (0.041, 0.083)\,\text{MeV}/c^2$. The other analysis

cuts are fixed as $p_{\mathrm{T}}(\Lambda_b^0) > 9.0\,\mathrm{GeV}/c$, $p_{\mathrm{T}}(\Lambda_b^{*0}) > 9.0\,\mathrm{GeV}/c$, and $p_{\mathrm{T}}(\pi_b^-) > 1.0\,\mathrm{GeV}/c$. The cut at $|d_0(\pi_s^\pm)/\sigma_{d_0}| < 3.0$ is chosen.

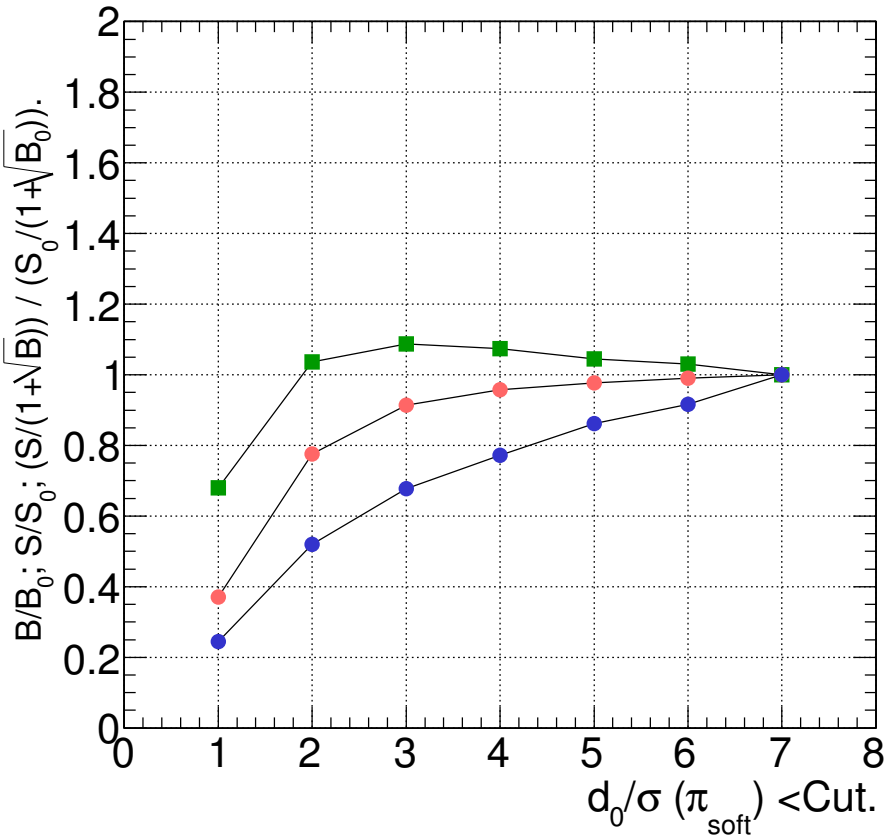

Figure 5.13: Scan of the cut on impact parameter of the soft pion, $|d_0(\pi_s^\pm)/\sigma_{d_0}|$. The Λ_b^0 decay pion transverse momentum cut is fixed at $p_{\mathrm{T}}(\pi_b^-) > 1.0\,\mathrm{GeV}/c$. The total transverse momentum cuts, $p_{\mathrm{T}}(\Lambda_b^0) > 9.0\,\mathrm{GeV}/c$ and $p_{\mathrm{T}}(\Lambda_b^{*0}) > 9.0\,\mathrm{GeV}/c$, are also used.

5.9.2 Silicon Standalone Hit Tracks versus COT Tracks

In Section 5.7, two options for the soft pion tracks were proposed (see Table 5.8), specifically,

- using the tracks above $p_{\mathrm{T}} = 200\,\mathrm{MeV}/c$ and having hits both in silicon trackers and in the COT.

- in addition to the above defined tracks, one can use also tracks having only silicon tracker hits available while leaving no hits in the COT, so called "Si standalone" tracks. We expect that this additional option will contribute to the prospective Λ_b^{*0} signal efficiency, though the resolution of the reconstructed signal is expected to be wider.

5.9.3 Soft $\pi_s^{\pm}$ Tracks in Λ_b^{*0} Monte-Carlo Data

We reconstruct the Λ_b^{*0} signal when only one of the pair of soft pion tracks has only SVX II hits while having no hits in COT. The other track has COT hits according to the criteria outlined in Table 5.8. The MC data distribution of the Q value for this particular case is shown in Figure 5.14. The analysis cuts of Table 5.10 are applied. When we use only the soft pion tracks having at least 3 $r-\phi$ hits in SVX II and at least 10 stereo and axial COT hits together, the distribution reveals finer resolution as is demonstrated in Figure 5.15. The resolutions in the Q value for the Λ_b^{*0} Monte-Carlo signal are listed in Table 5.12. The Λ_b^{*0} signal is successfully reconstructed with one of the soft pions leaving a silicon standalone track, though the resolution becomes $\approx 41\%$ wider, i.e. $(\sigma_{aver} \approx 2.02)/(\sigma_{aver} \approx 1.43) \approx 1.41$. The fraction of Λ_b^{*0} candidates reconstructed with one pion having only SVX II hits amounts to $\approx 12\%$.

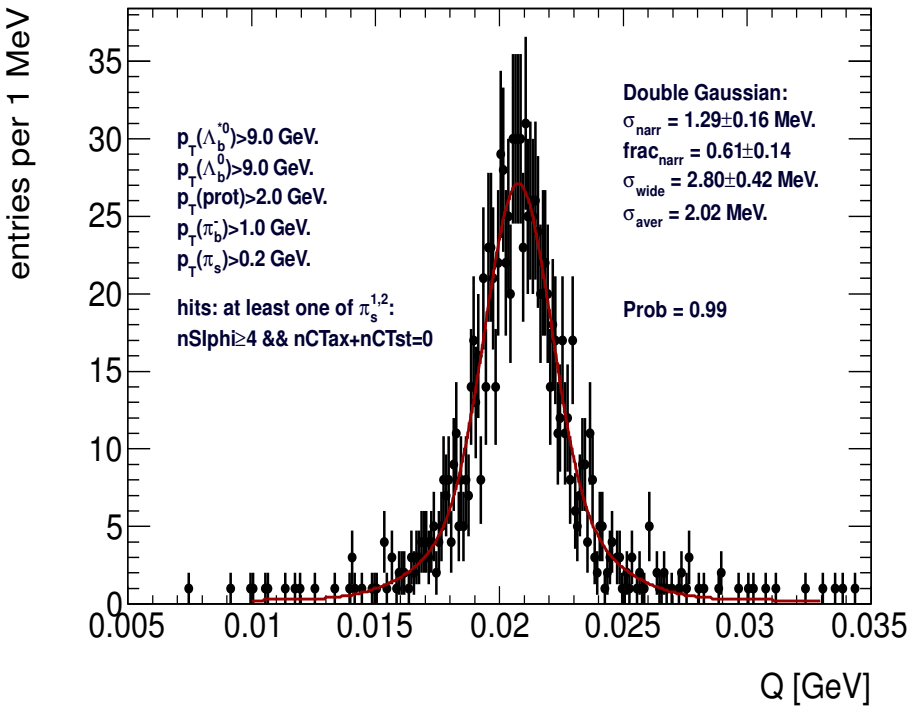

Figure 5.14: The distribution of the Q value in MC data: one soft pion track is SVX II standalone. The analysis cuts are applied.

State	π_s hits combination	σ_n, MeV/c^2	σ_w, MeV/c^2	g_n, fraction	σ_{aver}, MeV/c^2
Λ_b^{*0}	$N_{r-\phi}$(SVX II) ≥ 4 **and** $(N_{\rm ax}+N_{\rm st})$(COT) < 1	1.29 ± 0.2	2.8 ± 0.4	0.61 ± 0.14	≈ 2.02
Λ_b^{*0}	$N_{r-\phi}$(SVX II) ≥ 3 **and** $(N_{\rm ax}+N_{\rm st})$(COT) ≥ 10	0.91 ± 0.02	2.28 ± 0.09	0.72 ± 0.02	≈ 1.43

Table 5.12: Resolution of the detector for Λ_b^{*0} signals reconstructed with the MC data. The double Gaussian parameters $\sigma_{n,w}$ and relative fraction of the first, narrow core Gaussian, g_n, are listed in the table. The soft pion tracks have $p_{\rm T} > 0.2$ GeV/c^2 and two cases of SVX II and COT hit combinations.

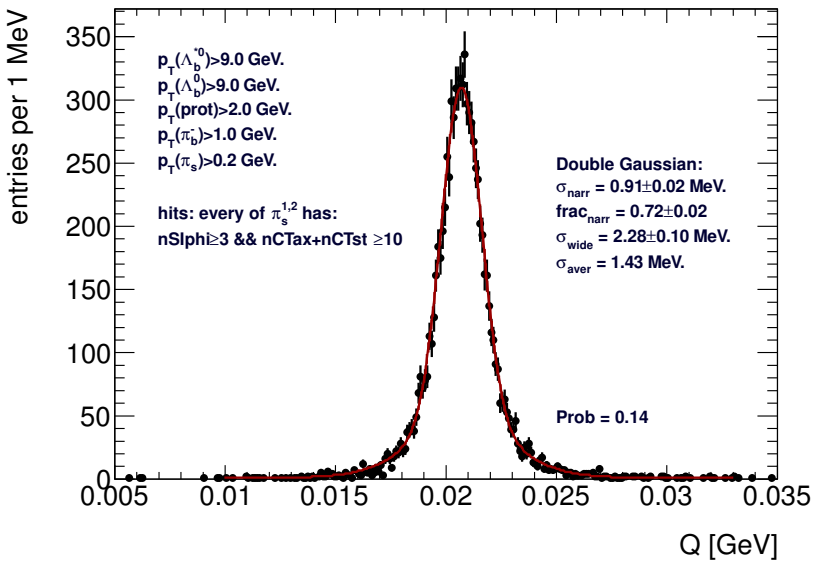

Figure 5.15: The distribution of the Q value in MC data: one soft pion track is silicon standalone or has COT hits as well. The analysis cuts are applied.

5.9.4 $p_{\mathrm{T}} > 0.2$ GeV/c^2 Cut versus Standard Tracks with $p_{\mathrm{T}} > 0.4$ GeV/c^2

As we expect that the soft pion tracks have their transverse momentum p_{T} as low as 200 MeV/c^2 but that the hits are present both in SVX II and the COT (second line in Table 5.12), it is useful to estimate the relative efficiency of our choice with respect to the standard track quality criteria listed in Table 5.7 and applied to the tracks of Λ_b^0 candidates.

We make the comparison using a MC sample and applying to the soft pion the standard, Table 5.7, and the loosened, used in this analysis, Table 5.12 criteria. The response of the CDF detector is shown in Figure 5.16. The relative efficiency of the $p_{\mathrm{T}} > 0.4\,\mathrm{GeV}/c^2$ cut with respect to our default analysis cut of $p_{\mathrm{T}} > 0.4\,\mathrm{GeV}/c^2$ can

be estimated as:

$$\frac{N_{cands}(p_{\rm T} > 0.4\,{\rm GeV}/c^2)}{N_{cands}(p_{\rm T} > 0.2\,{\rm GeV}/c^2)} = (3701 \pm 62)/(9472 \pm 99) = 0.391 \pm 0.008.$$

In other words, the relaxed requirements on the soft pion tracks increase the reconstructed yield of Λ_b^{*0} candidates by a factor of ~ 2.56.

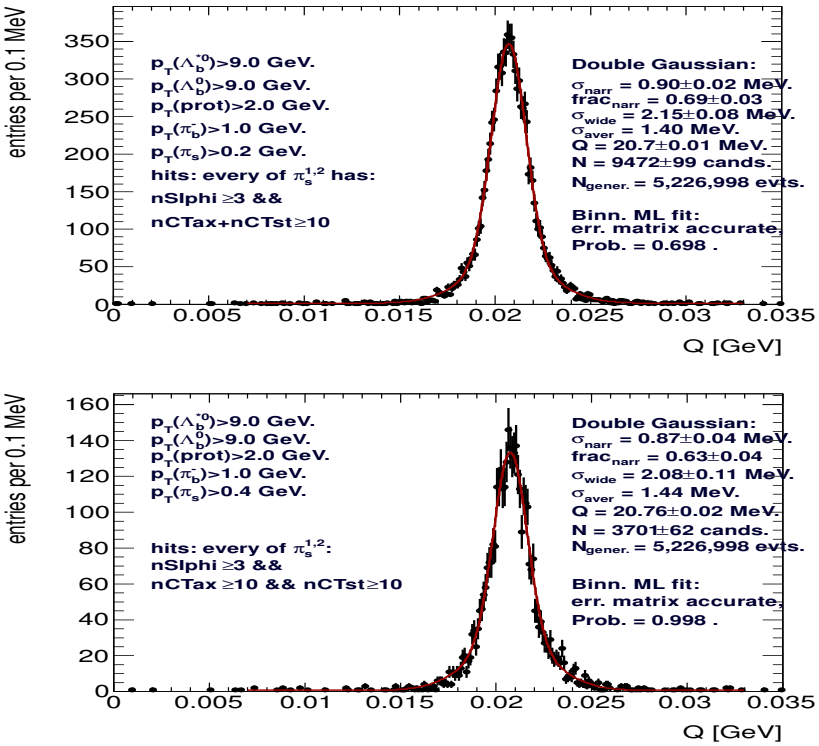

Figure 5.16: The response of the CDF detector to the Λ_b^{*0} signals after the modes generated with zero natural width, $\Lambda_b^{*0} \to \Lambda_b^0 \pi_s^+ \pi_s^-$, are simulated, reconstructed and ntuplized. The analysis cuts are applied. Upper plot: the soft pion tracks are required to have hits in the SVX II $N_{r-\phi}(\text{SVX II}) \geq 3$ and $(N_{\rm ax} + N_{\rm st})(\text{COT}) \geq 10$ and momentum $p_{\rm T} > 0.2$ GeV/c^2. Bottom plot: the soft pion track is required to be the same as the standard ones, i.e. $p_{\rm T} > 0.4$ GeV/c^2 and $N_{r-\phi}(\text{SVX II}) \geq 3$ and $N_{\rm ax}(\text{COT}) \geq 10$ and $N_{\rm st}(\text{COT}) \geq 10$. Here the MC data sample produced for for $Q = 20.66\,{\rm MeV}/c^2$ or $M = 5920.00\,{\rm MeV}/c^2$.

π_s hits	ΔM, MeV/c^2	σ_n, MeV/c^2	g_n, fraction	σ_w, MeV/c^2	σ_{av}, MeV/c^2
$N_{r-\phi}$(SVX II) ≥ 4 **and** $(N_{\rm ax}+N_{\rm st})$(COT) < 1	$145.90^{+0.04}_{-0.04}$	$1.42^{+0.04}_{-0.04}$	...	...	≈ 1.42
$N_{r-\phi}$(SVX II) ≥ 3 **and** $(N_{\rm ax}+N_{\rm st})$(COT) ≥ 10	$145.49^{+0.01}_{-0.01}$	$0.64^{+0.03}_{-0.03}$	$0.47^{+0.05}_{-0.05}$	$1.40^{+0.07}_{-0.07}$	≈ 1.11

Table 5.13: Resolution of the detector for D^{*+} signals reconstructed with experimental data. The double Gaussian parameters $\sigma_{n,w}$ and relative fraction of the first, narrow core Gaussian, g_n, are listed in the table. The Breit-Wigner width has been fixed to $\Gamma = 0.096\,\text{MeV}/c^2$, the PDG value. The soft pion tracks have $p_{\rm T} > 0.2$ GeV/c^2 and two cases of SVX II and COT hit combinations.

5.9.5 Soft $\pi_s^{\pm}$ Tracks with the D^{*+} Experimental Signal

We have also analyzed the case of SVX II standalone versus SVX II and COT hits using the D^{*+} signal available for the `xbhdij` *BStNtuple* dataset stored by the SAM system. The mass difference $\Delta M(D^{*+})$ distribution reconstructed with the soft pion having produced hits in the SVX II silicon tracker system only is shown in Figure 5.17. The soft pions are taken within $p_{\rm T}(\pi_s^+) \in (0.2, 0.3)\,\text{GeV}/c$ range, and the total momentum of the D^0 is required to be $p_{\rm T}(D^0) < 5.0\,\text{GeV}/c$. The latter cut is applied to achieve a reasonable S/B ratio for a D^{*+} signal in this particular kinematical domain with quite slow π_s^+. Again the D^{*+} signal is successfully reconstructed using SVX II only soft pion tracks similar to the case with Λ_b^{*0} MC data. The signal resolution is wider as expected. The fits of the signals are made with single or double Gaussians convolved with a Breit-Wigner of a width fixed to the PDG value, $\Gamma = 0.096\,\text{MeV}/c^2$. The case when soft tracks are reconstructed with ≥ 3 SVX II $r-\phi$ hits and ≥ 10 COT stereo and axial hits together is shown in Figure 5.18.

The fit results of the D^{*+} signal are listed in Table 5.13. The average resolution

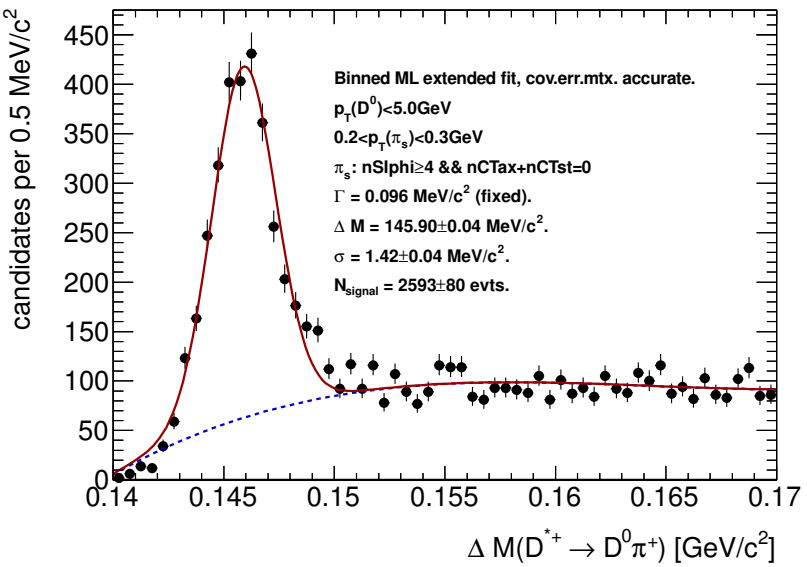

Figure 5.17: The distribution of the $\Delta M = M(D^0\pi^+) - M(D^0), D^0 \to K^-\pi^+$ value in MC data: one soft pion track is SVX II standalone.

for SVX II only reconstructed D^{*+} candidates is wider by $\approx 28\%$, i.e. $(\sigma_{aver} \approx 1.42)/(\sigma_{aver} \approx 1.11) \approx 1.28$. The fraction of SVX II only D^{*+} candidates for the kinematic region considered, i.e., $0.2\,\mathrm{GeV}/c < p_{\mathrm{T}}(\pi_s^+) < 0.3\,\mathrm{GeV}/c$ with $p_{\mathrm{T}}(D^0) < 5.0\,\mathrm{GeV}/c$, comprises $\approx 22\%$ of the total number of reconstructed D^{*+} candidates. The concern here is the fitted position of the D^{*+} signal in ΔM which is by $145.90 - 145.49 = 0.41\,\mathrm{MeV}/c^2$ higher for the candidates with SVX II only soft pions with respect to the nominal ones with COT hits included. Relative to the PDG value, the D^{*+} candidates with silicon standalone soft pions are $145.90 - 145.421 = 0.48\,\mathrm{MeV}/c^2$ higher while the nominal ones $(+0.07\,\mathrm{MeV}/c^2)$ can serve as a conservative input for the mass scale uncertainty estimate.

Apparently there is an issue with the mass scale for the SVX II only soft pions. A procedure or calibration signal is needed where the observed uncertainty is properly weighted or accounted *in situ* (in case of a calibration signal) and will correspond

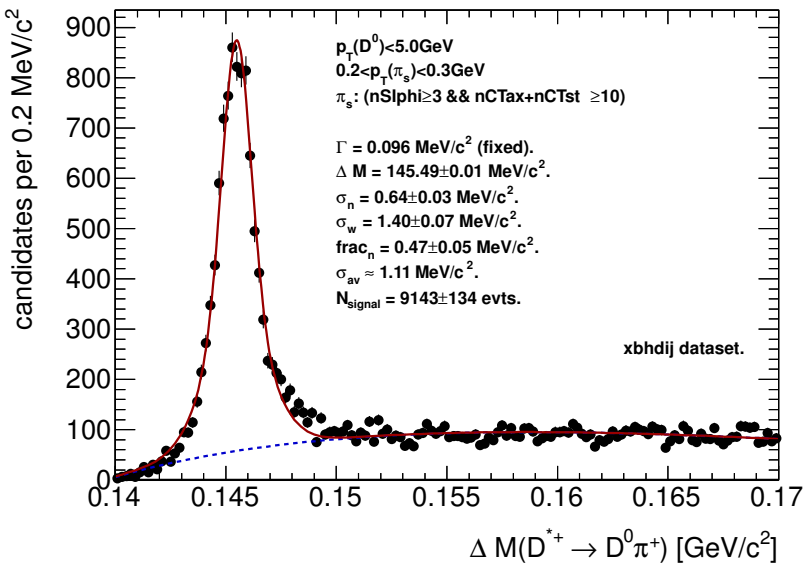

Figure 5.18: The distribution of the $\Delta M = M(D^0\pi^+) - M(D^0)$, $D^0 \to K^-\pi^+$ value in experimental data: the soft pion tracks always have COT hits according to criteria $(N_{\rm ax} + N_{\rm st})({\rm COT}) \geq 10$ (with $N_{r-\phi}({\rm SVX\ II}) \geq 3$). The soft pion track has $0.2\,{\rm GeV}/c < p_{\rm T}(\pi_s^+) < 0.3\,{\rm GeV}/c$ and $p_{\rm T}(D^0) < 5.0\,{\rm GeV}/c$.

to our Λ_b^{*0} experimental signal spectrum. The D^{*+} signal has a spectrum quite different from the bottom baryon one and cannot be used directly without some re-weighting. The other possibility lies in the charm baryons $\Sigma_c^{0,++}$. Their Q value is $\approx 28\,{\rm MeV}/c^2$, which is quite close to our search domain. Moreover a large fraction of $\Sigma_c^{0,++}$ triggered by the CDF displaced Two-Track Trigger come from B baryons.

5.10 Signal Resolution Model

In this section we describe the MC study aimed at calculating the detector resolution for the Λ_b^{*0} experimentally observed signals.

The resolution calculations are based on large statistics Monte Carlo samples. The exclusive $\Lambda_b^{*0} \to \Lambda_b^0 \pi_s^+ \pi_s^-$ modes for positive charge states are generated with `Bgen` with the natural width of a particular mode set to zero to measure only detector effects. The output of `Bgen` is fed into the full detector simulation `cdfSim` and then reconstructed with `ProductionExe`. The CDF realistic Monte Carlo software release `version 6.1.4mc` is used and packaged for CDF B-Physics specific analyses. The bottom baryon momentum spectra are re-weighted and corrected according to the experimental ones.

The reconstructed MC data are used as input to `BottomMods CandsExe`, version 80 executable to ntuplize the reconstructed data into `BStNtuple`. The final `BStNtuple` files are analyzed, and the detector response spectra are fitted with Gaussians.

Figure 5.19 shows the shape of the CDF detector response for Λ_{b1}^{*0} state corresponding to a predicted mass $M(\Lambda_{b1}^{*0}, J^P = \frac{1}{2}^-) = 5920.00\,\mathrm{MeV}/c^2$. The distribution is fitted with a sum of double Gaussian functions:

- the fraction of a narrow Gaussian, frac_n, the width of the narrow Gaussian, σ_n, and the width of a second, wider Gaussian, σ_w, are allowed to float; the corresponding fit is shown in the upper plot of Figure 5.19.

- the fraction of a narrow Gaussian, frac_n, the width of the narrow Gaussian, σ_n, and the ratio of widths, $\alpha = \frac{\sigma_w}{\sigma_n}$, are floating parameters in this case; the corresponding fit is shown in the lower plot of Figure 5.19.

The results of the fits for both states are listed in Table 5.14. We use the resolution

model fitted with MC data for the soft pion momentum $p_{\rm T}(\pi_{soft}) > 0.2\,{\rm GeV}/c^2$. The soft pion tracks are required to have hit number $N_{r-\phi}({\rm SVXII}) \geq 3$ and $(N_{\rm ax} + N_{\rm st})({\rm COT}) \geq 10$.

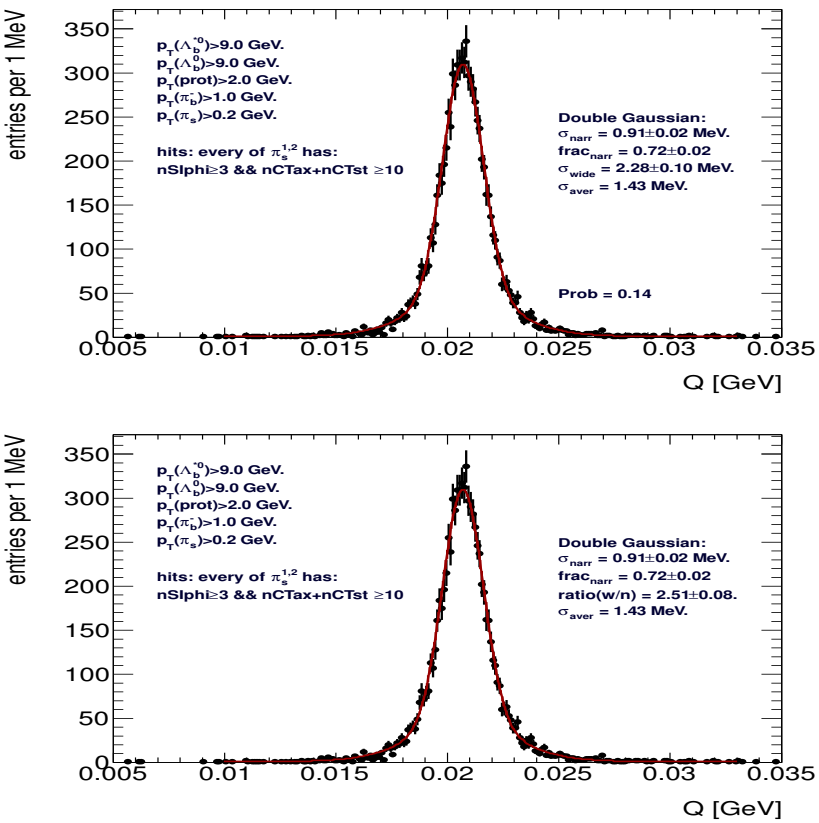

Figure 5.19: The response of the CDF detector to the Λ_b^{*0} signals after the modes generated with zero natural width, $\Lambda_b^{*0} \to \Lambda_b^0 \pi_s^+ \pi_s^-$ are simulated, reconstructed and ntuplized. The analysis cuts are applied. The soft pion tracks are required to have hits in the SVX II, $N({\rm SVX\ II}) \geq 3$ and $(N_{\rm ax} + N_{\rm st})({\rm COT}) \geq 10$. The $Q-$value spectrum, where $Q = M(\Lambda_b^0 \pi_s^+ \pi_s^-) - M(\Lambda_b^0) - 2 \cdot m_\pi$, is subjected to a fit with a double Gaussian: both widths are floating (upper plot), and the ratio$(w/n) = \sigma_w/\sigma_n$ is floating.

Soft pions $\pi_s^{1,2}$	σ_n, MeV/c^2	σ_w, MeV/c^2	fraction, g_n	$\alpha = \sigma_w/\sigma_n$
$p_{\rm T}(\pi_s^{1,2}) > 0.2\,{\rm GeV}/c^2$, $N_{r-\phi}({\rm SVX\ II}) \geq 3$ **and** $(N_{\rm ax} + N_{\rm st})({\rm COT}) \geq 10$	0.91 ± 0.02	2.28 ± 0.09	0.72 ± 0.02	2.51 ± 0.08

Table 5.14: Resolution of the detector for Λ_b^{*0} signals. The double Gaussian parameters $\sigma_{n,w}$ and relative fraction of the first, narrow core Gaussian, g_n, are listed in the table. The values quoted are used in the signal model of the fitter.

5.11 Λ_b^{*0} Signal Area

This is a blind analysis. We open the signal area after applying the analysis cuts explained in Section 5.8.

The signal function is parameterized by two Gaussians (see Eq. 5.2) taken with widths $\sigma_{n,w}$ and weights g_n, $(1 - g_n)$ according to Monte-Carlo simulation studies:

$$\mathcal{S}(Q; Q_0, \sigma_n, g_n, \sigma_w) = g_n \cdot \mathcal{G}_n(Q; Q_0, \sigma_n) + (1 - g_n) \cdot \mathcal{G}_w(Q; Q_0, \sigma_w) \quad (5.2)$$

$$\mathcal{S}(Q; Q_0, \sigma_n, g_n, \alpha) = g_n \cdot \mathcal{G}_n(Q; Q_0, \sigma_n) + (1 - g_n) \cdot \mathcal{G}_w(Q; Q_0, \alpha \cdot \sigma_n) \quad (5.3)$$

$$\text{where } \alpha = \frac{\sigma_w}{\sigma_n} \text{ is considered as a nuisance parameter and fixed from MC.}$$

In Eq. 5.2 the nuisance parameters are σ_n, σ_w, and g_n. These parameters are fixed from MC. Another option (see Eq. 5.3) is when the width ratio, $\alpha = \frac{\sigma_w}{\sigma_n}$, is considered as a nuisance parameter together with g_n to be fixed from MC. The Gaussian resolutions are listed in Table 5.14 of Section 5.10.

The background is described by a second order Chebyshev polynomial, Eq. 5.4,

$$\mathcal{BG}(Q; C, a_1, a_2) = \mathcal{P}^2(Q; C, a_1, a_2)\,, \quad (5.4)$$

where C, a_1, and a_2 are second order Chebyshev $\mathcal{P}^2$ polynomial coefficients which are also considered to be nuisance parameters.

The full model for the Q value spectra describes a single narrow structure on top of a smooth background. The parameters of interest are the position of the signal Q_0 and its yield, N_{cand} . The negative logarithm of the extended likelihood function (NLL) is minimized over the unbinned set of Q values observed for the candidates in our sample. The Q value spectrum is fit over the range $0.006 - 0.075\,\mathrm{GeV}/c^2$. The signal area is shown in Figure 5.20. This is a baseline spectrum and fit. The results

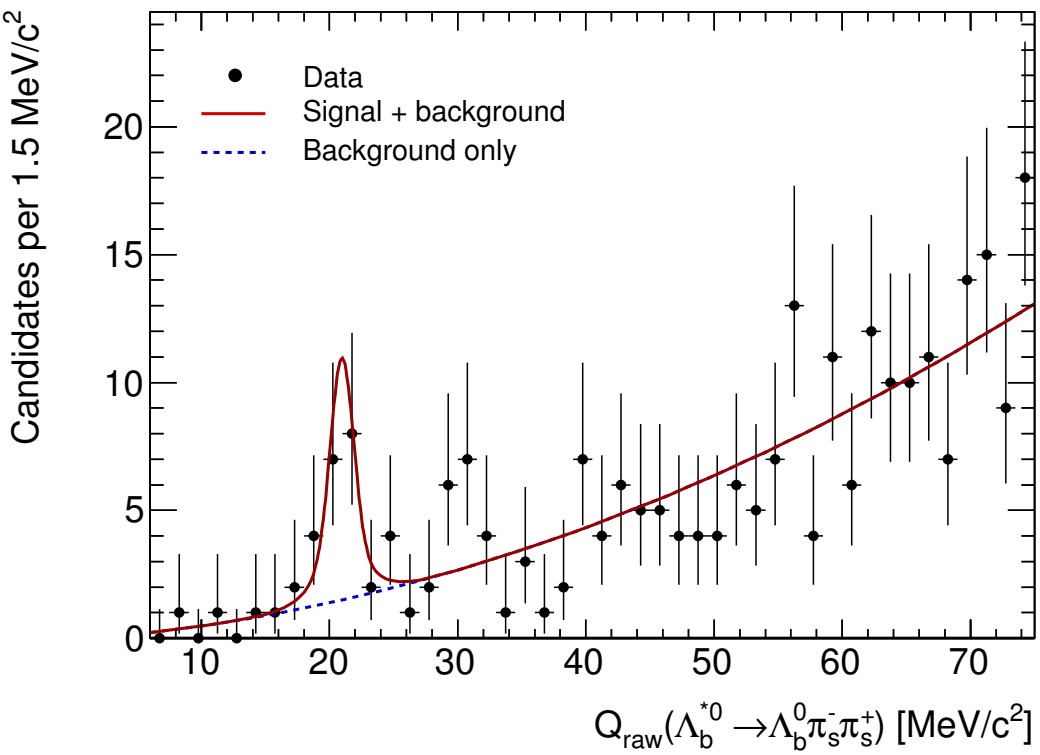

Figure 5.20: The projection of the unbinned fit. The Q value for the Λ_b^{*0} candidates is shown within the range $(0.006, 0.075)\,\mathrm{MeV}/c^2$. The soft pion tracks are above p_T of $200\,\mathrm{MeV}/c$ and are always required to have hits in the ranges $N_{r-\phi}(\mathrm{SVX\ II}) \geq 3$ and $(N_\mathrm{ax} + N_\mathrm{st})(\mathrm{COT}) \geq 10$; see results of the fit summarized in Table 5.15.

of the fit are summarized in Table 5.15.

Another alternative of the signal model is to fix only the ratio of the widths

Λ_b^{*0} : Parameters	Value	+HiError	-LoError	Comments
Q, MeV/c^2, Λ_b^{*0} pole	20.96	+0.35	−0.35	MINOS
N, evts, Λ_b^{*0} yield	17.3	+5.3	−4.6	MINOS
N_b, evts, background	238	+15	−15	MINOS
$-\log(\mathcal{L})$	−1902.777			minimized NLL

Table 5.15: Statistics of $\int \mathcal{L}\, dt \approx 9.6\,\text{fb}^{-1}$ from run periods 0 - 38, `GRL,v.45`: the fit results from the Λ_b^{*0} Q-value spectrum are shown in Fig. 5.20. The errors of the signal fit parameters have been calculated by MINOS. The Gaussian widths are fixed from the MC resolution model. This is the baseline fit.

and leave the narrow width floating. This model has been fitted from the MC and its results and parameters are shown in the Section 5.10, Table 5.14. The Q value spectrum with the projection of the unbinned fit is shown in Figure 5.21. The results of the fit when the ratio of widths is fixed are summarized in Table 5.16.

Λ_b^{*0} : Parameters	Value	+HiError	-LoError	Comments
Q, MeV/c^2, Λ_b^{*0} pole	21.07	+0.30	−0.46	MINOS
N, evts, Λ_b^{*0} yield	16.0	+6.4	−5.4	MINOS
N_b, evts, background	239	+17	−16	MINOS
$-\log(\mathcal{L})$	−1902.828			minimized NLL

Table 5.16: The projection of the unbinned fit. Statistics of $\int \mathcal{L}\, dt \approx 9.6\,\text{fb}^{-1}$ from run periods 0 - 38, `GRL,v.45`: the fit results from the Λ_b^{*0} Q-value spectrum are shown in Fig. 5.21. The errors of the signal fit parameters have been calculated by MINOS. The ratio of Gaussian widths is fixed from the MC resolution model, see Table 5.14.

To understand how much we would gain if we were to include the silicon standalone tracks, we demonstrate the corresponding Q value spectrum with the projection of the unbinned fit in Figure 5.22. Here one of the soft pion tracks is allowed to have only SVX II hits and no COT hits; the second soft pion track must comply with our standard requirement of COT hits. The fit model is with fixed widths. The

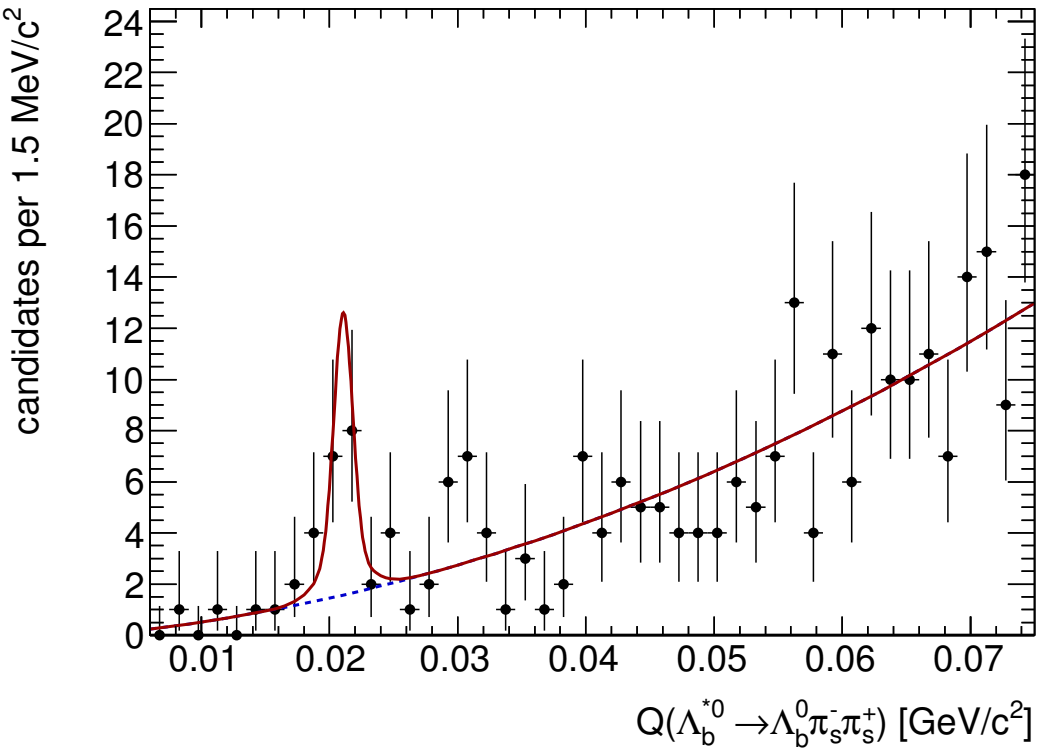

Figure 5.21: The projection of the unbinned fit. The Q value for the Λ_b^{*0} candidates is shown within the range $(0.006, 0.075)\,\mathrm{MeV}/c^2$. The soft pion tracks are above p_T of $200\,\mathrm{MeV}/c$ and are always required to have hits in the ranges $N_{r-\phi}(\mathrm{SVX\ II}) \geq 3$ and $(N_\mathrm{ax} + N_\mathrm{st})(\mathrm{COT}) \geq 10$; here the width ratio in the signal model is fixed, see results of the fit summarized in Table 5.16.

results of the fit when the silicon standalone tracks are included for one of the soft pions are summarized in Table 5.17.

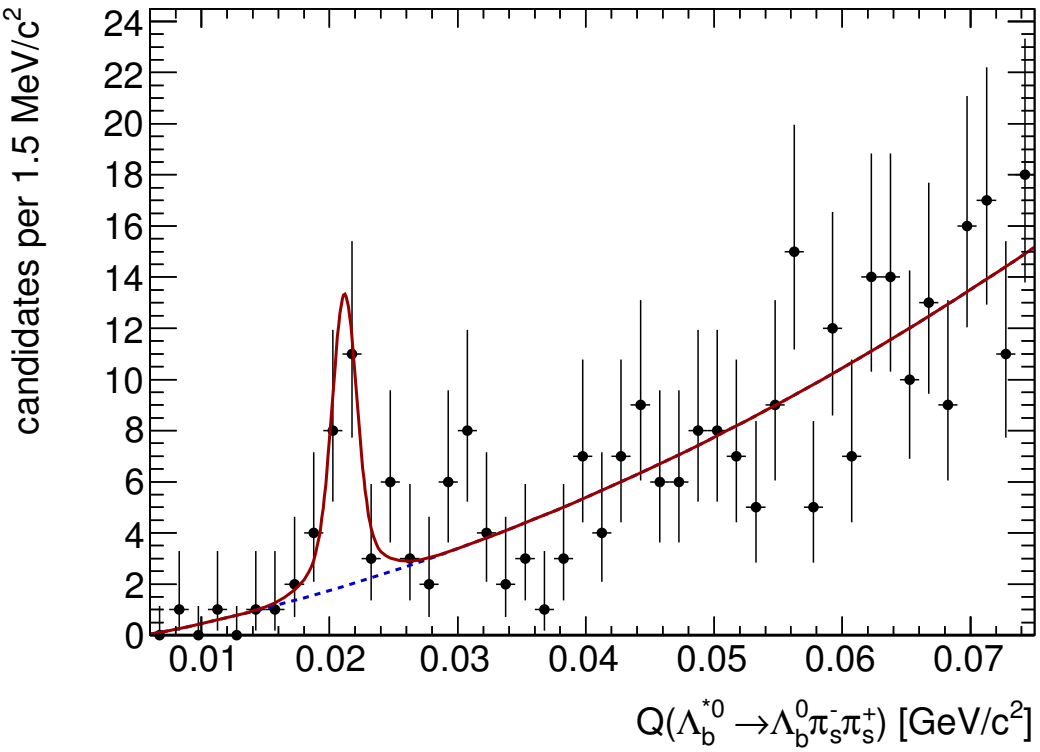

Figure 5.22: The projection of the unbinned fit. The Q-value for the Λ_b^{*0} candidates is shown within the range $(0.006, 0.075)\,\mathrm{MeV}/c^2$. The case when one of the soft pion tracks is allowed to have only SVX II hits and no COT hits; the second soft pion track must comply with our standard requirement of COT hits. The widths are fixed to MC values.

5.11.1 Signal Significance

The significance of the signals is determined using a log-likelihood ratio statistic [61, 62],

$$D \;=\; -2\,\ln\frac{\mathcal{L}_0}{\mathcal{L}_1} \;=\; -2\,\Delta(\ln\mathcal{L})\,.$$

We define hypothesis $\mathcal{H}_1$ corresponding to the presence of a Λ_b^{*0} signal on top of the background. The null $\mathcal{H}_0$ hypothesis is the background model described by

Λ_b^{*0} : Parameters	Value	+HiError	-LoError	Comments
Q, MeV/c^2, Λ_b^{*0} pole	21.12	+0.32	−0.33	MINOS
N, evts, Λ_b^{*0} yield	21.8	+6.0	−5.3	MINOS
N_b, evts, background	285	+18	−17	MINOS
$-\log(\mathcal{L})$	−2345.2			minimized NLL

Table 5.17: The projection of the unbinned fit. Statistics of $\int \mathcal{L}\, dt \approx 9.6\,\text{fb}^{-1}$ from run periods 0 - 38, `GRL,v.45`: the fit results from the Λ_b^{*0} Q-value spectrum are shown in Fig 5.22. The errors of the signal fit parameters have been calculated by MINOS.

the second order Chebyshev polynomial. The difference in the number of degrees of freedom is $5 - 3 = 2$ when both Gaussian widths are fixed. The results are summarized in Table 5.18. The baseline signal fit has a significance of ≈ 4.6.

Fit of the spectrum	$-2 \cdot \Delta(\log \mathcal{L})$	ΔNDF	Prob(χ^2)	N_σ	Comment
Baseline spectrum	$-2 \cdot (-12.993)$	2	$2.276207 \cdot 10^{-6}$	4.6	Table 5.15.
Fixed width ratio	$-2 \cdot (-13.044)$	3	$9.141224 \cdot 10^{-6}$	4.3	Table 5.16.
Si only pion incl.	$-2 \cdot (-15.601)$	2	$1.677150 \cdot 10^{-7}$	5.1	Table 5.17.

Table 5.18: Estimation of the significance.

Another method is to use the ProfileLikelihoodCalculator tool from the RooStats package. This calculator makes a significance estimate using the formula

$$N_\sigma = \sqrt{(-2 \cdot \Delta(\log \mathcal{L}))}\,.$$

The estimates are enhanced, see Table 5.19.

5.11.2 Signal Significance with Toy Monte-Carlo

The distribution of $-\Delta(\log \mathcal{L})$ for the Toy MC corresponding to the search window of $Q \in (0., 50.)\,\text{MeV}/c^2$ is shown in Figure 5.23. The experimental data point of

Fit of the spectrum	$-2 \cdot \Delta(\log \mathcal{L})$	N_σ	Comment
Baseline spectrum	$-2 \cdot (-12.993)$	≈ 5.1	Table 5.15.
Fixed width ratio	$-2 \cdot (-13.044)$	≈ 5.1	Table 5.16.
Si only pion incl.	$-2 \cdot (-15.601)$	≈ 5.6	Table 5.17.

Table 5.19: Estimation of the significance using the ProfileLikelihoodCalculator tool from the RooStats package.

12.99 is marked with a red line. For this case 174 entries are above the experimental data point. The number translates to the probability$p = 2.3 \cdot 10^{-4}$ corresponding to $N_\sigma = 3.5$. Thence the conservative significance estimate of the observed Λ_b^{*0} signal is 3.5σ in Gaussian terms.

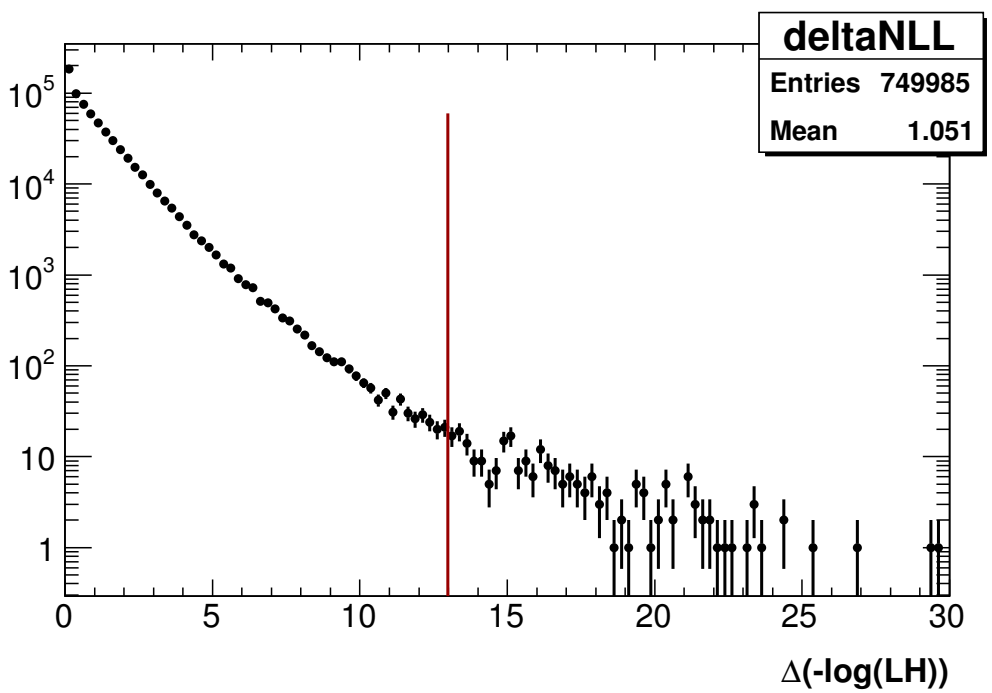

Figure 5.23: $-2\Delta(\log \mathcal{L})$ distribution for the search window $Q \in (0., 50.)\,\mathrm{MeV}/c$.

The distribution of $-\Delta(\log \mathcal{L})$ for the Toy MC corresponding to the fixed position

of the signal for the LHCb measurement, $Q = 21.25\,\mathrm{MeV}/c^2$, is shown in Fig. 5.24. The experimental data point of 12.65 is marked with a red line. In this case only 1 entry is above the experimental data point, corresponding to $p \sim 1.3 \cdot 10^{-6}$ or $N_\sigma \sim 4.7$, i.e. above $\sim 4.0\sigma$.

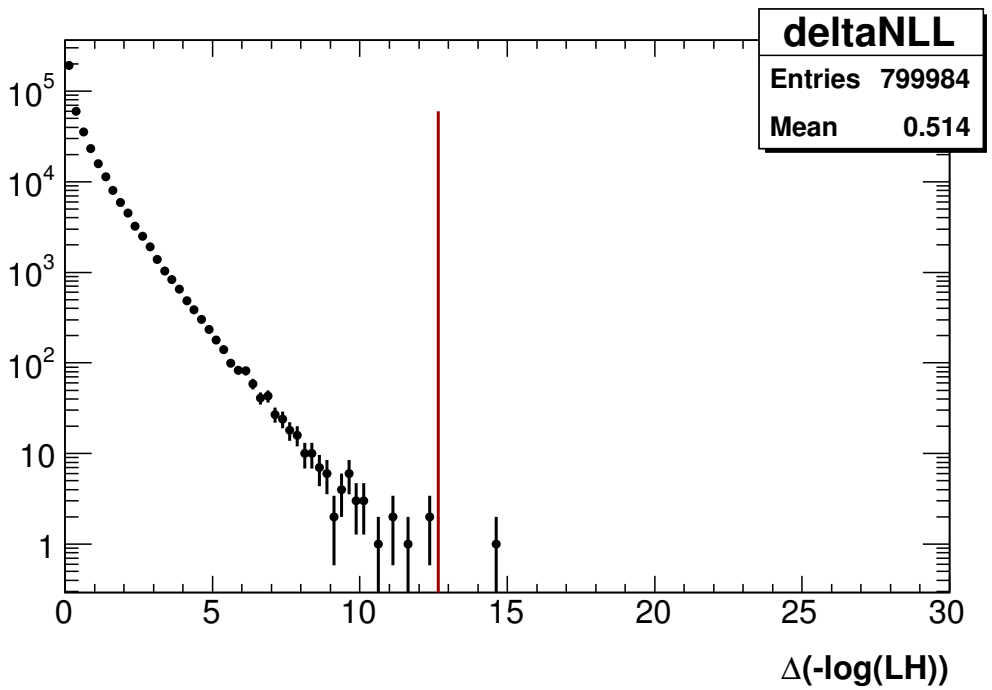

Figure 5.24: $-2\Delta(\log\mathcal{L})$ distribution for $Q = 21.25\,\mathrm{MeV}/c$, fixed to the LHCb measurement value.

Chapter 6

Systematic Error Analysis

6.1 Systematic Uncertainties

The systematic uncertainties considered in the analysis are the following:

- The uncertainty due to the CDF tracker momentum scale.
- The uncertainty due to the resolution model (see Sec. 5.10) described by the sum of two Gaussians.
- The choice of background model.

6.1.1 Momentum Scale

To estimate the uncertainty due to the momentum scale, a D^{*+} signal is taken as a calibration, both from MC and data. Table 6.1 shows several D^{*+} and charm baryon resonances measured with CDF and compared with the PDG [26] values. The mass difference between the D^{*} measured by CDF and that reported by the PDG amounts

Mass difference	CDF	PDG [26]
$M(D^{*+}) - M(D^0)$	145.477 ± 0.002	145.421 ± 0.010
$M(\Sigma_c^0) - M(\Lambda_c^+)$	167.28 ± 0.12	167.30 ± 0.11
$M(\Sigma_c^{++}) - M(\Lambda_c^+)$	167.44 ± 0.13	167.56 ± 0.11
$M(\Lambda_c(2625)^+) - M(\Lambda_c^+)$	341.65 ± 0.13	341.7 ± 0.6

Table 6.1: The CDF II and PDG [26] mass differences used to estimate the systematic error due to the mass scale uncertainty. The quoted $\Sigma_c^0, \Sigma_c^{++}$ values in the first column are taken from the best CDF II measurement [63], while the D^{*+} mass value quoted corresponds to the analysis and measurement for D^{*+} masses with $p_T > 200\,\text{MeV}/c$ from [51]. All the masses are in units of MeV/c^2.

to $0.056\,\text{MeV}/c^2$. In this case the uncertainties on the measured mass difference or Q value are due to the momentum scale of the low p_T π_s tracks.

Using the D^{*+} signal, the soft pion $p_\text{T}(\pi^+)$ is scaled by a factor α to get the PDG quoted value. The scale factor α will be used to propagate the uncertainty into the Q value scale of the $\Lambda_b^{*0} \to \Lambda_b^0 \pi_s^- \pi_s^+$ system. The plots in Figure 6.1 show the CDF experimental data for the D^{*+} and D^{*-} signals reconstructed separately for different charge states. The soft pion momentum $p_\text{T}(\pi_s^+)$ and the track quality criteria are the same as for the daughters of Λ_b^{*0} candidates.

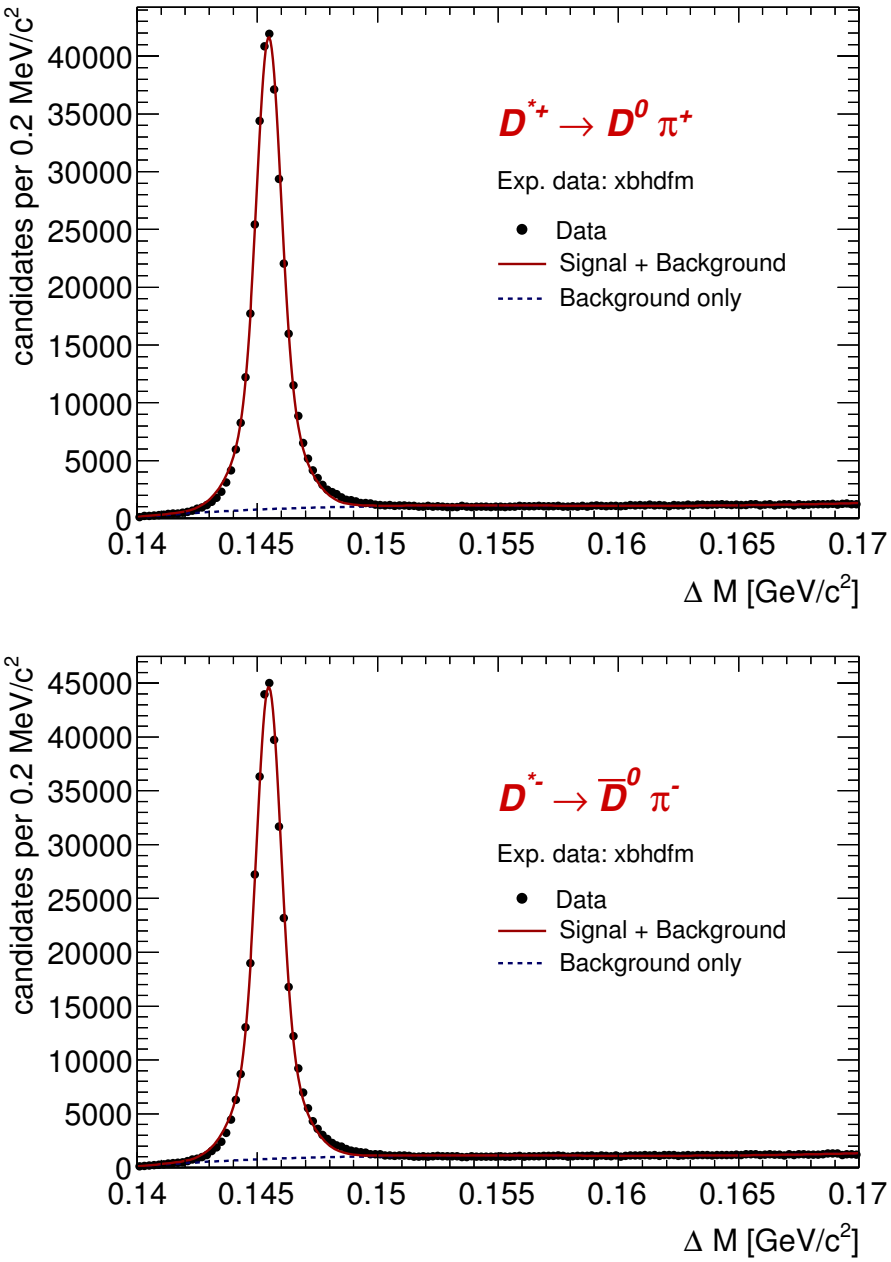

Figure 6.1: The mass differences $M(D^0\pi^+) - M(D^0)$ and $M(\bar{D}^0\pi^-) - M(\bar{D}^0)$ are shown in the upper and lower plot respectively.

Charged State	ΔM, MeV/c^2	σ_n, MeV/c^2	g_n, fraction	σ_w, MeV/c^2
D^{*+}	145.478 ± 0.001	0.478 ± 0.003	0.613 ± 0.007	1.14 ± 0.01
D^{*-}	145.476 ± 0.001	0.475 ± 0.003	0.615 ± 0.006	1.14 ± 0.01

Table 6.2: The results of the fits of two separate charge states, D^{*+} and D^{*-}.

The experimental D^{*+} and D^{*-} spectra are subjected to unbinned Maximum Likelihood fits with double Gaussians convolved with the Breit-Wigner function (two Voigtian functions). The natural width of the $D^{*\pm}$ is fixed to $\Gamma = 0.096\,\mathrm{MeV}/c^2$ [26]. The background is described by the `RooDSTD0BG` function provided by `RooFit` and developed mostly for the fits of the D^{*+} background shape. The results of the fits are listed in Table 6.2.

The difference in masses of different charge states is negligible:

$$\Delta M(D^{*+}) - \Delta M(D^{*-}) = (0.002 \pm 0.002)\,\mathrm{MeV}/c^2\,.$$

There is no charge asymmetry due to soft pions. We apply the multiplicative factor α to $p_\mathrm{T}(\pi_s)$ to adjust the CDF to PDG mass difference of $0.056\,\mathrm{MeV}/c^2$. The MC data plots in Figure 6.2 show the development of the MC D^{*+} peak position for several scale factors α applied to $p_\mathrm{T}(\pi_s^+)$.

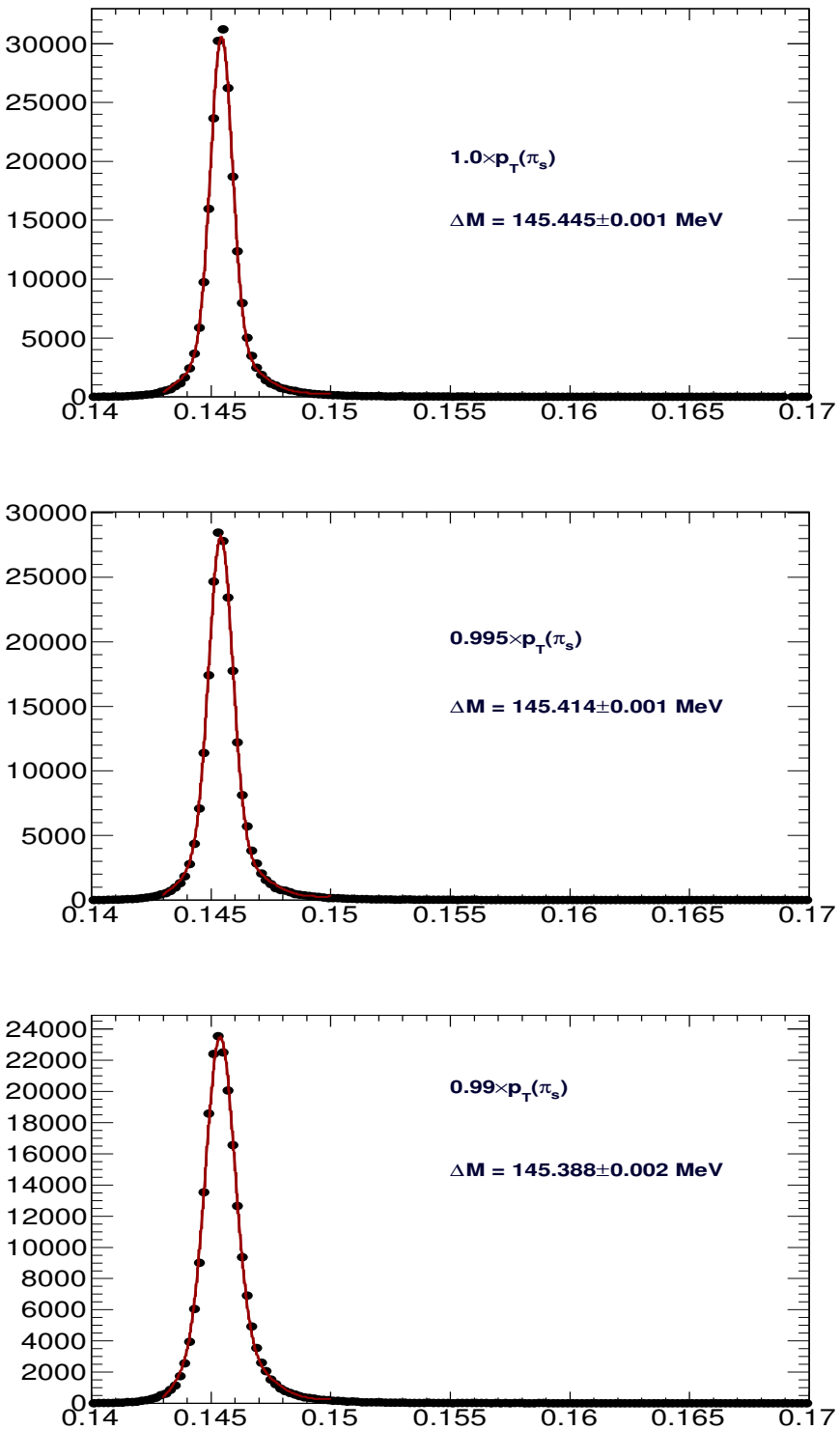

Figure 6.2: The MC D^{*+}plots with the scale factors $\alpha = 1.0, 0.995$, and 0.99.

Scale factor, $\alpha \cdot p_{\mathrm{T}}(\pi_s)$	ΔM, MeV/c^2	$\delta(\Delta M)$ MeV/c^2
1.0	145.445 ± 0.001	0.0
0.995	145.414 ± 0.001	0.031
0.99	145.388 ± 0.002	0.057
0.987	145.373 ± 0.002	0.072
0.985	145.361 ± 0.002	0.084

Table 6.3: The adjustment of the CDF data to the PDG mass difference for the D^{*+} with various scale factors.

The spectra in Figure 6.2 are fitted within the same range. The shift of the peak position with respect to the one with $\alpha = 1.0$ is presented in Table 6.3. One can see that the scale factor $\alpha = 0.99$ reduces the $p_{\mathrm{T}}(\pi_s^+)$ momentum scale by 1% and adjusts the CDF D^{*+} scale by the needed amount.

The plots in Figure 6.3 show the MC soft pion spectra for the soft pions from the D^{*+} and for both soft pions from the Λ_b^{*0}. The soft pion spectrum from the Λ_b^{*0} is slightly softer than the ones originating from the D^{*+}. Taking the relative measure of the softness of the Λ_b^{*0} soft pions with respect to the D^{*+} ones as the ratio of mean p_{T} values,

$$< p_{\mathrm{T}}(\pi_s, \Lambda_b^{*0}) > / < p_{\mathrm{T}}(\pi_s, D^{*+}) >= 0.43/0.55\,,$$

we can reduce the 1% adjustment of the D^{*+} soft pions by this ratio, $0.01 \cdot \frac{0.43}{0.55} = 0.0078$, and apply to the Λ_b^{*0} soft pions the factor $1.0 - 0.0078 \approx 0.992$.

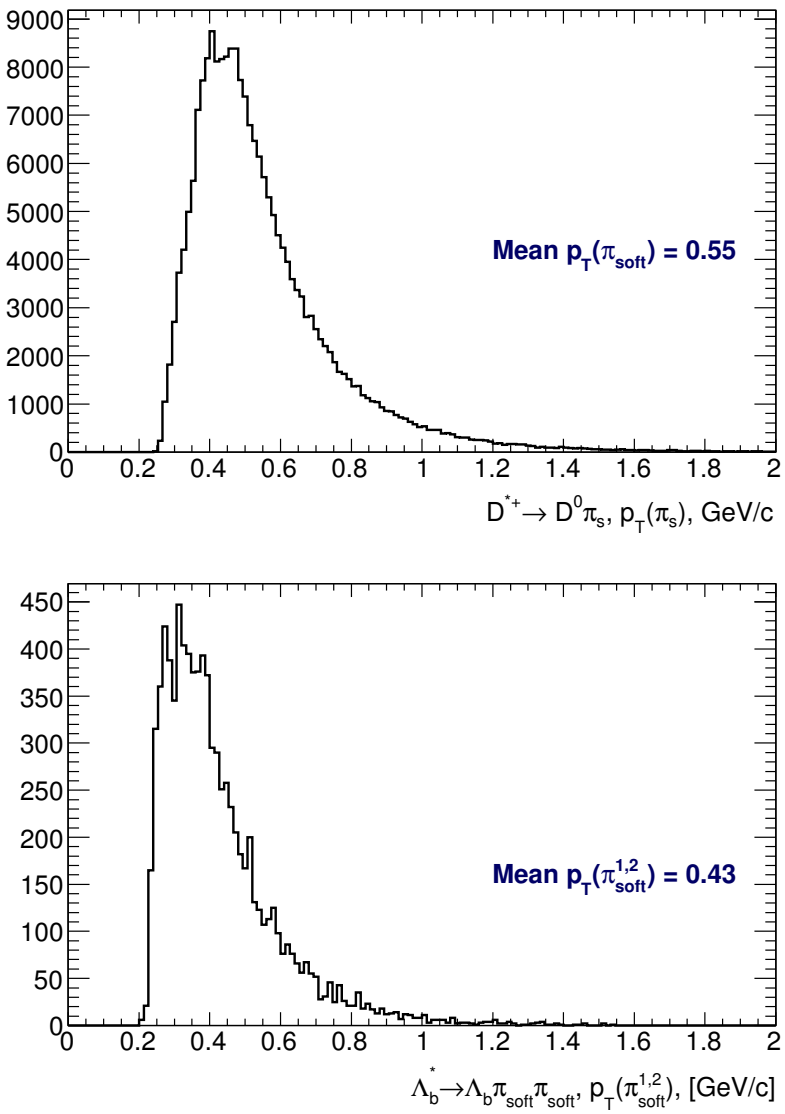

Figure 6.3: The p_{T} spectra of the soft pions from D^{*+} and Λ_b^{*0}.

The plots in Figure 6.4 show the development of the MC Λ_b^{*0} peak position for several scale factors α applied to $p_{\mathrm{T}}(\pi_s^+)$ and corresponding to the ones applied to D^{*+}. The spectra in Figure 6.4 are fitted with a double Gaussian, and the shift of

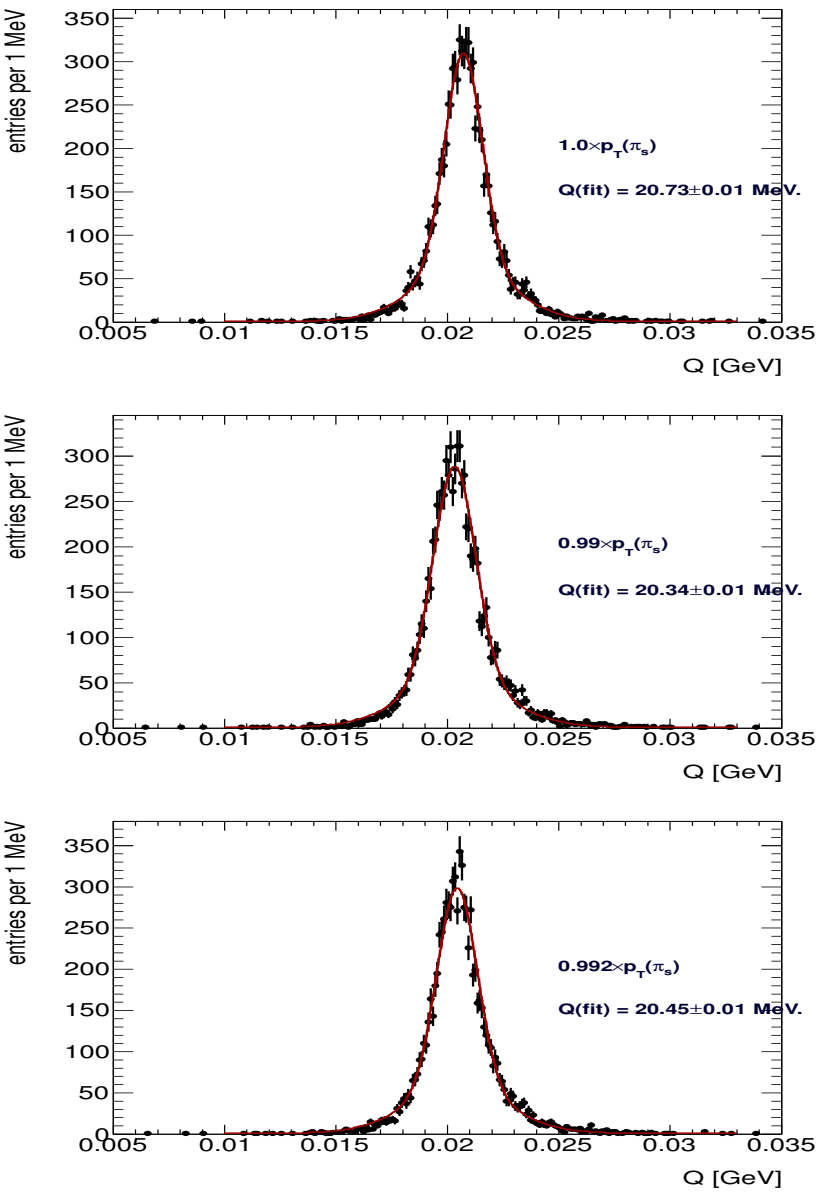

Figure 6.4: The MC Λ_b^{*0} plots with the scale factors $\alpha = 1.0, 0.995$, and 0.992.

Scale factor, α	Q, MeV/c^2	$\delta(Q)$ MeV/c^2
1.0	20.73 ± 0.01	0.0
0.995	20.53 ± 0.01	0.20 ± 0.02
0.992	20.45 ± 0.01	0.28 ± 0.02
0.99	20.34 ± 0.01	0.39 ± 0.02

Table 6.4: The shift of the $\Lambda_b^{*0}Q$-value in MC data with various scale factors applied to both soft pions.

the Λ_b^{*0} peak position with respect to the one with $\alpha = 1.0$ is presented in Table 6.4. With the scale factor 0.992, the Λ_b^{*0} mass moves by $-0.28\,\mathrm{MeV}/c^2$. The central value of the Λ_b^{*0} fitted Q value is corrected by this shift with a 100% uncertainty, i.e., the correction found using the calibration D^{*+} signal will be $(-0.28 \pm 0.28)\,\mathrm{MeV}/c^2$, contributing to the momentum scale uncertainty.

6.1.2 Signal Model

The CDF Monte Carlo simulation typically underestimates the $D^{*\pm}$ resolutions in the experimental data: $\sigma_n(\text{data}) \lesssim 1.25\,\sigma_n(\text{Monte Carlo})$. Similar relations are found for the broad component of the resolution: $\sigma_w(\text{data}) \lesssim 1.40\,\sigma_w(\text{Monte Carlo})$. These factors are used the sources of the systematic uncertainties, see [51] and [57].

Taking a conservative approach, the corresponding Gaussian widths are adjusted as 100% correlated by

$$\sigma_n(\text{Monte Carlo}) = \sigma_n(\text{Monte Carlo}) + 0.25 \cdot \sigma_n(\text{Monte Carlo})$$

and

$$\sigma_w(\text{Monte Carlo}) = \sigma_w(\text{Monte Carlo}) + 0.40 \cdot \sigma_w(\text{Monte Carlo})$$

The σ_n, σ_w and fraction of the narrow core g_n have statistical uncertainties due to the finite size of the Λ_b^{*0} MC sample used to extract these parameters. We examine the case in which

$$\sigma_n(\text{Monte Carlo}) = \sigma_n(\text{Monte Carlo}) \pm \delta_{\text{stat}}(\sigma_n(\text{Monte Carlo}))$$

$$\sigma_w(\text{Monte Carlo}) = \sigma_w(\text{Monte Carlo}) \pm \delta_{\text{stat}}(\sigma_w(\text{Monte Carlo}))$$

and

$$g_n(\text{Monte Carlo}) = g_n(\text{Monte Carlo}) \pm \delta_{\text{stat}}(g_n(\text{Monte Carlo})).$$

The signal spectrum is refitted with the adjusted resolutions. The difference in the fit result for the Q value is taken as the systematic uncertainty.

The case is also considered in which the signal model is changed as the ratio of widths is fixed while the narrow one is left floating. This case introduces another systematic due to the signal model. This uncertainty is listed in Table 6.5 with value $\pm$ 0.11 MeV/c^2.

6.1.3 Background Shape

To find the systematic uncertainty associated with the choice of background shape, the background PDF is replaced by third and fourth order Chebyshev polynomials, and then compared with the default one.

6.1.4 Summary of Uncertainties

The uncertainties are summarized in Table 6.5.

The uncertainty due to the momentum scale of the soft pions is the largest one. The uncertainties are added and the central value of the fitted Q-value of the signal is adjusted, specifically $Q = (20.68 \pm 0.35(\text{stat}) \pm 0.30(\text{syst}))$ MeV/c^2.

Source	**Value**, MeV/c^2	Comment
Momentum scale	-0.28 ± 0.28	propagated from D^{*+} sample
MC σ_n, σ_w predictions	-0.07	MC underestimates resolution
MC σ_n, σ_w stat. uncertainty	± 0.011	change by ± 1(stat)
MC g_n stat. uncertainty	± 0.004	change by ± 1(stat)
Signal model	± 0.11	use case with fixed width ratio
Background model	± 0.03	consider 3-rd, 4-th power Chebyshev polynomials
Total:	-0.28 ± 0.30	added in quadrature

Table 6.5: Summary of systematic uncertainties.

6.2 Efficiency Estimates for various Mass Difference Values Q

In this section we describe the MC study aimed at estimating the acceptances and efficiencies for several Q-value points. The goal is to understand the relative efficiencies at several Q-values. Particularly we are interested in the relative efficiencies of $Q = 10.0\,\mathrm{MeV}/c^2$ and our default $Q = 20.66\,\mathrm{MeV}/c^2$ as these two mass differences corresponds to excited states of Λ_b^0. These relative efficiencies would also support to illustrate the lack of a $\Lambda_b^{*0}(5912)$ signal in the CDF data in comparison with the $\Lambda_b^{*0}(5912)$ yield reported by the LHCb. The MC data are generated, simulated, reconstructed, ntuplized and analyzed in the same way as is described in Section 5.10, *i.e.*, the analysis cuts are applied to plot the distributions of the detector response.

Figure 6.5 shows the shape of the CDF detector response for the Λ_{b1}^{*0} state corresponding to $Q = 10.0\,\mathrm{MeV}/c^2$ or $M = 5909.34\,\mathrm{MeV}/c^2$, to $Q = 15.0\,\mathrm{MeV}/c^2$ or $M = 5914.34\,\mathrm{MeV}/c^2$, and to $Q = 20.66\,\mathrm{MeV}/c^2$ or $M = 5920.00\,\mathrm{MeV}/c^2$. The distributions are again fitted with a sum of double Gaussian functions as in Section 5.10.

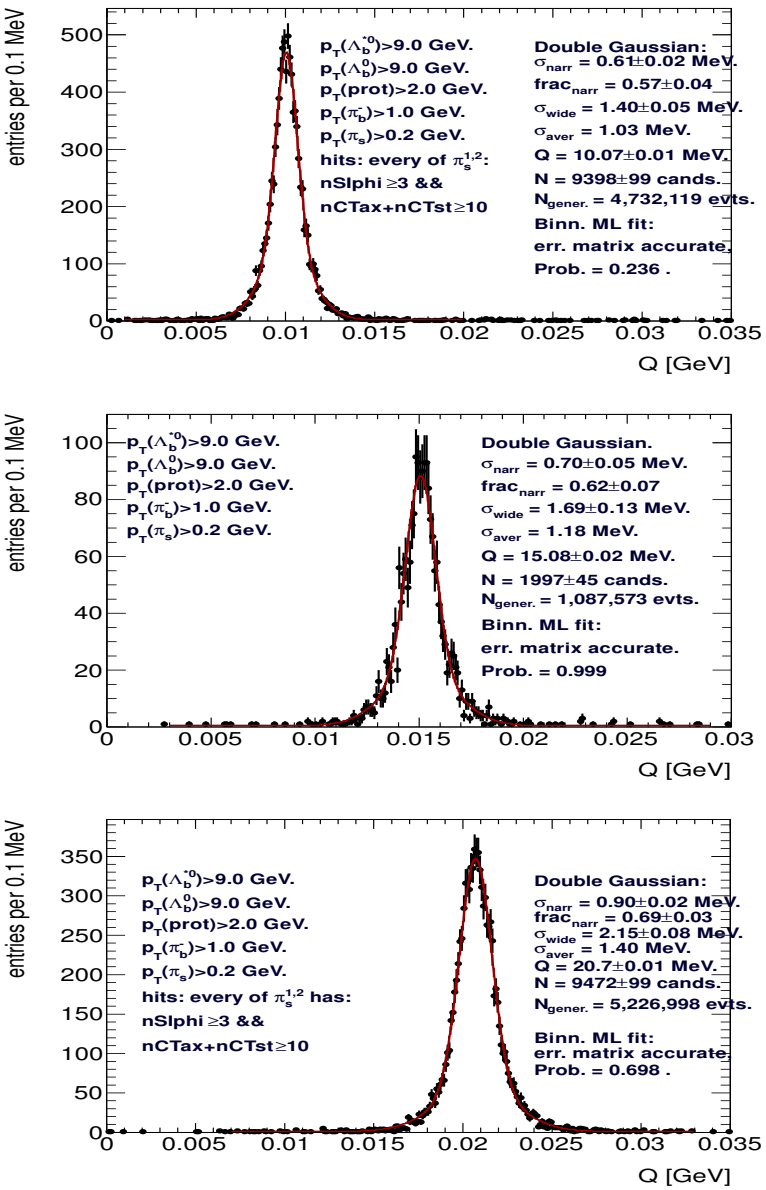

Figure 6.5: The response of the CDF detector to the Λ_b^{*0} signals after the modes generated with zero natural width, $\Lambda_b^{*0} \to \Lambda_b^0 \pi_s^+ \pi_s^-$, are simulated, reconstructed and ntuplized. The analysis cuts are applied. The soft pion tracks are required to have hits in SVX II, $N(\text{SVX II}) \geq 3$ and $(N_{\text{ax}} + N_{\text{st}})(\text{COT}) \geq 10$. The Q-value spectrum, where $Q = M(\Lambda_b^0 \pi_s^+ \pi_s^-) - M(\Lambda_b^0) - 2 \cdot m_\pi$, is subjected to a fit with a double Gaussian: both widths and relative weight are floating. The upper plots corresponds to a MC data sample produced for $Q = 10.0\,\text{MeV}/c^2$ or $M = 5909.34\,\text{MeV}/c^2$, the middle plot is for $Q = 15.0\,\text{MeV}/c^2$ or $M = 5914.34\,\text{MeV}/c^2$, and the bottom one is for $Q = 20.66\,\text{MeV}/c^2$ or $M = 5920.00\,\text{MeV}/c^2$.

Q, MeV/c^2	N gen.	N filt.	Acceptance, $\mathcal{A}$	N CDF reco.	N fitted	Reconstr. eff. $\mathrm{Eff}_{\mathrm{reco.}}(10^{-3})$
10	8936091	4859633	0.5438 ± 0.0002	4732119	9397	(1.99 ± 0.02)
15	2599753	1526299	0.5871 ± 0.0003	1087604	1997	(1.84 ± 0.04)
20	7910582	4949285	0.6257 ± 0.0002	5226998	9472	(1.81 ± 0.02)

Table 6.6: Estimates of the acceptances and reconstruction efficiencies for $Q = 10, 15$, and $20.66\,\mathrm{MeV}/c^2$. The calculations are based on the full CDF Monte-Carlo simulation. The statistical errors for acceptances and efficiencies are calculated as $\delta\mathrm{Eff} = \sqrt{\mathrm{Eff} \cdot (1 - \mathrm{Eff})/N_{orig}}$.

The results of the fits for all three Q-value points are listed in Table 6.6. We use the resolution model fitted to MC data where the soft pion momentum $p_{\mathrm{T}}(\pi_s) > 0.2\,\mathrm{GeV}/c^2$.

The soft pion tracks are required to have hits given by $N_{r-\phi}(\mathrm{SVX\ II}) \geq 3$ and $(N_{\mathrm{ax}} + N_{\mathrm{st}})(\mathrm{COT}) \geq 10$. The analysis cuts are applied to the reconstructed candidates. The following definitions are required for the filter acceptance and efficiency of the finally reconstructed and fitted candidates:

$$\mathcal{A} = N_{\mathrm{filt.}}(p_{\mathrm{T}}(\pi_s^{\pm}) > 150\,\mathrm{MeV}/c)/N_{\mathrm{gen.}}$$

$$\mathrm{Eff}_{\mathrm{reco.}} = N_{\mathrm{fitted}}/N_{\mathrm{CDF\,reco.}}$$

The resulting full efficiencies $\varepsilon = \mathcal{A} \cdot \mathrm{Eff}_{\mathrm{reco.}}$ for every Q-value are calculated as a product of the acceptance of `HepgFilter` applied to the soft pions, $p_{\mathrm{T}}(\pi_s^{\pm}) > 0.150\,\mathrm{GeV}/c$, and of the reconstruction efficiency $\mathrm{Eff}_{\mathrm{reco.}}$, see Table 6.7. The simulated trigger efficiency is included in $\mathrm{Eff}_{\mathrm{reco.}}$.

Table 6.8 shows the resolution for every Q-value based on a double Gaussian resolution model, see Figure 6.5. The average resolution is calculated based on the total variance, *i.e.*,

$$\sigma_{aver}^2 = \sigma_n^2 \cdot g_n + \sigma_w^2 \cdot (1 - g_n)\,.$$

Q, MeV/c^2	$\varepsilon = \mathcal{A} \cdot \mathrm{Eff}_{\mathrm{reco.}}$
$Q = 10$	$(1.08 \pm 0.01) \cdot 10^{-3}$
$Q = 15$	$(1.08 \pm 0.02) \cdot 10^{-3}$
$Q = 20$	$(1.13 \pm 0.01) \cdot 10^{-3}$

Table 6.7: Estimates of the full efficiencies for values $Q = 10, 15$, and 20.66 MeV/c^2. The statistical errors on $\mathcal{A}$ and $\mathrm{Eff}_{\mathrm{reco.}}$ are added in quadrature.

The average resolution gradually increases with the Q-value, as expected.

Q, MeV/c^2	σ_n, MeV/c^2	σ_w, MeV/c^2	fraction, g_n	σ_{aver}, MeV/c^2
$Q = 10$	(0.61 ± 0.03)	(1.40 ± 0.05)	(0.57 ± 0.04)	≈ 1.03
$Q = 15$	(0.70 ± 0.05)	(1.69 ± 0.13)	(0.62 ± 0.07)	≈ 1.18
$Q = 20$	(0.90 ± 0.02)	(2.15 ± 0.08)	(0.69 ± 0.03)	≈ 1.40

Table 6.8: The parameters of the double Gaussian resolution model for values $Q = 10, 15$, and 20.66 MeV/c^2.

6.2.1 Expectation for the Signal of the $\Lambda_b^{*0}(5912)$

The LHCb Collaboration has recently published their observation of $\Lambda_b^{*0}(5912)$ and $\Lambda_b^{*0}(5920)$ signals [44]. The LHCb and CDF results are summarized in Table 6.9. To estimate the possible yield in the CDF detector, we normalize the measured CDF yield for the $\Lambda_b^{*0}(5920)$ using the ratio of the yields of the $\Lambda_b^{*0}(5912)$ and the $\Lambda_b^{*0}(5920)$ measured in LHCb detector, specifically:

$$\begin{aligned} N(\Lambda_b^{*0}(5912))^{\mathrm{expect.}}_{\mathrm{CDF}} =& (N(\Lambda_b^{*0}(5912))_{\mathrm{LHCb}} / N(\Lambda_b^{*0}(5920))_{\mathrm{LHCb}}) \\ &\times (\varepsilon(Q = 10\,\mathrm{MeV}/c^2)_{\mathrm{CDF}} / \varepsilon(Q = 20\,\mathrm{MeV}/c^2)_{\mathrm{CDF}}) \\ &\times N(\Lambda_b^{*0}(5920))_{\mathrm{CDF}} \end{aligned}$$

The ratio of efficiencies in the CDF detector is taken from Table 6.7. The normalization to LHCb results uses the assumptions:

Experim.	State	$Q_{meas.}$, MeV/c^2	Yield, N_{cands}
LHCb [44]	$\Lambda_b^{*0}(5912)$	$13.46 \pm 0.12(\text{stat}) \pm 0.04(\text{syst})$	$17.6 \pm 4.8(\text{stat})$
LHCb [44]	$\Lambda_b^{*0}(5920)$	$21.26 \pm 0.08(\text{stat}) \pm 0.04(\text{syst})$	$52.5 \pm 8.1(\text{stat})$
CDF	$\Lambda_b^{*0}(5920)$	$20.68 \pm 0.35(\text{stat}) \pm 0.30(\text{syst})$	$52.5 \pm 8.1(\text{stat})$
CDF counts	$\Lambda_b^{*0}(5912)$	$(10.66, 16.82)$	3.0 (3.22, fitted)

Table 6.9: The LHCb and CDF results on the $\Lambda_b^{*0}(5912)$ and $\Lambda_b^{*0}(5920)$ signals. The last line shows the number of counted and fitted candidates in the $(13.46 + 0.28 \pm 3\sigma_{\text{aver}})$ MeV/c^2 range at the expected $\Lambda_b^{*0}(5912)$ signal position in the CDF detector.

(i) The CDF simulation is *right* for soft tracks (below 400 MeV/c)

(ii) $\varepsilon(Q = 10\,\text{MeV}/c^2)_{\text{LHCb}}/\varepsilon(Q = 20\,\text{MeV}/c^2)_{\text{LHCb}} = 1.0$

(iii) $\sigma_{prod}(J^P = \frac{1}{2}^-) \,/\, \sigma_{prod}(J^P = \frac{3}{2}^-)$ is, for Λ_b^{*0} states, the same in LHCb and in CDF.

The expected number of $\Lambda_b^{*0}(5912)$ candidates is found to be $N(\Lambda_b^{*0}(5912))^{\text{expect.}}_{\text{CDF}} = 5.5 \pm 2.4$. The assumptions (i) and (iii) are weak.

6.2.2 p-Values

Based on the LHCb measurements (see Table 6.9 and Table 6.8), we set the Q-value range in the CDF spectrum to be $(13.46 + 0.28(\text{scale offset}) \pm 3 \cdot \sigma_{\text{aver}})$ MeV/c^2 or $(10.66, 16.82)$ MeV/c^2. The range is shown with dashed lines in Figure 6.6.

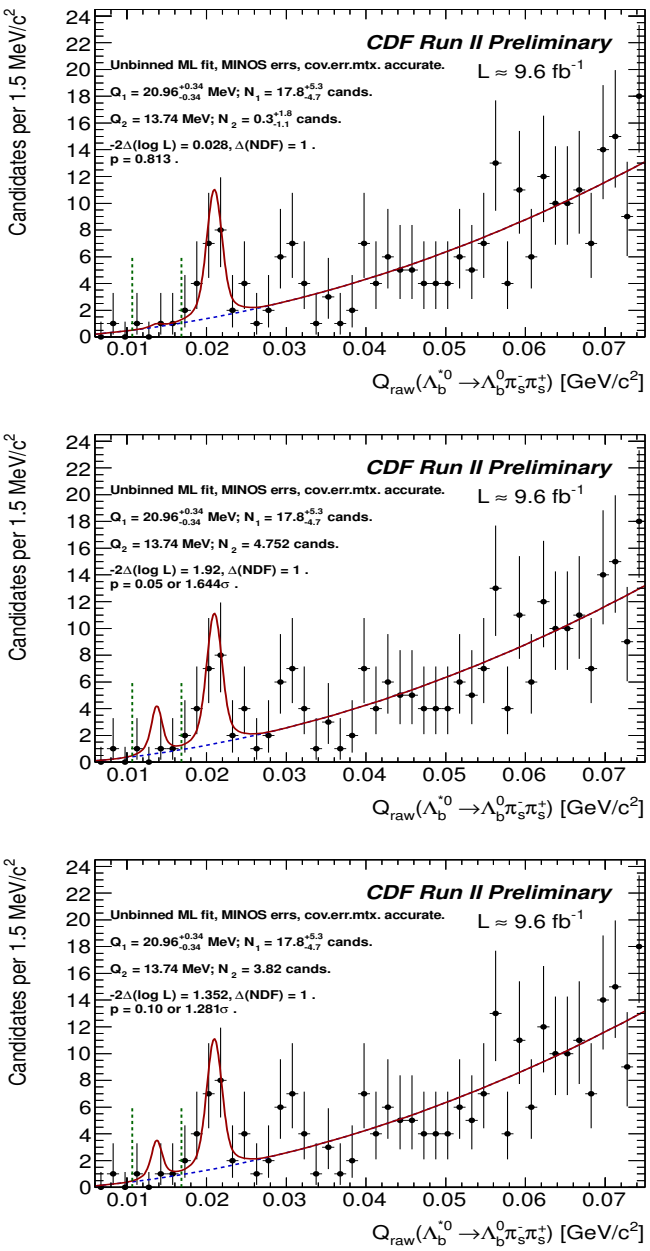

Figure 6.6: The expected $\Lambda_b^{*0}(5912)$ range of $(10.66, 16.82)\,\mathrm{MeV}/c^2$ is shown with green dashed lines at the CDF Q-value spectrum. The unbinned maximum likelihood fits with double peak model are shown, and the second (non-default) peak position $Q = 13.74\,\mathrm{MeV}/c^2$ is fixed in the fits. Top to bottom plots: the yields are floating for both peaks; the yields are set to values corresponding to 95% C.L., $N_2 = 4.752$; to 90% C.L., $N_2 = 3.82$.

Yield	p-value	C.L.	N_σ
5.5	0.026	0.972	≈ 1.94
$5.5 - 2.4$	0.125	0.831	≈ 1.15
$5.5 + 2.4$	0.0045	0.9957	≈ 2.6

Table 6.10: The p-value estimates based on Poissonian counting.

Integrating the background normalized to data within $Q \in (10.66, 16.82)\,\mathrm{MeV}/c^2$, we estimate the number of background candidates under the expected $\Lambda_b^{*0}(5912)$ signal to be 3.22. The actual candidate count within the same range is 3.0 candidates, see Table 6.9.

The p-values are calculated likelihood that the expected signal of 5.5 ± 2.4 candidates on top of 3.2 background will fluctuate down to $n \leq 3$ candidates, given Poisson statistics.
The code for this is:

5.5 candidates on top of 3.2 background fluctuates to 3, 2, and 1 entries

```
double prob  = TMath::PoissonI(3.0, 5.5 +3.2);
    prob += TMath::PoissonI(2.0, 5.5 +3.2);
    prob += TMath::PoissonI(1.0, 5.5 +3.2);
```

p($N \leq 3$) = 0.026037, $N_\sigma = 1.94$

See Table 6.10 for a summary of the p-values.

The unbinned Maximum Likelihood fits are shown in Figure 6.6. The likelihood ratio of the two-peak hypothesis is the default one. The single peak hypothesis is used to find the 90% C.L. and 95% C.L. probabilities for observing a signal of the $\Lambda_b^{*0}(5912)$ in the CDF detector. The double Gaussian resolution for the $\Lambda_b^{*0}(5912)$ signal is set according to Table 6.8. The p-value is calculated with TMath::Prob(2.0*TMath::Abs(deltaNLL), deltaNDF).

Yield	$-2 \cdot \Delta(\ln \mathcal{L})$	Δ(NDF)	p-value	C.L.	N_σ
5.5	2.404	1	0.028	0.972	≈ 1.9
$5.5 - 2.4$	0.948	1	0.169	0.831	≈ 1.0
$5.5 + 2.4$	4.082	1	0.0043	0.9957	≈ 2.6
4.752	1.92	1	0.05	0.95	≈ 1.644
3.82	1.352	1	0.10	0.90	≈ 1.281

Table 6.11: The p-value estimates using the likelihood ratio of unbinned maximum likelihood (ML) fits. The last two rows contain 95% C.L. and 90% C.L. upper limits respectively, see also Figure 6.6. With the $Q = 13.74\,\text{MeV}/c^2$ fixed in the maximum likelihood fit for the two signal hypothesis, the difference in the number of degrees of freedom, $\Delta(\text{NDF}) = 6 - 5$.

The inverse function 0.5*TMath::ChisquareQuantile(1.0-pValue, deltaNDF) is used to calculate the corresponding two peak $-\ln \mathcal{L}$ with respect to the default, single peak $-\ln \mathcal{L}$. The $-\ln \mathcal{L}$ curve has been scanned versus yield to find the corresponding value.

We consider a "one side discovery" p-value and calculate the equivalent number of Gaussian σ as `TMath::ErfcInverse(2.*pValue)*(TMath::Sqrt(2.))`, i.e. the value of $p = (1 - 0.6827)/2$ corresponds to 1σ in this normalization. The fit results with upper limits at 95% C.L. and 90% C.L. are summarized in Table 6.11. The results in Tables 6.10 and 6.11 are consistent.

6.2.3 Conclusion of the Study

The expected signal size of the $\Lambda_b^{*0}(5912)$ is estimated for CDF data based on the observations made by LHCb and on the model conjectures made. The expected CDF yield of 5.5 candidates at $Q = 13.46\,\text{MeV}/c$ is $\lesssim (1.9\sigma)$ (Gaussian) away from the actual 3 candidates found in the Q-value range of interest. The unbinned ML fit analysis of the experimental Q-value spectrum shown in Figure 6.6 results in

upper limits on the $\Lambda_b^{*0}(5912)$ signal at 4.8 candidates at 95% C.L. (1.64σ) and 3.8 candidates at 90% C.L. (1.28σ).

6.3 Summary

A search for Λ_b^{*0} resonances has been performed. The Λ_b^{*0} resonance state in the Q value spectra, specifically

$$Q = 20.68 \pm 0.35(\text{stat}) \pm 0.30(\text{syst}) \text{ MeV}/c^2,$$

has been observed.

The significance of the signal for the search window of $(0, 50)\,\text{MeV}/c^2$ is 3.5σ. In terms of the mass difference, the signal is observed at

$$\Delta M = 299.82 \pm 0.35(\text{stat}) \pm 0.30(\text{syst}) \text{ MeV}/c^2.$$

We use the world-average Λ_b^0 mass value [22], $m(\Lambda_b^0) = 5619.4 \pm 0.7$ MeV/c^2 , which is dominated by the CDF [64] result and by the latest LHCb measurements [65]. We quote the absolute mass of the observed state to be:

$$M(\Lambda_b^{*0}) = 5919.22 \pm 0.35\,(\text{stat}) \pm 0.76\,(\text{syst}) \text{ MeV}/c^2\,.$$

The result is consistent with some of the theoretical predictions and the measurement [44] recently reported by the LHCb Collaboration of the state $\Lambda_b^{*0}(5920)$.

The $\Lambda_b^{*0}(5912)$ claimed by LHCb is not observed. At the corresponding Q-value of 13.46 MeV/c, we set an upper limit of 4.8 (3.8) candidates at 95% (90%) C.L. Assuming similar relative production rates and relative efficiencies for the $\Lambda_b^{*0}(5912)$ and $\Lambda_b^{*0}(5920)$ states in the CDF II and LHCb detectors, the lack of a $\Lambda_b^{*0}(5912)$ signal in the CDF data is statistically consistent with the $\Lambda_b^{*0}(5912)$ yield reported by the LHCb.

Chapter 7

Irradiation of New Technologies with the Proton Beam at LANSCE

7.1 Motivation

The detectors used in a high energy physics experiment play an essential role in discovering new particles and measuring their physical properties. Future advanced hadron colliders will produce tremendous radiation fields. Silicon tracking systems like the one described in Chapter 3 are used to reconstruct charged particle trajectories that traverse the detector volume. Hence the understanding of interactions between the energetic particles and the tracker material is very crucial.

We irradiate novel silicon detector devices with 800 MeV protons with typical beam currents of 60-80 nA. The irradiation is carried out at the Los Alamos Neutron Science Center (LANSCE) facility [66] of Los Alamos National Laboratory (LANL). The experiments were carried out in the Blue Room or Target 2 facility at the Weapons Neutron Research (WNR) experimental area at LANSCE. We irradiate these devices for various periods of time depending upon the desired fluence and

uniformity of the dose. Some devices are irradiated to fluences up to $(1-10)\times10^{15}$ n_{eq}/cm^2. During and after the irradiation, information about the test beam profile and fluence is very important.

This chapter describes the measurement of the fluence by activation of aluminum foils and the beam profile measurement using an aluminum foil matrix technique. A High Purity Germanium (HPGe) gamma ray spectrometer is installed, calibrated, and used to measure the activity of the aluminum foils. The activity results of the aluminum foils provide the measurement of the fluence received by the irradiated silicon devices.

7.2 Measurement of Proton Fluence by Activation of Aluminum Foils

Aluminum foils are placed into the 800 MeV proton beam to be used as dosimeters. The aluminum foils have sizes approximately 1x2 cm^2, 1x1 cm^2, and 2x2 cm^2 depending on the size of the test sample with which they are associated. In the interaction of the aluminum with the proton beam p, the element ^{22}Na is produced. The ^{22}Na decays via $\beta^+ \sim 90.32\%$ of the time and via electron capture $\sim 9.62\%$ of the time to excited ^{22}Ne, which then decays with a half-life of 2.602 years. The excited ^{22}Ne de-excites by emitting a gamma ray of energy 1274.5 keV as shown in Figure 7.1. The positron annihilates with an electron in the source or the cladding and emits a gamma ray of 511 keV. The gamma energy spectrum is acquired at a distance of 11 cm with the gamma-ray spectrometer.

We measure the total activity of the foil to compute the fluence. The rate of accumulation is given by

$$^{27}Al \rightarrow^{22} Na \rightarrow^{22} Ne.$$

The rate of decay of ^{22}Na is given by

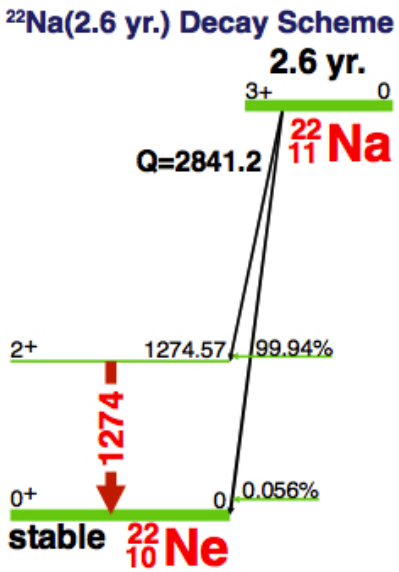

Figure 7.1: Decay spectra of the ^{22}Na, in keV.

$$\frac{dN(^{22}Na)}{dt} = \varphi N(^{27}Al)\sigma - \lambda N(^{22}Na),$$

where φ is the proton flux, σ is the total cross section for the production of ^{22}Na from proton-induced reactions on aluminum foil [67, 68], and λ is the decay constant that relates to the half-life $t_{1/2}$ as $\lambda = \frac{ln2}{t_{1/2}}$. We assume that $N(^{27}Al)$ is constant and given by

$$N(^{27}Al) = \frac{N_A \times P \times W}{M_A}$$

where N_A is Avogadro's number, P is the purity of the aluminum foil, W is the mass of the foil in grams, and M_A is the atomic mass of aluminum. We assume that $N(^{22}Na)(t = 0) = 0$, and we use aluminum with purity 99.5%. By solving the equation for these initial conditions, we obtain

$$N(^{22}Na) = \frac{\phi N(^{27}Al)\sigma(1 - e^{-\lambda t})}{\lambda}.$$

The activity A of the irradiated foil in the absence of the beam is given by

$$A = -\frac{dN(^{22}Na)}{dt} = \lambda N(^{22}Na).$$

The activity of a foil irradiated by protons for a period T and then measured after an elapsed time t_e is

$$A(t_e) = \varphi N(^{27}Al)\sigma(1 - e^{-\lambda T})e^{-\lambda t_e}.$$

Immediately after proton irradiation, $t_e = t_0 = 0$, and we can write

$$A(t_0) = \varphi N(^{27}Al)\sigma(1 - e^{-\lambda T}).$$

Hence the expression for the activity immediately after irradiation reduces to

$$A(t_e) = A(t_0)e^{-\lambda t_e}.$$

In our setup, the foil is left to decay for an elapsed time t_e and then measured for an interval of time $t_c = t_f - t_e$.

The average activity during the interval is given by

$$\overline{A(t_c)} = \frac{A(t_0)}{t_c}\int_{t_e}^{t_f} e^{-\lambda t}dt = \frac{A(t_e)}{\lambda t_c}(1 - e^{-\lambda t_c}).$$

Thus,

$$A(t_e) = \frac{\overline{A(t_c)}\lambda t_c}{(1 - e^{-\lambda t_c})}.$$

We measure $\overline{A(t_c)}$ and compute $A(t_e)$ and $A(t_0)$. Using

$$A(t_0) = \varphi N(^{27}Al)\sigma(1 - e^{-\lambda T}).$$

where t_0 is the time at the end of irradiation. We compute the flux

$$\phi = \frac{A(t_0)}{N(^{27}Al)\sigma(1 - e^{-\lambda T})} = \frac{A(t_e)e^{\lambda t_e}}{N(^{27}Al)\sigma(1 - e^{-\lambda T})}.$$

We then compute Φ, the proton fluence in protons/cm^2, through $\Phi = \phi T$.

7.3 Calibration of the Gamma Ray Spectrometer

We use an ORTEC GEM45P4-76-SMP gamma ray detector system and an ORTEC DSPEC-50 Multi Channel Analyzer (MCA) to collect these data in counts/unit time/channel. To calculate the activity at a particular energy, we need to convert these data into decays/unit time at a given energy. Our calibration source's spectrum ranges from 59.5 keV to 1836.1 keV and has eleven energy peaks distributed over this range. We also need the detection efficiency of the HPGe spectrometer's detector system as a function of energy. The efficiency of the detector system relates the number of gamma rays emitted from the source to the number of gamma rays collected in the full energy peak area.

7.3.1 Energy Calibrations

There are two energy calibration functions, (1) the energy vs. channel number, and (2) the peak shape (or FWHM) versus energy. The inputs to these functions are a spectrum or series of spectra with isolated peaks distributed over the energy range of interest, and an analysis gamma-ray library or table of peak energies. The formula for energy vs. channel number is

$$E(C) = a_1 + a_2 C + a_3 C^2$$

where E is the energy, the a_i are coefficients, and C is the channel number. We obtain these coefficients a_i by selecting the Auto Calibration option and fitting the energy spectrum of the calibration source with a quadratic polynomial. Figure 7.2 shows the fitted curve of calibrated energy versus channel number, for all 16383 channels. The coefficients obtained are a_1 =0.207 keV, a_2 = 0.207 keV/channel, and $a_3 = -3.914 \times 10^{-9}$ keV/channel^2.

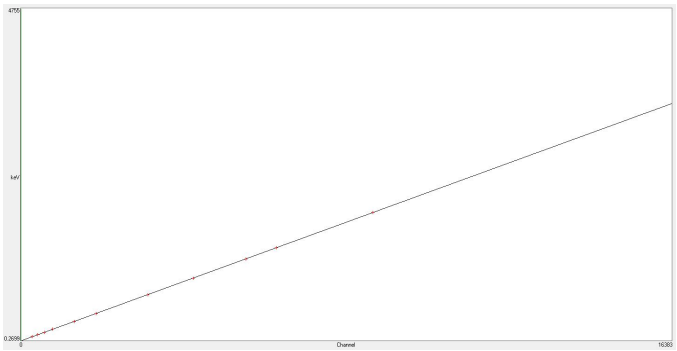

Figure 7.2: Calibration of energy versus channel number, captured as a screenshot from the ORTEC spectrometer.

The formula for FWHM versus channel number is

$$F(C) = b_1 + b_2 C + b_3 C^2$$

where F is FWHM in channels, the b_i are coefficients, and C is the channel number. To calculate the FWHM in energy, $F(E)$, we use the formula

$$F(E) = F(C)(a_2 + a_3 C)$$

where *F(C)* is FWHM in channels at channel C, C is channel number, and a_2 and a_3 are given as above. Calibration begins with collection of the spectrum of the calibration source with its isolated peaks. We use the Mixed Gamma Standard point source (peak energies are in keV, shown in the parentheses), which contains Am-241(59.54), Cd-109 (88.03), Co-57 (122.07), Ce-139 (165.85), Hg-203 (279.17), Sn-113 (391.69), Cs-137 (661.66), Y-88 (898.02), Co-60 (1173.24), Co-60 (1332.5), and Y-88 (1836.01). It has a gamma-ray emission rate of 3 microCi. We use the Auto Calibration mode, which performs a complete energy and FWHM calibration on the displayed spectrum using the working library. Auto Calibration searches for all the major peaks in the spectrum, and then this peak list is compared to the library peak list to find the calibration that gives the best match.

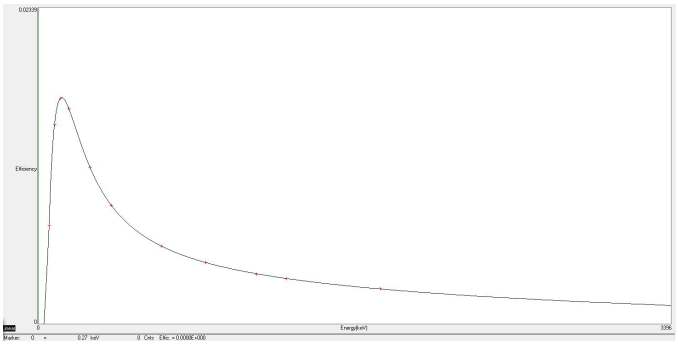

Figure 7.3: Calibration of efficiency versus energy, captured as a screenshot from the ORTEC spectrometer.

7.3.2 Efficiency Calibrations

The HPGe detector system efficiency includes effects from the detector itself, the detector source geometry, the materials surrounding the detector, and absorption in the source material. Efficiency is a function of energy, and our p-type germanium detector has a maximum efficiency at about 150 keV. To perform the efficiency calibration, we use the spectrum of the calibration radionuclides, the initial source strengths, and the calibration dates. These data are entered by the ORTEC custom software GammaVision-32. We use a 6-term polynomial to fit the natural logarithm of efficiency ϵ versus energy E:

$$\epsilon = e^{(\sum_{i=1}^{6} a_i E^{2-i})}.$$

The a_i are fitting coefficients. This function is optimized for a p-type detector. Figure 7.3 shows the fitted curve of calibrated efficiency versus energy for energies from 0 to 3396 keV. The coefficients a_i, in order of increasing index i, are -0.321305, -5.652440, 0.569694, -0.072035, 0.003970, and -0.000092 respectively. GammaVision-32 recalls the Calibration Certificate table (provided by Mixed Gamma Standard) of entries and performs a calibration based on the data in the nuclide calibration table,

and once the procedure is complete it displays the graph and calibration table.

7.4 Fluence Measurement Uncertainties

The primary sources of uncertainty on the measurement of proton fluence are the uncertainty in the measurement of the activity of ^{22}Na (σ_A); the uncertainty in the measurement of production cross-section of ^{22}Na (σ_C); the uncertainty in the measurement of mass of the Al foil (σ_W); the uncertainty in the measurement of dimensions of the Al foil (σ_D); and the uncertainty in the measurement of exposure counting time during the proton irradiation (σ_T).

7.4.1 Uncertainty in the Measurement of the Activity

The total uncertainty in the measurement of the activity is determined by summing in quadrature the individual uncertainties from the various analysis components.

These contributions are σ_{count}, the counting uncertainty; σ_{nor}, the normally distributed uncertainty; σ_{rsum}, the random summing uncertainty; σ_{abs}, the absorption uncertainty; σ_{nuc}, the nuclide uncertainty; σ_{eff}, the efficiency uncertainty; σ_{geo}, the geometry uncertainty; and σ_{uni}, the uniformly distributed uncertainty. All of the components of uncertainty are computed at the 1-sigma level and printed out in the activity report.

The counting uncertainty (σ_{count}), is given by σ_{GA}, the uncertainty in the gross area, and σ_{BA}, the uncertainty in the background area, added in quadrature:

$$\sigma_{count} = \sqrt{\sigma_{GA}^2 + \sigma_{BA}^2}.$$

The gross area error is given by the square root of the gross area. The background area error is given by the square root of ($\frac{Background\ area \times peak\ width}{Width\ of\ low\ average + Width\ of\ high\ average}$). The

Gamma Vision software calculates this uncertainty and shows it in the analysis report.

7.4.2 Estimation of Uncertainties

The estimated uncertainty in the measurement of the production cross-section of ^{22}Na is about 2.6%. A typical aluminum foil was weighed to ± 0.1 mg accuracy, and its contribution to the uncertainty in the measurement is less than 1%. The counting uncertainty is highly dependent on the amount of time the aluminum foil is measured by the gamma ray spectrometer. If the sample is counted for 10 minutes, the overall measurement uncertainty is on the order of 10%. If the sample is counted for 12 hours or longer, the overall uncertainty reduces to $2-3\%$. The dimensions of the foil were measured to the precision of ± 0.001 cm and contribute uncertainty to the measurement of about 0.5%. The uncertainty in the measurement of counting time is less than 0.1%.

7.5 Beam Profile Measurement using an Al Foil Matrix

The following serves as a confirmation of the diode array-based beam profile measurement which is described in the next chapter.

We insert transverse to the beam a 2x2 cm^2 aluminum foil segmented into sixteen individual squares and expose it to a fluence of approximately 4×10^{15} protons/cm^2. We then measure the activity of each individual square separately and infer the proton fluence received by it.

Figure 7.4 shows the resulting histogram of proton beam profile received by each

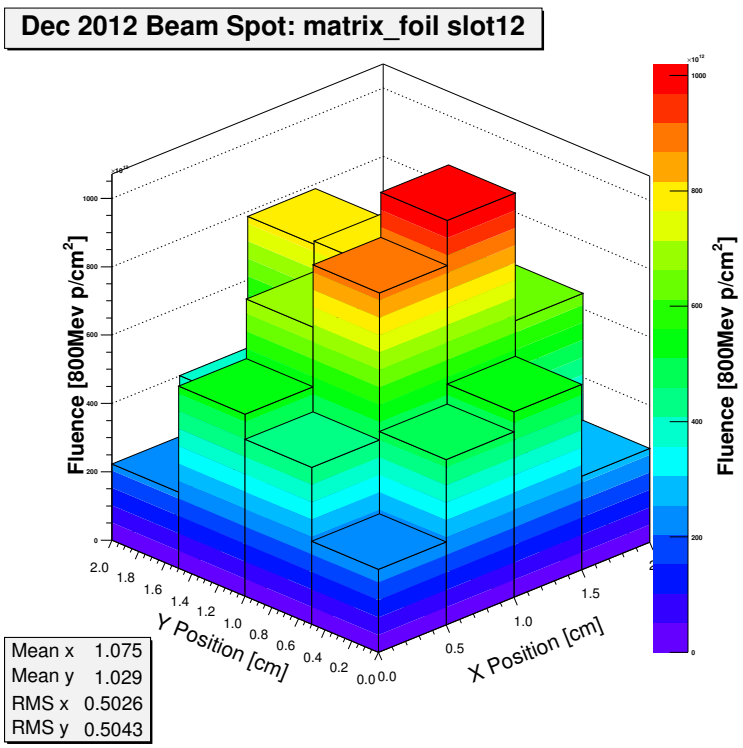

Figure 7.4: Proton beam profile in the XY plane as a function of proton fluence.

foil. The aluminum square centered on position (1.25 cm, 0.75 cm) received the maximum proton fluence and indicates the center of the beam spot. The beam intensity is distributed over an area of about 2 cm^2, and the hot beam spot is located within ∼0.5 cm^2. The maximum fluence received by the aluminum square is about 1.02×10^{15} protons/cm^2 and its total uncertainty in measurement is less than 1.5%.

Chapter 8

A Method for Real Time Monitoring of Proton Beam Profile and Fluence

8.1 Overview

Detectors planned for use at the Large Hadron Collider will operate in a radiation field produced by beam collisions. To predict the radiation damage to the components of the detectors, prototype devices are irradiated at test beam facilities that reproduce the radiation conditions expected. The profile of the test beam and the fluence applied per unit time must be known. Techniques such as thin metal foil activation and radiographic image analysis have been used to measure these; however, some of these techniques do not operate in real time, have low sensitivity, or have large uncertainties. We have developed a technique to monitor in real time the beam profile and fluence using an array of $p-i-n$ semiconductor diodes whose forward voltage is linear with fluence over the fluence regime [69] relevant to, for example,

tracking in the LHC Upgrade era. We have demonstrated this technique in the 800 MeV proton beam at the LANSCE facility of Los Alamos National Laboratory.

8.2 Introduction

Development of instrumentation often requires study of the interaction between high energy charged particles and materials. The energy transferred by charged beams through ionization and lattice displacement can lead to a loss of performance and accelerated aging of structural materials and electronic devices. Devices for the LHC or another future collider are typically tested for this sort of effect by being placed in a charged beam. We have developed a technique for real time measurement of the beam profile and fluence. This is an alternative to other methods such as thin metal foil activation [70], radiographic image analysis [71], flying wire [72], and Faraday cups [73], some of which are either not read concurrently with the beam operation, have larger uncertainties, or have lower sensitivity.

8.3 Description of the Diode Array

We construct an array of OSRAM BPW34F $p-i-n$ diodes [74] to characterize the charged particle beam. When $p-i-n$ diodes with bases manufactured from high resistivity n-type silicon are operated under the conditions of low injection, the concentration of carriers in the base region varies such that the resistivity ρ varies as a function of charged particle fluence Φ, as $\rho = \rho_0 e^{\Phi/K_\rho}$. Here ρ_0 is the initial equilibrium resistivity of silicon before irradiation and the coefficient K_ρ has a value between 400 and 3000 cm^{-2} for different silicon materials [75].

The forward voltage across the diode increases linearly with the fluence when

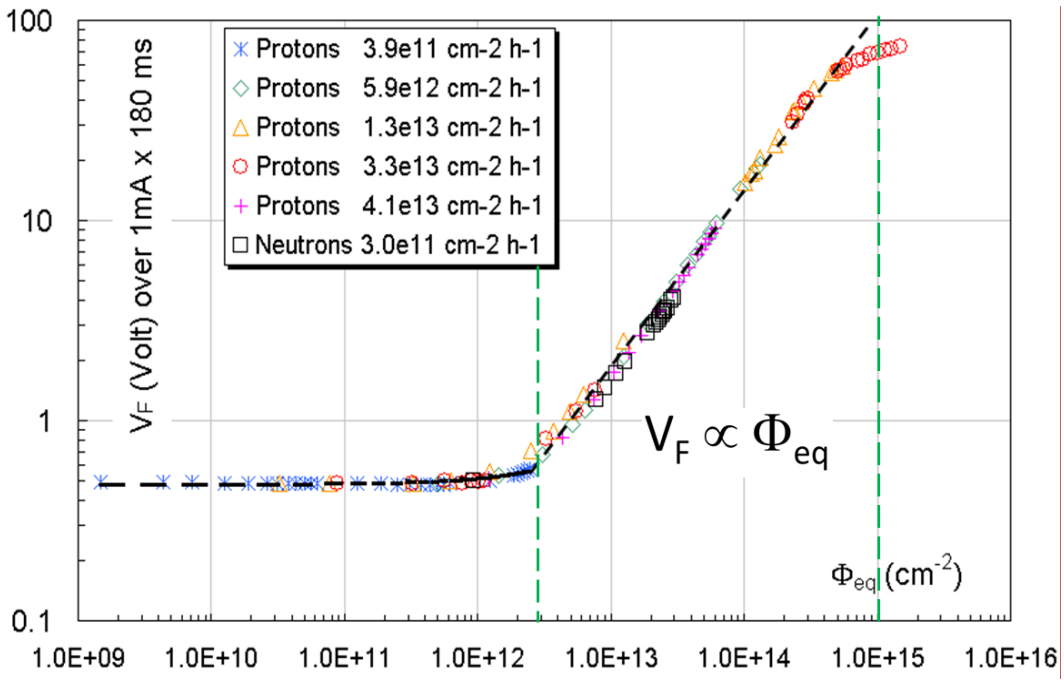

Figure 8.1: Forward voltage of a single OSRAM diode as a function of fluence in 1 MeV neutron equivalent cm^{-2} [76].

supplied with a constant forward current. The diode's forward voltage response at 1 mA, as a function of fluence, is shown in Figure 8.1 for exposure to 23 GeV protons and 0.8 MeV neutrons. On this graph, the response of the $p-i-n$ diodes to the proton damage is linear in the fluence range from 2×10^{12} to 10^{15} 1 MeV neutron equivalent (neq) per cm^2 before reaching saturation [76]. In the fluence region below 2×10^{12} neq per cm^2 (not studied here), high-sensitivity diodes from CMRP would provide a similar linear characteristic [77]. Advantages of using an array of $p-i-n$ diodes to measure the fluence include ease of readout, high spatial resolution, wide range of fluence response, independence of device orientation, dose-rate independence, and commercial availability at very low cost. A disadvantage of the diode is its temperature dependence. We minimize this disadvantage by sourcing the 1 mA current needed to operate them in short (130 ms) pulses.

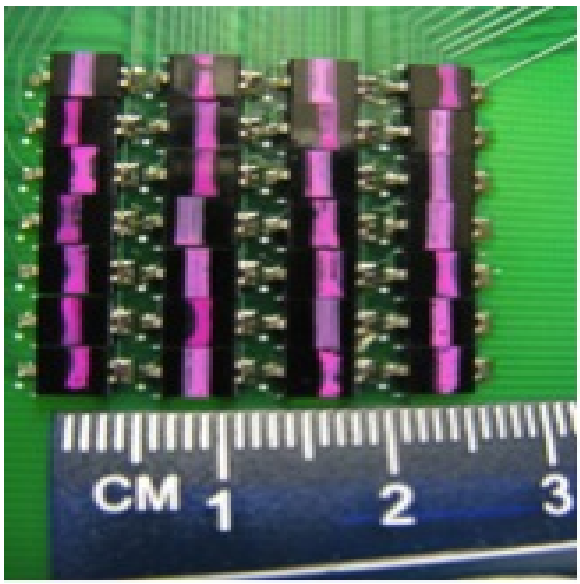

Figure 8.2: The front side of the diode array.

8.4 Diode Array Readout Hardware and Software

The diodes are soldered to back-to-back metalized pads on the two sides of a G10 board. Four columns of seven diodes each are on one side, and three columns of seven diodes each are interleaved between them on the other side, producing a 7x7 array with nearly complete coverage of a 2.5 cm^2 region when operated altogether (see Figure 8.2). The active area of each BPW34F diode is 2.65 mm x 2.65 mm, and the pitch between their centers is 3.8 mm. The board can be placed in a stack box (see Figure 8.3) with the devices under test (DUT). Custom automated diode scanner software using LabVIEW is capable of scanning 49 channels quickly and remotely without stoppage of the beam. To scan a specific channel, a source measure unit sources a pulse of current and reads out the forward voltage across the $p-n$ junction (see Figure 8.4). No special environment is required for these measurements.

Our diode array system uses a Keithley 2410 SourceMeter, a Keithley 706 Scanner, and a LabVIEW application. The LabVIEW code controls the setup and func-

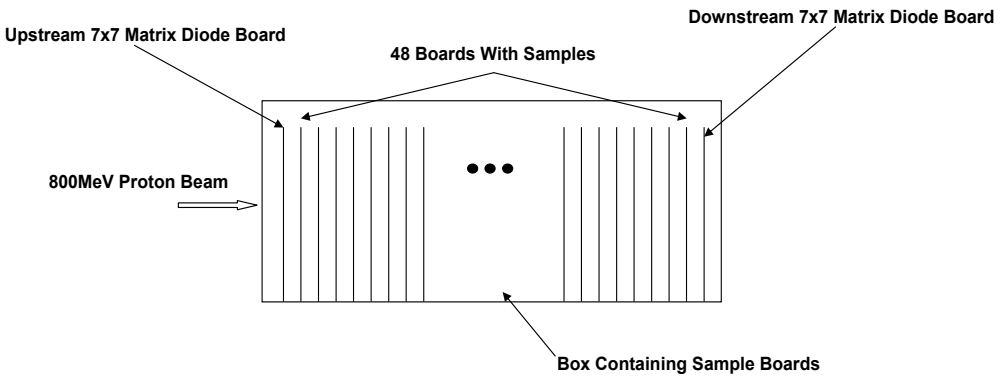

Figure 8.3: Setup layout of a stack box.

tioning of the SourceMeter and Scanner. In general the SourceMeter is set to source a 1 mA constant current while measuring the forward voltage of the selected diode. The Scanner selects each of the diodes as it is pulsed and reads them out one at a time. The total time per diode measurement is approximately 130 ms.

8.5 Calibration and Example Implementation

Two diode arrays were irradiated at the Los Alamos Neutron Science Center (LANSCE) in September 2012. The accelerator provides bunches of 5×10^{11} protons per macro-pulse at an energy of 800 MeV. The diameter of the proton beam spot is

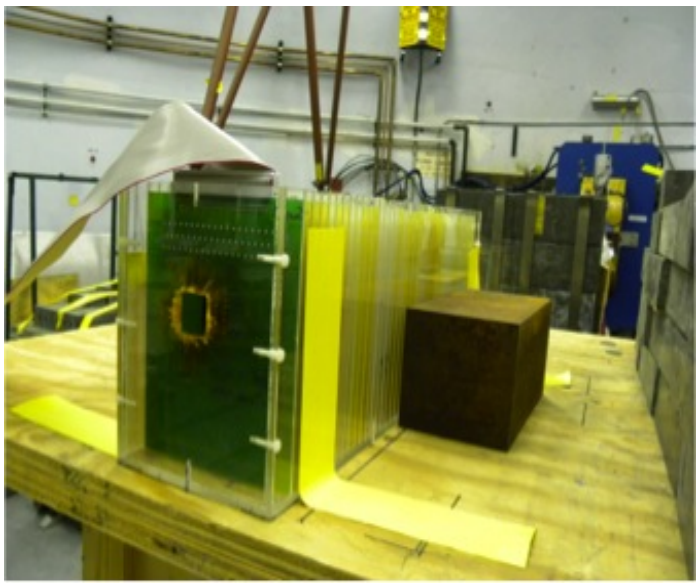

Figure 8.4: Stack box along the proton beam. The diode array is attached to cables in the first position.

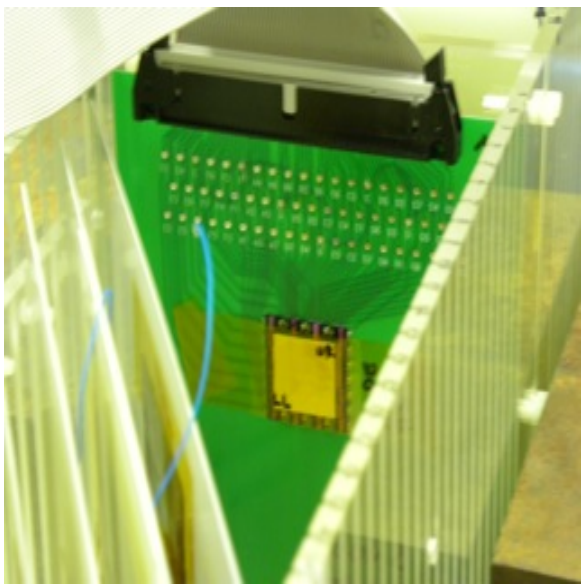

Figure 8.5: Aluminum foil matrix attached to the diode array.

about 2 cm. This proton beam is maintained at a constant current of 80 μA. A useful configuration is to place one array at each end of the stack to monitor beam depletion. Figure 8.5 shows the DUT stack box in the beam including one of the diode arrays. The electrical connections used for the beam profile measurement are shown in Figure 8.6. The arrays were read out over a 30 m cable after fluences of about 4 $\times 10^{13}$, 2 $\times 10^{14}$, 3.2 $\times 10^{14}$, and 8.2 $\times 10^{14}$ neq per cm^2.

We used aluminum foil activation to calibrate the diode response to fluence from the diode array for the LANSCE 800 MeV proton beam. A foil of size 2x2 cm^2 was attached directly to the diode array as shown in Figure 8.5. We then measured the activity of its central 1 cm^2 region and converted this to the proton fluence received by it. We also used four aluminum foils adjacent to the diode array in the stack box. At various points in the irradiation, the diode array was read out and one of the foils was removed at the same time. Figure 8.7 shows our measurements of fluence (from foil activation) and voltage (from the adjacent diodes). From the fitted line, we obtain a linearity coefficient $c = (6.786 \pm 1.090) \times 10^{-14}$ V/cm^{-2} for 800 MeV protons, which converts to $(9.558 \pm 1.536) \times 10^{-14}$ V/cm^{-2} for neq, using the hardness factor $k = 0.71$. This is consistent with the value of $(10.989 \pm 2.197) \times 10^{-14}$ V/cm^{-2} obtained in [78].

As a test of the effectiveness of this technique, the diode array measurements at the upstream and downstream ends of a stack of approximately forty 300 μm thick silicon sensors were compared four times over the period during which 3.7 x 10^{15} 800 MeV protons were delivered. The results of this study are shown in Figure 8.8, where one sees the beam profile spread as a result of scatters within the stack. The full width at half maximum (FWHM) measured by the upstream and downstream diode arrays is shown in Table 8.1 separately for the X and Y dimensions.

At any particular point in the stack, the resolution on the proton beam profile depends on the diode density. Because the grid is constituted by discrete points, the

Table 8.1: Full width at half maximum of the proton beam as measured by arrays before and after a stack of approximately 40 300μm silicon wafers, at four instances during a run.

Proton Pulses	Upstream array FWHM X (mm)	Upstream array FWHM Y (mm)	Downstream array FWHM X (mm)	Downstream array FWHM Y (mm)
144	15	15	17	17
488	12	11	15	15
3167	12	11	15	14
7556	13	12	15	15

resolution is given by $p/\sqrt{12}$, where p is the pitch [79]. In our case $p = 3.8$ mm so the resolution is 1.1 mm. The diodes in these prototypes were soldered by hand which limited the pitch achievable. Future iterations of this device could use integrated diodes with higher density and consequently better resolution.

8.6 Systematic Uncertainties

The current pulse width contributes uncertainty on the diode voltage of about 5%. This could be made arbitrarily smaller with use of a different Sourcemeter. The cable from the diode array to the readout scanner contributes an uncertainty of under 9%. This could be reduced by using a four wire measurement. The Keithley 2410 Sourcemeter measures the voltages to a precision of 0.015% + 50 mV. The uncertainty due to the temperature coefficient of the OSRAM BPW34F $p - i - n$ diodes is about 2.6%. The total uncertainty in the measurement of the fluence using forward voltage is determined to be 11% by summing in quadrature the individual uncertainties. This is comparable to the uncertainty achievable from a 60 minute post-experimental count of an activated aluminum foil.

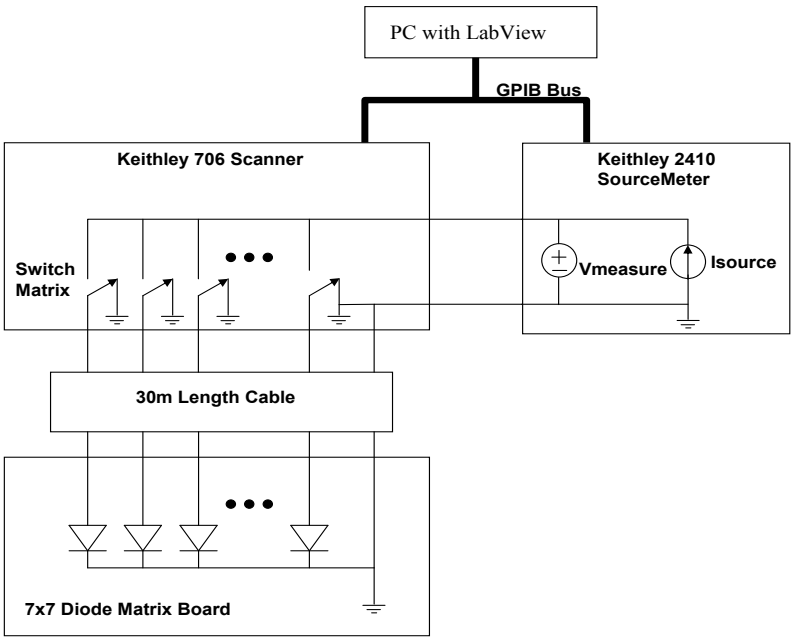

Figure 8.6: Electrical connections for the diode array readout.

8.7 Conclusions

A method for rapid in-situ measurement of beam profile and fluence using a diode array system is described. The fluence calibration of the diode array has been confirmed using aluminum foils. A few seconds' measurement of the fluence delivered during operation can be accomplished without stoppage of the beam to a precision (11%) comparable to that from a ∼60 minute post-experimental count of an activated aluminum foil. Using this technique we have verified the deterioration of the beam profile as the beam traverses a stack of approximately 40 300-μm silicon sensors. The resolution on real-time measurement of the beam profile is limited only by the pitch at which the experimenter assembles the diodes.

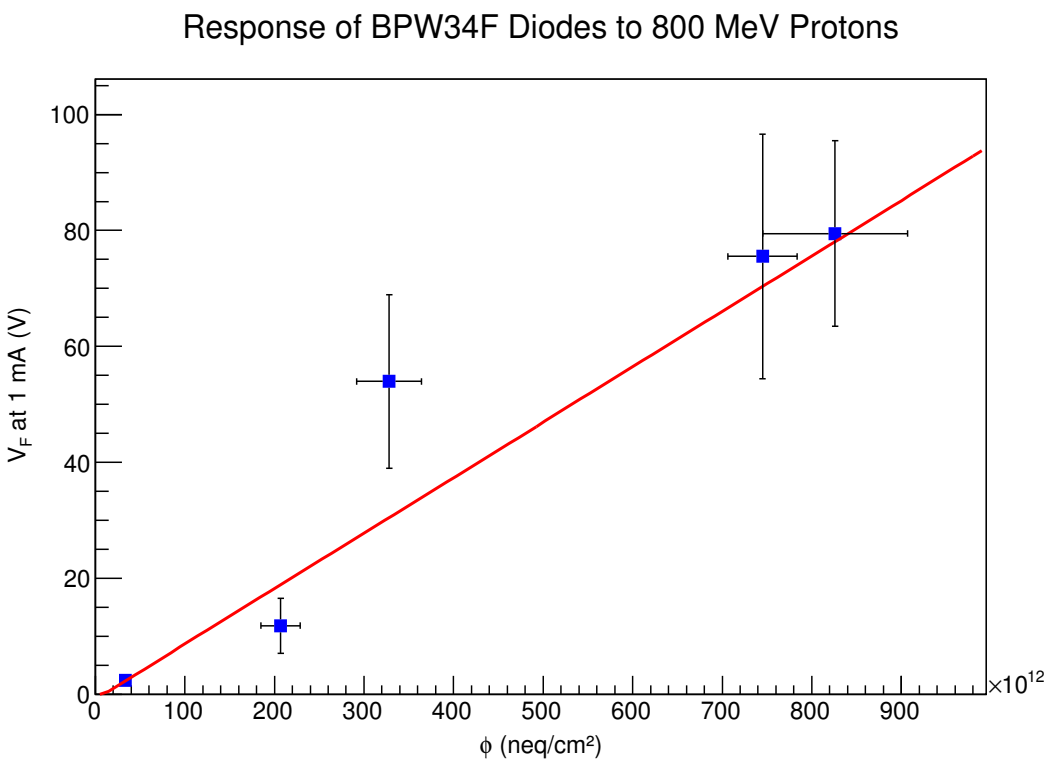

Figure 8.7: Calibration plot showing response of forward voltage of the diode array at 1 mA as a function of proton fluence.

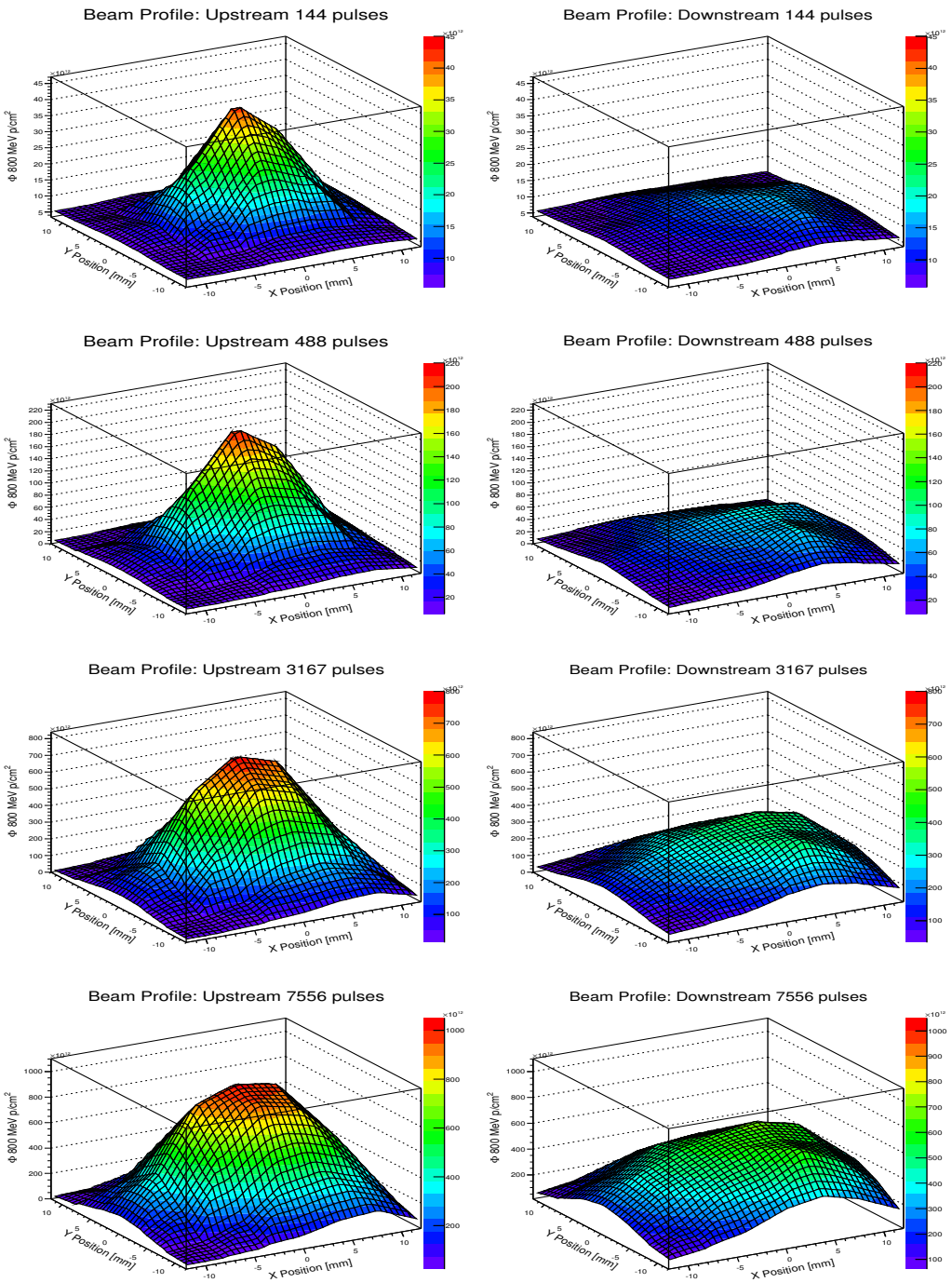

Figure 8.8: An example real time measurement of an evolving beam profile, made using a pair of diode arrays placed upstream (left column) and downstream (right column) of a stack of about 40 300-μm thick silicon sensors. In each subgraph, x and y indicate diode position. The vertical axis is fluence derived from voltage. The fluence received (in number of proton macro-pulses) increases downward. Note the vertical axes are different for each row. The graphs have been smoothed.

Chapter 9

Production of a Large Inclusive B/Charm Physics Monte Carlo Sample

9.1 Introduction

A setup, based on the CDF standard MC production framework, has been developed to produce a large inclusive B/charm physics Monte Carlo (BMC) sample. This sample is designed to be generic and is expected to serve future physics analyses which require a detailed understanding of the background composition. Comparing various Pythia generation modes, we choose the one which best represents the real data. We also present benchmark quantities, such as sample production time and disk usage that indicate how to optimize the scheme to utilise minimal CPU and disk resources to produce a one billion triggerable event sample.

9.2 Motivation and Goals

The CDF B physics group pursues a broad range of B and charm physics analyses and continues to produce world leading results using the full Run II dataset. Traditionally the B group analyses produced their own MC samples using custom setups which were not stored centrally nor documented adequately for their reuse by other analyses. Most of these samples were based on a specific signal or background decay, *e.g.* made with the `BGen` heavy hadron generator, and were outdated with each release of a newer CDF software framework.

At the end of Run II data taking, in late 2011, the CDF reconstruction software was finalized, an official `BStNtuple` format was created, and the `EvtGen` heavy hadron decayer was updated with the latest decay models and branching ratios. Anticipating a loss of manpower and computing resources in the future, the B group decided to produce a large generic B/charm Monte Carlo (BMC) sample to serve all the future analyses that will require background composition studies. Unlike a signal MC or a background MC with a fixed composition, a generic or inclusive MC is composed of all possible decay modes which can be fully or partially reconstructed by the CDF II analysis framework.

The CDF Monte Carlo production (MCprod) framework [80] includes four major steps,

1. $p\bar{p}$ hard scattering event generation,
2. CDF detector simulation,
3. Levels 1 and 2 trigger simulation, and
4. event reconstruction (also called *production*).

Although the cross section $\sigma(p\bar{p} \rightarrow b\bar{b})$ is large, $\mathcal{O}(100\ \mu\text{b})$, only a tiny fraction of potentially interesting B/charm events make it through our trigger requirements. Also, the step that consumes the most CPU time is the detector simulation, which beats the remainder by more than an order of magnitude. It is thus important to intelligently select events based on their generator level properties which have high chances of passing the trigger requirements, thereby conserving CPU resources in the detector simulation step. This additional (optional) step, called post-generation filtering, is introduced between steps 1 and 2 described above. The CDF B/charm analyses involve four trigger categories [1], namely:

1. BCHARM: Multi-body B/charm fully hadronic decays
2. DiMuon: Events involving a $J/\psi \rightarrow \mu\mu$ decay
3. Bhh: Two-body rare B hadronic decays
4. SemiLep: Semileptonic B/charm decays, comprising either an electron or a muon with a corresponding neutrino.

We introduce another (optional) step called trigger selection (in the `Prereq` module) between steps 3 and 4 of the MC production described above, to store only triggerable events in the MC sample. The paths involved in each trigger category are described in Section 9.5 in detail. The post-generation filtering is motivated by the four trigger categories and is a logical OR of five sets of requirements[2], which are described in Section 9.4 in detail as well.

To summarize, the main goals of this work is to choose a hard scattering event generation scheme which is the closest representative of the real data, then impose

[1] Each is based on a set of requirements, called paths, in Levels 1 and 2 of the CDF trigger system.

[2] The last two represent the electron and muon modes of the SemiLep trigger, respectively.

post-generation filtering to select potentially triggerable events for further detector and trigger simulation. This is followed by the trigger selection. Finally, an estimate is made of the disk space requirements for storing 1 billion triggered MCprod events and the corresponding BStNtuples.

9.3 Choice of Hard Scattering Event Generation

To produce a B/charm inclusive decay sample, a natural choice is the Pythia [81] generator which is widely used across all physics groups in CDF, and moreover it has been successfully used in other B analyses in the past[3].

Pythia is a highly configurable MC generator integrated into the CDF software framework. It lets the user choose between various combinations of QCD subprocesses by setting the `MSEL` parameter appropriately. The relevant options for our consideration are:

- MSEL = 4, 5: generate $c\bar{c}$, $b\bar{b}$ processes, respectively, using massive matrix elements. These are not useful for our purpose individually (we need both) and without modeling of the low-p_T production. However, we use the MSEL = 5 mode, as a B-only scenario for comparison with other realistic options.

- MSEL = 1: generates QCD high-p_T processes with low-p_T production activated. The latter is tuned to real data by CDF, called the *Rick Field Tune A* [82], to model the Underlying Event (UE) correctly. This is our default generation mode of choice.

- MSEL = 1, No UE: for comparison we also consider a case where the low-p_T production is switched off. In this case, the CDF recommendation is to require

[3]The other choice was the HERWIG generator which we didn't explore due to lack of understanding of its parameter tuning requirements for our low-p_T application

a minimum parton $\hat{p_T}$ of 5 GeV. This is motivated by 2 reasons: firstly, because the default MSEL=1 option consumes a significantly higher amount of CPU time for low-p_T production and leads to a larger event size; and secondly, B physics analyses are known not to depend strongly on UE modeling.

We want to compare the Pythia MSEL=5, MSEL=1 and MSEL=1,NoUE cases to choose the one which works the best for us in terms of data reproducibility, sample production time, and disk usage. For cross-checks we also compare a few more scenarios with slightly changed Pythia options, as described later.

9.4 Post-generation Filtering Requirements

The post-generation filtering requirements select events which are likely to pass at least one of the four trigger categories subsequently. This is a speed-up measure so we ensure that these requirements don't reject any triggerable event. Also, since the detector simulation has not run at this stage, all the requirements are applied based on generator level quantities only.

For an event to pass post-generation filtering, it is required to have a b or a c quark and to satisfy at least one of the five sets of filter cuts, *i.e.,*

(b || c) && (Filter-1 || Filter-2 || Filter-3 || Filter-4 || Filter-5),

where the filters are defined as:

- Filter-1: A decay which includes two muons
  - both have $p_T > 1.3$ GeV and $|\eta| < 1.3$

- Filter-2: A decay which includes two oppositely charged particles, p, K, π, e, or μ.
  - both have $p_T > 1.8$ GeV and $|\eta| < 1.3$
  - the pair have opposite charge, $p_{T1} + p_{T2} > 4.5$ GeV, and $\Delta\phi$ (opening azimuthal angle between two particles) < 140.
- Filter-3: A decay which includes two particles, p, K, π, e, or μ
  - both have $p_T > 1.8$ GeV and $|\eta| < 1.3$
  - the pair have $0 < \Delta\phi < 95$
- Filter-4: A semi-leptonic decay with an electron
  - electron with $E_T > 2.5$ GeV and $|\eta| < 1.3$
  - other particle: $|\eta| < 1.3$, $p_T > 1.8$ GeV, $\Delta\phi < 100$
- Filter-5: A semi-leptonic decay with a muon
  - muon with $p_T > 3.5$ GeV and $|\eta| < 0.8$
  - other particle: $|\eta| < 1.3$, $p_T > 1.8$ GeV, $\Delta\phi < 95$

9.5 Trigger Selection Requirements

The trigger selection step involves requiring a logical OR of the four trigger categories under consideration. Each of the categories is comprised of multiple trigger paths in Level-1 and/or Level-2 of the CDF trigger system, as described below:

- Bhh (L2): Selects 2-body hadronic B decays in Level-2
  - L2_B_PIPI

- BCHARM (L2): Selects multi-body hadronic B/charm decays in Level-2
  - L2_TWO_TRK2_D100_L1_OPPQ_DPHI135_SUMPT5.5
  - L2_B_CHARM
- DiMuon (L1): Selects Level-1 paths involving $J/\psi \to \mu\mu$ decays
  - L1_TWO_CMU1.5_PT1.5
  - L1_CMU1.5_PT1.5_&_CMX1.5_PT2
  - L1_CMUP6_PT4
- SemiLep (L2): Selects semi-leptonic (electron and muon) B decays in Level-2
  - L2_TRK2_D120_L1
  - L2_TRK2_D120_PS4_L1
  - L2_CMUP6_PT4_&_TRK2_D120_DPHI90
  - L2_CMUP6_PT4_SVT_&_TRK2_D120_DPHI90
  - L2_CMUP6_PT4_D0_&_TRK2_D120_DPHI90
  - L2_TRK2_D120_&_CEM4_PT4

9.6 Custom Monte Carlo Production Setup

Starting from the official (`6.1.4mc.m`, `patch-x`, `maxopt`) `MCprod` tarball [83] we make a custom tarball for inclusive BMC sample production, applying various changes as explained below. A detailed description of the `MCprod` framework and B-group specific usage can be found on the BMC webpage [84].

The following is an overview of the changes made to the official tarball:

- `mcProduction/scripts/run1segment` (modified):
  Made a simple fix to the crash recovery part of the master script which is run on CAF nodes for each segment.

- `mcProduction/scripts/MCProd` (modified):
  Introduced a new switch `MC_FILTER_PATH` to control whether a particular filter or an OR of all filters is required in the script run by run1segment for each section sequentially.

- `SimulationMods/test/setup_output.tcl` (modified):
  Made changes to handle the new filter conditions in the script that sets up the AC++ paths assigned to each output file (stream).

- `mcProduction/tcl/bmc_EvtGen_bcgeneric.tcl` (new):
  wrote this script that sets up B meson/baryon and prompt charm decays in `EvtGen`.

- `mcProduction/tcl/bmc_Pythia_msel1.tcl` (new): MSEL=1 default setup

- `mcProduction/tcl/bmc_Pythia_msel1NoUE.tcl` (new): MSEL=1 NoUE setup

- `mcProduction/tcl/bmc_postgen_MultiFilter.tcl` (new):
  wrote post-generation filter setup. Depending on `MC_FILTER_PATH`, it lets the user run a specific filter or an OR of all five.

- `mcProduction/tcl/bmc_prereq_allTrig.tcl` (new):
  Trigger selection setup for the `Prereq` module, performing an OR of all four trigger categories.

- `mcProduction/book/runlist_bmc_p0-p38.txt` (new):
  The complete RunII runlist.

- `mcProduction/book/cdfpbot/bbot01-3` (new):
  Dataset Definition Files (DDF) to run MSEL=1, MSEL=1 NoUE, and MSEL=5 setups. An example bbot01 DDF is listed in the Appendix.

Besides the above files we modify the following parameters in the DDFs for optimal use of the Central Analysis Farm (CAF) resources. A CAF job is divided into SEGMENTS and each segment runs on a worker node which can have multiple SECTIONS. The sections of a segment are run sequentially and their outputs are concatenated into one output file and shipped back to the user.

- NEV_PER_INV_NB: The run list provides the integrated luminosity of each run to be simulated. Based on the total number of requested events and this parameter, the number of events per segment is decided.
- NEV_PER_SECTION: An upper limit to the number of events that a job section can actually generate. It decides the number of sections in a job segment.
- RUN_LIST: This is the good run list used to generate the MC sample.
- SEGMENT_SIZE: Maximum size of a segment in MB. It decides how many segments a CAF job is divided into.
- N_SECTIONS: Total number of job sections determined by the segmentation script, `DSdef2SegmentList`.

All the modified files described above are provided as a tarball on the inclusive BMC webpage [85] with step-by-step instructions to produce samples. Here is a summary of the steps involved to produce an inclusive BMC sample:

- Download the latest B-group Monte Carlo tarball from the standard MC tarballs and web page [83], create a working directory, and unpack the tarball in it.

- Copy over or replace the files provided in the custom tarball.
- Create a new DDF or modify an existing one in the directory called `mcProduction/book/cdfpbot`, which may involve adding or editing tcl control files in `mcProduction/tcl`.
- Tune parameters such as NEV_PER_INV_NB, NEV_PER_SECTION and SEGMENT_SIZE in the DDF to achieve a desired sized data sample.
- The segmentation of the CAF job is handled by the `DSdef2SegmentList` script. Once the segments and sections therein are decided, the value of N_SECTIONS is updated in the DDF.
- When the DDF has been prepared, run a section locally to produce a 100 event test sample. If the test succeeds, delete the new files produced in the test job and re-tar the working directory.
- Finally, submit the full CAF job to the CDFGrid, NamGrid, or EuroGrid, specifying the icaf disk location in `submit_MCProd` script. We have noticed that EuroGrid and NamGrid are better choices over CDFGrid in terms of stability and reliability.

A set of pilot samples, both as MCprod output and as BStNtuple, have been produced and listed on the inclusive BMC webpage [85]. For simplicity they were produced using a limited runlist and include the first 3 trigger categories, both individually and combined.

9.7 Results and Discussion

In this section we present our findings on filter and trigger efficiencies, sample production times, and disk space usage for the scenarios under consideration.

Pythia Modes	b/c quark	filter-1	filter-2	filter-3	filter-4	filter-5	All OR'ed
MSEL=1	3.58	0.037	0.16	0.28	0.007	0.0015	0.31
MSEL=1 (noUE)	8.59	0.29	0.90	1.46	0.05	0.012	1.71
MSEL=5	100	12.84	17.58	27.57	2.40	0.85	35.73

Table 9.1: Individual and combined filter efficiencies (in %).

Triggers	MSEL=1 w.r.t. Ngen	MSEL=1 noUE w.r.t. Ngen	MSEL=5 w.r.t. Ngen	MSEL=1 w.r.t. Nsim	MSEL=1 noUE w.r.t. Nsim	MSEL=5 w.r.t. Nsim
All Triggers	0.21	0.82	99.24	68.17	48.18	277.75
Bhh	0.02	0.08	10.40	6.57	4.88	29.20
BCharm	0.17	0.63	70.87	53.42	36.98	198.98
Dimuon	0.04	0.16	26.45	13.52	9.38	74.27

Table 9.2: Individual and combined trigger efficiencies ($\times 10^{-4}$).

Table 9.1 lists individual filter efficiencies (in %) for the three Pythia modes. Table 9.2 lists the efficiencies for each trigger path individually and combined.

Table 9.3 lists the real and CPU times spent under the 3 Pythia modes for processing 250 million events. The CPU time split in seconds at different stages of simulation

Pythia Modes	Gen. Evts	Trig. Evts	Job time (hours)	Real Time Avg.(Max)	CPU time Avg.(Max)	Event size Avg.(Max)
MSEL=1	247M	5,351	27:00:18	8:17:28 (15:38:16)	7:49:56 (13:53:11)	127k (170k)
MSEL=1 (noUE)	260M	21,528	24:19:58	15:17:09 (24:08:22)	14:34:00 (23:35:19)	107k (112k)
MSEL=5	10M	100,754	17:24:16	6:24:10 (15:33:34)	6:16:06 (15:27:41)	128k (132k)

Table 9.3: Real and CPU time usage (in hours).

Pythia Modes	Ngen	Pythia (sec)	Evt Gen (sec)	Part-Filt. b/c	All 5 Filts	Det Sim (sec)	Nsim	XFT (sec)	Ntrig
MSEL=1	2.5M	13275	777	47	272	10795	7845	122	88
MSEL=1 (noUE)	2.5M	3635	1277	72	1028	53766	43362	333	294
MSEL=1 (noUE) + nopT	2.5M	2689	909	52	307	5352	4757	70	51
MSEL=5	35K	322	52	0.1	250	20315	12528	247	215

Table 9.4: CPU time split (in sec) at various stages of MC production.

is shown in Table 9.4. It also verifies that the bulk of time is spent in detector simulation and reconstruction. In addition to the three usual Pythia modes, this table also lists MSEL=1, NoUE with no $\hat{p_T}$ cut (the $\hat{p_T}$ cut is set to 5 GeV by default for other studies).

As shown, the majority of processing time is spent on detector simulation, except in the case of the for MSEL=1 (with UE) mode, where a comparable amount of time is spent in low-p_T production by Pythia. Table 9.5 shows the processing time and disk space required to produce BStNtuples from MCprod data. Table 9.6 shows the processing time and disk space estimate to produce an inclusive BMC sample of one billion triggered events.

The estimated CPU hours, number of CAF long queue jobs, and disk space required to store the MCprod and BStNtuple files are all reasonable and have been accepted by the CDF B group to proceed with production.

Pythia Modes	Nprod	Total Time (in hours)	BstNtuple File Size (in MB)
MSEL=1 (Bhh)	5,351	0:16	25
MSEL=1 (Bcharm)	5,351	2:06	195
MSEL=1 (Dimuon)	5,351	0:06	13
MSEL=1 (AllTrig)	5,351	2:08	209
MSEL=1 (noUE, Bhh)	21,528	0:33	65
MSEL=1 (noUE, Bcharm)	21,528	4:35	505
MSEL=1 (noUE, Dimuon)	21,528	0:40	103
MSEL=1 (noUE, AllTrig)	21,528	5:30	625
MSEL=5 (Bhh)	100,754	4:00	384
MSEL=5 (Bcharm)	100,754	31:50	2962
MSEL=5 (Dimuon)	100,754	6:29	862
MSEL=5 (AllTrig)	100,754	35:30	3536

Table 9.5: Processing time and disk space usage for BStNtupling.

9.8 Validation of Pilot Samples and Improvement

Validation of the prepared pilot samples has to be done to better understand the functionality of our setup. Several studies and tests were performed, and are discussed below.

We added the semileptonic trigger category to our trigger selection, as explained in Section 9.5. The corresponding electron and muon Level-2 paths were taken from

Pythia Modes Modes	Max. Real time (in hours)	Long CAF time (in hours)	Production files size (in TB)	Ntupling time time (in hours)	BStNtuple size (in TB)
MSEL=1	2922,402	40,589	131	398,679	37.2
MSEL=1 (noUE)	1121,304	15,574	103	255,481	27.6
MSEL=5	154,430	2,145	110	352,343	33.5

Table 9.6: Processing time and disk space usage for one billion triggered inclusive BMC events.

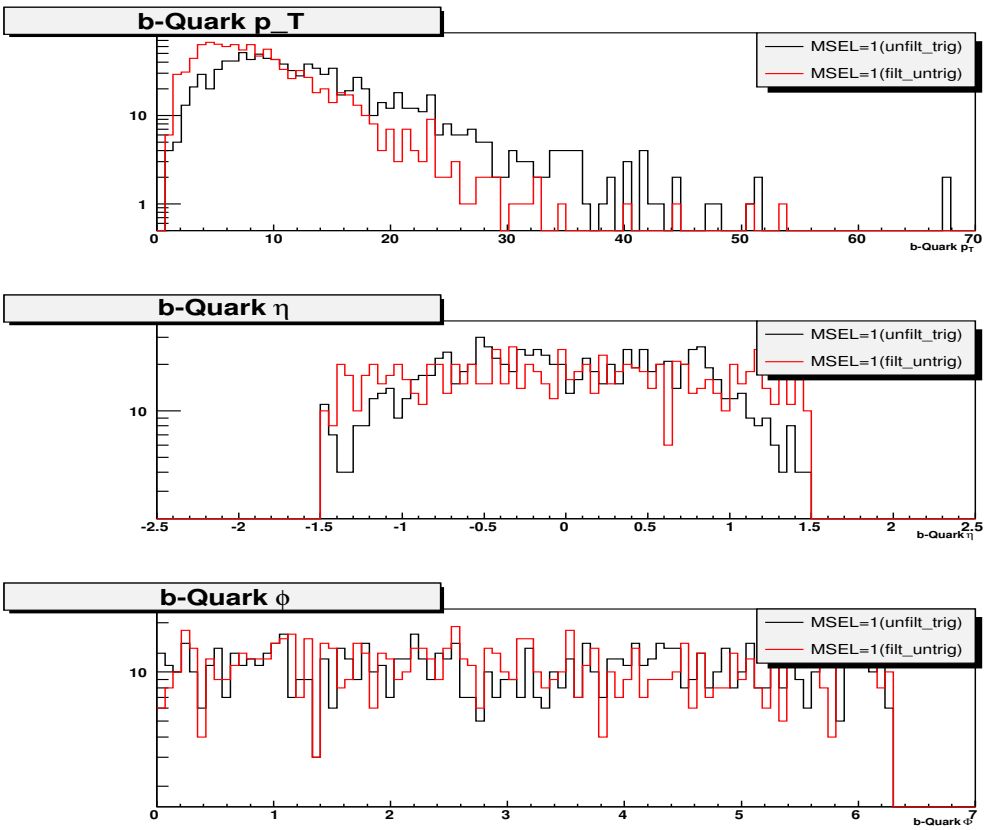

Figure 9.1: The b quark p_T, η, and ϕ distributions for the MSEL=1 case. In each plot the no-filter with trigger (black) and filter with no trigger (red) distributions are compared.

Table 4 of the BStNtuple User Guide [86]. The pilot samples mentioned in the earlier sections don't include this trigger category.

As shown in Table 9.4, the CPU time spent in Pythia is more than 3.5 times larger for MSEL=1 with than without the UE. We use a cutoff of $\hat{p_T} > 5$ GeV in the latter (noUE) case, following CDF recommendation. To understand if this difference is mainly due to the cutoff or to the (Rick Field Tune A) UE generation machinery, cases with and without the cutoff were compared. Comparing the third and fourth rows of Table 9.4, one sees that the difference is not affected appreciably by changing

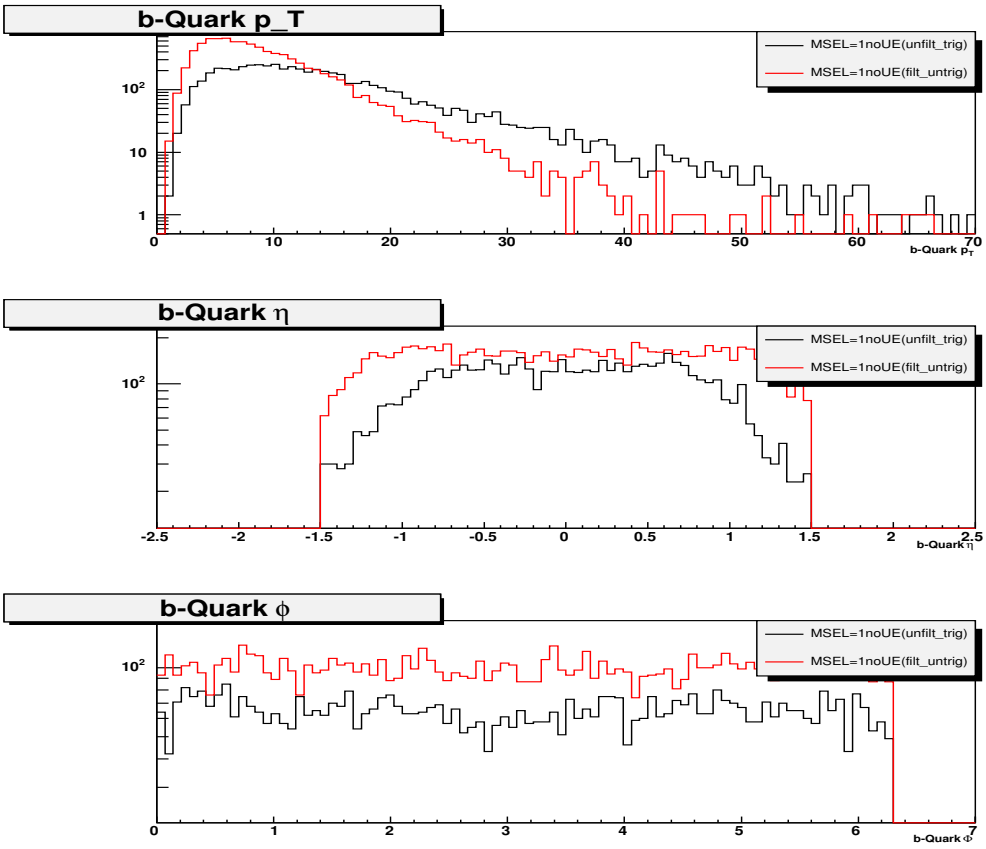

Figure 9.2: The b quark p_T, η, and ϕ distributions for the MSEL=1 noUE case. In each plot the no-filter with trigger (black) and filter with no trigger (red) distributions are compared.

the cutoff. Figure 9.1 and Figure 9.2 show b quark p_T, η, and ϕ distributions for MSEL=1 with and without the UE cases, respectively. In each plot the no-filter with trigger (black) and filter without trigger (red) distributions are compared with arbitrary normalization. A comparison of shapes suggest that the filters provide close to optimal performance.

9.9 Sample Production

Following the B group's approval, Pythia MSEL=1 with UE was chosen as the physics process for simulation. The official area for production job submission is: fcdflnxN:/cdf/spool/behari/inclusive BMC/. The README file in it explains the steps in detail to produce samples using grid resources. The output is managed at fcdfdas11:/cdf/local/disk01/saty/InclBMC Data. One million triggerable events are produced per week which corresponds to 3 pb^{-1} of integrated luminosity. The target is to produce a few hundred million event's sample by January 2014. A webpage [87] provides automated monitoring of MC production, concatenation, and tape upload steps.

9.10 Summary

We have created a customized MCprod setup to produce a large inclusive B/charm Monte Carlo sample. Pilot samples have been successfully produced using this setup. The filter and trigger efficiencies, CPU time, and disk space usage suggest that with the available resources, production of a one billion triggered event sample is feasible. The produced MCprod and BStNtuple pilot samples are available for validation. A dedicated webpage provides links to them and step by step instructions to produce new inclusive BMC samples.

Chapter 10

Summary, Conclusions, and Outlook

A search for the $\Lambda_b^{*0} \to \Lambda_b^0 \pi^- \pi^+$ resonance state in its [9, 88] Q-value spectrum was carried out successfully. A narrow structure is identified at mass 5919.22 $\pm$ 0.76 MeV/c^2 with a significance of 3.5σ. This signal is attributed to the orbital excitation of the bottom baryon Λ_b^0 and supports similar findings in proton-proton collisions at LHC. The limitations of the CDF detector and the end of the Tevatron run in Fall 2011 restricted analysis of the Λ_b^{*0} in greater detail. One has to analyze the data collected at the LHC to measure the masses and widths of excited states such as the Λ_b^{*0} with better precision. The LHCb detector, which has a high precision tracking system consisting of a silicon-strip vertex detector surrounding the pp interaction region, is the most suitable for these measurements. I look forward to extending this analysis work by searching for new heavy excited b or c baryons and mesons, which are useful for probing QCD in its confinement domain. The precise measurement of their masses and widths will test the HQET models used to describe the interaction of heavy quarks. Further extending this work to include the study of differential cross sections of vector bosons (W, Z, γ) and associated heavy flavor

jets (b or c) in the final state would allow us to reduce a large background [89, 90] in top quark physics and Higgs related analyses. These measurements may also improve the precision of heavy quark pdfs. I believe we need to address the large top quark Yukawa coupling problem by rigorously studying these processes. The study of associated production of different heavy flavor quarks can provide a probe for the existence of additional charged massive bosons, which will allow us to study new physics beyond the Standard Model.

A method for rapid real time measurement of beam profile and fluence using a diode array system is demonstrated using an 800 MeV proton beam at the LANSCE facility of Los Alamos National Laboratory. The study of radiation damage to the components of new particle tracking detectors is crucial for the continued development of the collider physics experiments. The resolution on this real-time measurement of the beam profile is limited by the pitch at which the experimenter assembles the diodes. We can extend this work by integrating the $p-i-n$ diodes on the silicon substrate to increase the pitch and improve the resolution on the real-time measurement. Furthermore, it may be possible to perform a 3D measurement by using a matrix of diode layers and testing them with the 800 MeV proton beam. These measurements would explain degradation of detector materials as a beam penetrates deep into the materials.

Appendix A

Inclusive BMC Study

A.1 Dataset Definition File (bbot01) Example

```
#-------------------------------------------------------------
DSID                    bbot01
BOOK                    cdfpbot
DSNAME       PythiaMSEL1_BCgeneric_PGall_614mcm_testxftsvtrunlist
GENERATION_MODE         0
MC_PROCESS_TCL          bmc_Pythia_msel1.tcl
FILTER_TCL              bmc_postgen_MultiFilterNew.tcl
FILTER_PATH             -1
MINBIAS_TCL
MC_TRIGSIM_TCL          bmc_trigsim_newxftsvt.tcl
GEN_PARTICLE            6
MC_DECAY_TCL            bmc_EvtGen_bcgeneric.tcl
#USER_DECAY_FILE
BMC_SAMPLE_NUM          251
```

```
PREREQ_TRIG_TCL         bmc_prereq_allTrig.tcl
NEV_PER_INV_NB          30.0
NEV_PER_SECTION         15000
FIRST_RUN               151434
LAST_RUN                261518
RUN_LIST                runlist_bmc_testxftsvt.txt
N_SECTIONS              71
FILTER_EFF              100
EVENT_SIZE              300
SEGMENT_SIZE            2000
#-------------------------------------------------------------
```

References

[1] S. Chatrchyan *et al.* (CMS Collaboration). Observation of a new boson at a mass of 125 gev with the cms experiment at the lhc. *Phys. Lett. B*, 716(30), 2012.

[2] G. Aad *et al.* (ATLAS Collaboration). Observation of a new particle in the search for the standard model higgs boson with the atlas detector at the lhc. *Phys. Lett. B*, 716(1), 2012.

[3] A. V. Manohar. Heavy quark effective theory and nonrelativistic QCD Lagrangian to order α_s/m^3. *Phys. Rev. D*, 56(1), 1997.

[4] M. Neubert. Heavy-quark symmetry. *Phys. Rep.*, 245(259), 1994.

[5] N. Isgur. Weak transition form factors between heavy mesons. *Phys. Lett. B*, 237(527), 1990.

[6] R. R. Wilson. The Tevatron. FERMILAB-TM-0763, 1978.

[7] T. Aaltonen *et al.* (CDF Collaboration). Operational experience, improvements, and performance of the CDF Run II silicon vertex detector. *Nucl. Instrum. Methods Phys. Res., Sect. A*, 729(153), 2013.

[8] CERN Collaboration. The Large Hadron Collider. http://home.web.cern.ch/topics/large-hadron-collider.

[9] T. Aaltonen *et al.* (CDF Collaboration). Evidence for a bottom baryon resonance Λ_b^{*0} in CDF data. *Phys. Rev. D*, 88(071101), 2013.

[10] P. Palni *et al.* (CDF Collaboration). Heavy flavor production and spectroscopy with CDF. *Nucl. Phys. Proc. Suppl.*, 233:151–156, 2012.

[11] Igor V. Gorelov *et al.* (CDF Collaboration). Evidence for the bottom baryon resonance state Λ_b^{*0} with the CDF II detector. *Proc. of Scie. (ICHEP2012)*, 349, 2012.

[12] Robert Oerter. *The Theory of Almost Everything: The Standard Model, the Unsung Triumph of Modern Physics*. Plume, 2006.

[13] M. E. Peskin and D. V. Schroeder. *An Introduction To Quantum Field Theory*. Westview, 1995.

[14] F. Abe *et al.* (CDF Collaboration). Observation of Top Quark Production in $p\bar{p}$ Collisions with the Collider Detector at Fermilab. *Phys. Rev. Lett.*, 74:2626–2631, 1995.

[15] M. Kobayashi and T. Maskawa. Cp-violation in the renormalizable theory of weak interaction. *Prog. Theor. Phys.*, 49(2), 1973.

[16] N. Cabibbo. Unitary symmetry and leptonic decays. *Phys. Rev. Lett.*, 10(531), 1963.

[17] S. Nussinov and W. Wetzel. Comparison of exclusive decay rates for b $\rightarrow$ u and b $\rightarrow$ c transitions. *Phys. Rev. D*, 36(130), 1987.

[18] N. Isgur and M. B. Wise. Weak decays of heavy mesons in the static quark approximation. *Phys. Lett. B*, 232(113), 1989.

[19] N. Isgur and M. B. Wise. Relationship between form-factors in semileptonic anti-b and d decays and exclusive rare anti-b meson decays. *Phys. Rev. D*, 42(2388), 1990.

[20] N. Isgur and M. B. Wise. Spectroscopy with heavy quark symmetry. *Phys. Rev. Lett.*, 66(1130), 1991.

[21] N. Isgur and M. B. Wise. Weak transition form-factors between heavy mesons. *Phys. Lett. B*, 237(527), 1990.

[22] J. Beringer *et al.* (Particle Data Group Collaboration). Review of particle physics. *Phys. Rev. D*, 86(010001), 2012.

[23] V.M. Abazov *et al.* (D0 Collaboration). The upgraded D0 detector. *Nucl. Instrum. Methods A*, 565(463), 2006.

[24] CDF Collaboration. Technical Design Report. FERMILAB-PUB-96-390-E, 1996.

[25] A. Affolder *et al.* (CDF Collaboration). Intermediate Silicon Layers Detector for the CDF Experiment. *Nucl. Instrum. Methods A*, 453:84–88, 2000.

[26] K. Nakamura *et al.* (Particle Data Group Collaboration). Review of particle physics. *J. Phys. G*, 37(075021), 2010.

[27] E. Klempt and J. M. Richard. Baryon spectroscopy. *arXiv:0901.2055 [hep-ph]*, 2009.

[28] J. L. Rosner. Hadron spectroscopy: Theory and experiment. *J. Phys. G*, 34:S127, 2007.

[29] S. Capstick and W. Roberts. Quark models of baryon masses and decays. *Prog. Part. Nucl. Phys.*, 45(S241), 2000.

[30] S. Capstick and N. Isgur. Baryons in a relativized quark model with chromodynamics. *Phys. Rev. D*, 34(2809), 1986.

[31] S. Gasiorowicz and J. L. Rosner. Hadron spectra and quarks. *Am. J. Phys.*, 49(954), 1981.

[32] M. Karliner, B. Keren-Zur, H. J. Lipkin, and J. L. Rosner. Predictions for masses of bottom baryons. *arXiv:0708.4027 [hep-ph]*, 2007.

[33] M. Karliner. Heavy quark spectroscopy and prediction of bottom baryon masses. *Nucl. Phys. Proc. Suppl.*, 187(21), 2009.

[34] M. Karliner, B. Keren-Zur, H. J. Lipkin, and J. L. Rosner. The quark model and b baryons. *Ann. Phys.*, 324(2), 2009.

[35] W. Roberts and M. Pervin. Heavy baryons in a quark model. *Int. J. Mod. Phys.*, 23(2817), 2008.

[36] H. Garcilazo, J. Vijande, and A. Valcarce. Faddeev study of heavy baryon spectroscopy. *J. Phys. G*, 34(961), 2007.

[37] D. Ebert, R. N. Faustov, and V. O. Galkin. Masses of heavy baryons in the relativistic quark model. *Phys. Rev. D*, 72(034026), 2005.

[38] D. Ebert, R. N. Faustov, and V. O. Galkin. Masses of excited heavy baryons in the relativistic quark model. *Phys. Lett. B*, 659(612), 2008.

[39] D. Ebert, R. N. Faustov, and V. O. Galkin. Mass spectra of heavy baryons in the relativistic quark model. *Phys. Atom. Nucl.*, 72(178), 2009.

[40] J. R. Zhang and M. Q. Huang. Heavy baryon spectroscopy in qcd. *Phys. Rev. D*, 78(094015), 2008.

[41] J. R. Zhang and M. Q. Huang. Heavy flavor baryon spectra via qcd sum rules. *arXiv:0904.3391 [hep-ph]*, 2009.

[42] E. E. Jenkins. Model-independent bottom baryon mass predictions in the 1/n(c) expansion. *Phys. Rev. D*, 77(034012), 2008.

[43] Z. Aziza Baccouche, C. K. Chow, T. D. Cohen, and B. A. Gelman. Excited heavy baryons and their symmetries. III: Phenomenology. *Nucl. Phys. A*, 696(638), 2001.

[44] R. Aaij *et al.* (LHCb Collaboration). Observation of excited Λ_b^0 baryons. *Phys. Rev. Lett.*, 109(172003), 2012.

[45] A. Belloni, I. K. Furic, and Ch. Paus (CDF Collaboration). Multibody trigger paths in the two track trigger data. Cdf/phys/bottom/public/6526.

[46] A. Abulencia *et al.* (CDF Collaboration). Observation of $B_s^0 - \bar{B}_s^0$ Oscillations. *Phys. Rev. Lett.*, 97(242003), 2006.

[47] P. Nason, S. Dawson, and R. K. Ellis. The total cross-section for the production of heavy quarks in hadronic collisions. *Nucl. Phys. B*, 303(607), 1988.

[48] C. Peterson, D. Schlatter, I. Schmitt, and P. M. Zerwas. Scaling violations in inclusive e+ e- annihilation spectra. *Phys. Rev. D*, 27(105), 1983.

[49] D. J. Lange. The evtgen particle decay simulation package. *Nucl. Instrum. Methods Phys. Res., Sect. A*, 462(152), 2001.

[50] R. Brun, R. Hagelberg, M. Hansroul, and J.C. Lassalle. CERN Reports No. CERN-DD-78-2-REV.

[51] C. Calancha, J.P. Fernandez, I. Gorelov, L. Labarga, and S. Seidel. Measurement of the Bottom Baryon Resonances $\mathbf{\Sigma_b}$ and $\mathbf{\Sigma_b^*}$. CDF Internal Note CDF/PHYS/BOTTOM/CDFR/10194.

[52] I. Gorelov, D. Litvintsev, P. Maksimovic, M. Martin, J. Pursley, M. Schmidt, S. Seidel, R. J. Tesarek, and E. Vataga. Λ_b^0 Data Sample and Mass Fit with Two Displaced Track Trigger Using $1\,\mathrm{fb}^{-1}$. CDF Internal Note CDF/PHYS/BOTTOM/CDFR/8395.

[53] I. Gorelov, D. Litvintsev, P. Maksimovic, M. Martin, J. Pursley, M. Schmidt, S. Seidel, R. J. Tesarek, and E. Vataga. Search for New Heavy Baryons Σ_b and Σ_b^* in the Two Track Trigger Data Using $1\,\mathrm{fb}^{-1}$. CDF Internal Note CDF/PHYS/BOTTOM/CDFR/8396.

[54] T. Aaltonen *et al.* (CDF Collaboration). First observation of heavy baryons Σ_b and Σ_b^*. *Phys. Rev. Lett.*, 99(202001), 2007.

[55] A. Abulencia *et al.* (CDF Collaboration). Measurement of $\sigma(\Lambda_b^0)/\sigma(\bar{B}^0) \times BR(\Lambda_b^0 \to \Lambda_c^+\pi^-)/BR(\bar{B}^0) \to D^+\pi^-)$ in $p\bar{p}$ collisions at $\sqrt{s} = 1.96$ TeV. *Phys. Rev. Lett.*, 98(122002), 2007.

[56] T. Aaltonen *et al.* (CDF Collaboration). Measurement of the branching fraction $\mathcal{B}(\Lambda_b^0 \to \Lambda_c^+\pi^-\pi^+\pi^-)$ at CDF. *Phys. Rev. D*, 85(032003), 2012.

[57] T. Aaltonen *et al.* (CDF Collaboration). Measurement of the masses and widths of the bottom baryons Σ_b^{+-} and Σ_b^{*+-}. *Phys. Rev. D*, 85(092011), 2012.

[58] G. Punzi. Sensitivity of searches for new signals and its optimization. *arXiv:308063 [physics.data-an]*, 2003.

[59] Shin-Shan Yu, Rick Tesarek, Dmitri Litvintsev, Joel Heinrich, and Nigel Lockyer. Ratio of $\mathcal{B}(\Lambda_b^0 \to \Lambda_c^+\mu^-\overline{\nu}_\mu)$ to $\mathcal{B}(\Lambda_b^0 \to \Lambda_c^+\pi^-)$ in the Two Track Trigger. CDF Internal Note CDF/PHYS/BOTTOM/CDFR/7559.

[60] Y. Le, M. Martin, and P. Maksimovic. Observation of $\Lambda_b^0 \to \Lambda_c^+\pi_b^-$ and the Measurement of $f_{\Lambda_b^0} \cdot \mathcal{B}(\Lambda_b^0 \to \Lambda_c^+\pi_b^-)/f_{B^0} \cdot \mathcal{B}(B^0 \to D^-\pi^+)$. CDF Internal Note CDF/ANAL/BOTTOM/CDFR/6396, 1983.

[61] S.S. Wilks. The large-sample distribution of the likelihood ratio for testing composite hypotheses. *Ann. Math. Statist.*, 9(60):2, 1938.

[62] R. Royall. On the probability of observing misleading statistical evidence. *J. Amer. Statist. Assoc.*, 95(760), 2000.

[63] T. Aaltonen *et al.* (CDF Collaboration). Measurements of the properties of $\Lambda_c(2595)$, $\Lambda_c(2625)$, $\Sigma_c(2455)$, and $\Sigma_c(2520)$ baryons. *Phys. Rev. D*, 84(012003), 2011.

[64] D. Acosta *et al.* (CDF Collaboration). Measurement of b hadron masses in exclusive J/ψ decays with the CDF detector. *Phys. Rev. Lett.*, 96(202001), 2006.

[65] R. Aaij *et al.* (LHCb Collaboration). Measurement of the Λ_b^0, Ξ_b^-, and Ω_b^- Baryon Masses. *Phys. Rev. Lett.*, 110(182001), 2013.

[66] K.F. Schoenberg and P.W. Lisowski. LANSCE a key facility for national science and defense. Los Alamos Science No. 30, 2006.

[67] T.N. Taddeucci, J. Ullmann, L.J. Rybarcyk, G.W. Butler, and T.E. Ward. Total cross sections for production of ^{7}Be, ^{22}Na, and ^{24}Na in p + ^{7}Li and p + ^{27}Al reactions at 495 and 795 MeV. *Phys. Rev. C*, 55:1551–1554, 1997.

[68] G.L. Morgan *et al.* Total cross sections for the production of ^{22}Na and ^{24}Na in proton-induced reactions on ^{27}Al from 0.40 to 22.4 GeV. *Nucl. Instrum. Methods Phys. Res., Sect. B*, 211:297–304, 2003.

[69] P. Palni *et al.* A method for real time monitoring of charged particle beam profile and fluence. *Nucl. Instrum. Methods Phys. Res., Sect. A*, 735:213–217, 2013.

[70] C. Furetta *et al.* Fluence and Dosimetric Measurements For a $\pi^{\pm}$ Irradiation Facility. CERN Reports No. CERN-ECP/95-2, 1995.

[71] M. Glaser *et al.* Dosimetry Assessments in the Irradiation Facilities at the CERN-PS Accelerator. *IEEE Trans. Nucl. Sci.*, 53(4):2016–2022, 2006.

[72] W. Blokland *et al.* A new flying wire system for the tevatron. In *Proc. Particle Accelerator Conference*, volume 2, Vancouver, Canada, 1997.

[73] D. Bisello *et al.* Radiation Damage of Standard and Oxygenated Silicon Diodes Irradiated by 16-MeV and 27-MeV Protons. *IEEE Trans. Nucl. Sci.*, 48(4):1020–1027, 2001.

[74] OSRAM Opto-Semiconductors. BPW34F photodiode datasheet. http://www.osram-os.com.

[75] M. G. Buehler *et al.* On-chip p-mosfet dosimetry. *IEEE Trans. Nucl. Sci.*, 40(6):1442 – 1449, 1993.

[76] F. Ravotti. *Development and Characterization of Radiation Monitoring Sensors for the High Energy Physics Experiments of the CERN LHC Accelerator.* Doctoral dissertation, Université Montpellier II, 2006.

[77] A. B. Rosenfeld *et al.* Neutron dosimetry with planar silicon p-i-n diodes. *IEEE Trans. Nucl. Sci.*, 50(6):2367 – 2372, 2003.

[78] F. Ravotti *et al.* Radiation Monitoring in Mixed Environments at CERN: From the IRRAD6 Facility to the LHC Experiments. CERN Reports No. CERN-PH-EP/2006-024, 2006.

[79] G. Lutz. *Semiconductor Radiation Detectors*. Springer, 1999.

[80] CDF Collaboration. CDF Monte Carlo Production. http://www-cdf.fnal.gov/internal/mcProduction/index.html.

[81] Torbjorn Sjostrand, Leif Lonnblad, and Stephen Mrenna. Pythia 6.2 Physics and Manual. arXiv:0108264 [hep-ex].

[82] R. Field and R. C. Group. Pythia Tune A, Herwig, and Jimmy in Run 2 at CDF. *arXiv:0510198 [hep-ph]*, 2005.

[83] CDF Collaboration. The standard MCprod tarballs. http://www-cdf.fnal.gov/internal/mcProduction/pages/tarballs.html.

[84] CDF Collaboration. B Group Monte Carlo Webpage. http://www-cdf.fnal.gov/internal/physics/bottom/bmontecarlo/.

[85] CDF Collaboration. Inclusive BMC Production Webpage. http://www-cdf.fnal.gov/internal/physics/bottom/b-montecarlo/inclusive_mc.html.

[86] CDF Collaboration. BStNtuple User Guide. http://www-cdf.fnal.gov/htbin/notes/cdfnoteSelGet?number=10711.

[87] CDF Collaboration. Production dashboard. http://www-cdf.fnal.gov/internal/physics/bottom/b-montecarlo/InclBMC progress.html.

[88] Prabhakar Palni *et al.* (CDF Collaboration). Evidence for a bottom baryon resonance Λ_b^{*0} in CDF data. *arXiv:1309.6269 [hep-ex]*, 2013.

[89] G. Aad *et al.* (ATLAS Collaboration). Study of jets produced in association with a W boson in pp collisions at $\sqrt{s} = 7$ TeV with the ATLAS detector. *Phys. Rev. D*, 85(092002), 2012.

[90] V. M. Abazov *et al.* (D0 Collaboration). Measurements of Differential Cross Sections of Z/γ^*+jets+X Events in $p\bar{p}$ Collisions at $\sqrt{s} = 1.96$ TeV . *Phys. Lett. B*, 678(45), 2009.